8-1-1991

Computing Torque and Related Output Variables of a Switched ReluctanceMachine Using a Magnetic Circuit Approach

Matthew E. Toennies
Purdue University

Computing Torque and Related Output Variables of a Switched Reluctance Machine Using a Magnetic Circuit Approach

Matthew E. Toennies

TR-EE-91-30
August 1991

COMPUTING TORQUE AND RELATED OUTPUT VARIABLES OF A SWITCHED RELUCTANCE MACHINE USING A MAGNETIC CIRCUIT APPROACH

A Thesis

Submitted to the Faculty

of

Purdue University

by

Matthew Eric Toennies

In Partial Fulfillment of the

Requirements for the Degree

of

Master of Science in Electrical Engineering

August 1991

This Thesis is dedicated to all those who believed in me, especially my parents.

ACKNOWLEDGEMENTS

I would like to thank Dr. Chee-Mun Ong for this opportunity to work with him. I appreciate the confidence he exhibited in me as well the confidence I obtained through the course of this endeavor. I would also like to thank Dr. P.C. Krause and Dr. P.M. Lin for serving on my advisory committee. Furthermore, I am indebted to Purdue Electric Power Center (PEPC) for providing me with the necessary financial support. Also, I would like to extend my appreciation to Thomas Roettger for his timely advice. In addition, I would like to acknowledge the use of the figures from Mehdi Moallem's thesis to facilitate the comparative study. Most importantly, I would like to thank John R. Suriano for his generosity and support or none of the following would have been possible.

TABLE OF CONTENTS

Page

LIST OF TABLES

LIST OF FIGURES

Figure Page

Appendix
Figure Page

ABSTRACT

Toennies, Matthew Eric. M.S.E.E., Purdue University, August 1991. Computing Torque and Related Output Variables of a Switched Reluctance Machine Using a Magnetic Circuit Approach. Major Professor: Chee-Mun Ong.

The normal procedure industry employs in designing a Switched Reluctance Machine (SRM) is to construct and test a prototype to determine the machine's actual output characteristics. This procedure is time-consuming and does not allow for an accurate insight into machine dynamics. This research project consists of an analytical method for determining torque, current, and flux linkages of an SRM. A magnetic circuit modelling approach is employed for this research and the machine dimension parameters of the SRM as well as the B-H curve magnetization characteristics are utilized. The objective of the magnetic circuit modelling approach is to obtain results which will be comparable to a machine modelled using the finite element method of flux determination. The magnetic circuit analysis uses a systematic approach for calculating the reluctances of the air gap between the stator and rotor poles in a typical SRM. The end result of the magnetic circuit model is a non-linear function with respect to flux. The operating characteristics of the SRM are modelled mathematically by using first-order differential equations of flux linkages with respect to current and rotor position. Rapid speed in calculation of the operating characteristics of an SRM results from the precalculation of the flux linkage to current relationship.

CHAPTER 1
DEVELOPMENT AND OPERATING PRINCIPLES OF SWITCHED RELUCTANCE MACHINES

This thesis explains the methodology for analytical modelling of a Switched Reluctance Machine (SRM) in order to simulate its steady state performance. It begins with a brief review of the development and operating principles of Switched Reluctance Machines (SRM) in this chapter. The next two chapters describe the main aspects of the research project: magnetic modelling, analysis, and results. In chapter four, the use of the model in predicting the SRM steady state performance is presented. A comparison of the results, machine parameters and steady state waveforms, with those obtained from an earlier finite element analysis is given in chapter five. Finally, chapter six outlines the conclusion and recommendations of this study.

1.1 Definition and History of Reluctance Machines

Simply put, a stepper motor or a reluctance machine converts electrical signals into rotary motion. This motion of the machine rotor is in incremental distances called steps. Reluctance machines (RM) are known as the simplest of all electrical machines from a design standpoint. However,

the control of RM's is rather complex and it was not until the early 1980's when the RM experienced a surge in popularity. The deciding factor for any RM usage is primarily cost. The complex circuitry required by RM's for operation did not become feasible until the advent of inexpensive solid-state circuitry.

Despite the recent popularity of RM's, these machines have been in use since the early 1930's. In 1927, the British used a rotary switch version of a RM to remotely control the direction indicator for the torpedo tubes and guns on their warships [1]. However, it was not until the early 1960's that RM's proved to be useful as actuators and efficient energy converters [1].

1.1.1 Common Reluctance Machines

From this early history emerged many different kinds of RM's but the most common in use are: variable-reluctance or switched reluctance machines (SRM), solenoid-rachet type, permanent magnet types, phased-pulsed, and harmonic drive type [2]. This report will focus on SRM's which are known to be a combination of a RM with a switching invertor used for motion control [3].

1.2 Operation of Switched Reluctance Machines

The operation of a SRM is rather straight-forward if one assumes the switching operation to be an independent entity

of the machine. Figure 1 shows a typical "single-stack" SRM. The machine shown is commonly labelled to be a "8/6" configuration. The term "8/6" is a simplified way of expressing the machine arrangement of 8 stator poles and 6 rotor poles. The 8/6 is the most popular machine configuration due to geometric considerations and is the one used for the analysis [4]. Before delving into the operational characteristics of a SRM, a distinction between SRM and other machines should be made. In a SRM, the stator and rotor have salient poles of soft steel, usually M19 steel. The stator has simple concentric windings while the rotor has no windings. Torque is produced by the rotor's tendency to align with the stator-produced flux (ϕ), minimizing reluctance ($\mathfrak{R}$) and increasing the flux linkage (λ) of the stator windings [3].

1.2.1 Machine Operation Analysis

Consider phase A of Figure 1; when switch S_A is closed a current flows around the A phase stator poles creating a magnetic field which produces the flux in both the stator and rotor core and the air gaps. This flux (ϕ) is inversely proportional to the reluctance ($\mathfrak{R}$) of its path through the steel and air and is proportional to the magnetomotive force. The magnetomotive force (mmf), is related to the flux and reluctance by way of a magnetic circuit relationship. The magnetomotive force ($\mathcal{F}$), is analogous to voltage in the

Ohm's Law relationship ($V=I*R$) of a simple electric circuit. Similar to Ohm's relationship of voltage and current, the magnetic relationship can be expressed as:

$$\mathcal{F}=\phi\mathfrak{R} \tag{1.1}$$

where:

ϕ -the flux through the iron

$\mathcal{F}$ -the potential of the magnetic circuit

$\mathfrak{R}$ -the reluctance of the iron core and the air gap

Thus, when phase A is energized in Figure 1, a torque is produced on the rotor which tends to align it with the stator poles of phase A.

Next, phase B is energized by closing S_B. At the same instant in time, phase A is de-energized by the opening of S_A. Immediately, flux builds up between the BB' stator and rotor poles with the concentration of magnetic flux in the rotor points closest to the BB' stator poles. As a result, the flux lines between the BB' stator poles and the rotor pole closest are "bent" or curved as shown in Figure 2 [1]. These flux lines exhibit Maxwell stress or a proclivity to become straight lines [1]. This stress creates the clockwise torque, or restoring torque, in an effort to reduce the curvature of the flux lines and align the rotor with the BB' stator poles. In other words, the current induced flux in

the BB' stator poles will create a clockwise torque on the rotor. The rotor torque tries to restore the equilibrium state of the system such that the magnetic reluctance is decreased between the BB' stator and the rotor poles. Hence, the torque ultimately aligns the stator and rotor poles. Figure 3 shows the position of the rotor after the B phase is energized. At this point, the B phase, BB', stator and the rotor are aligned due to the magnetic attraction between both poles.

1.2.2 Switched Reluctance Machine Definition

If the switching is performed sequentially, for example phases A,B,C are fired in sequence, the rotor will rotate in incremental steps. Usually a control system of solid-state circuitry is used to energize (pulse) the stator poles. When this pulsing is synchronized with the rotor movement, the rotor turns with an average speed ($\omega_r > 0$) needed for the definition of a continuous motion device.

1.2.3 Control Feedback and Closed Loop Operation

Torque is controlled by removing current from the aligned poles and transferring the current to other pairs of stator poles. This "switching" of phases must be done rapidly and is accomplished by the control circuitry. This allows the rotor to retain its continuous motion by canceling

out the non-uniform torque. Non-uniform torque makes the rotor "jerk."

The rapid synchronization of the switching between stator poles of an SRM is achieved by positional feedback. Usually an optical encoder on the shaft decodes the rotor position for the logic to produce the next command of the microprocessor. At start up, the control system finds the relative position of the rotor and uses the position to determine which phase to energize first to begin continuous motion [1]. Control of the stator pole winding currents with respect to rotor position allows for the optimization of the torque [4]. Figure 4 shows the main components of a typical SRM control system [1]. This closed-loop operation allows for a smoother motion of the rotor.

1.3 Advantages and Disadvantages of SRM's

An SRM has many advantages: low design cost due to its simplicity (no rotor windings), high level of controllability (due to microprocessor controllers), and high torque-to-mass ratios [3]. One potential drawback of an SRM, as stated before, is the complexity of the controller which until recently prohibited mass production of SRM's [3]. On an operational standpoint, SRM's can be viewed as synchronous machines since the rotor "moves" in synchronization with the stator mmf. However, analytically, the SRM requires more complex analysis due to the double saliency, non-linearity of

pole iron saturation, and the positional feedback of the switching controller.

1.4 Applications of SRM's

Considerable progress has been made on SRM's during the last decade due to advancements in solid-state circuitry. SRM's are considered to be an excellent digital interface machine due to the "pulsing" nature of the stator mmf field. SRM's are primarily used in applications that normally use induction motor drives. More recently, RM along with SRM's have been utilized in robotics due to the accuracy of the rotational motion [5]. The wide range of applications are due to the following operational advantages: discrete motion control, non-cumulative positional error, and high torque to mass ratio [2].

1.5 Primary Objective of Research

A major hurdle to previous attempts at analytical prediction of the SRM behavior is the non-linearity since motor inductance is a function of both phase current and rotor position. Many researchers attempt to discount the saturation of the system in an effort to linearize the machine equations. By far the most accurate method of determining machine behavior is the finite element method which takes into account the non-linearity. In [6], a successful attempt was made to determine machine

characteristics using finite element analysis. The finite element method is considered "impractical" for preliminary design evaluation purposes by some because of its complexity and computing requirements [7]. Analytical methods have shown promise in estimating minimum and maximum inductances (L) of SRM's when saturation is taken into account.

The objective of this research is to determine whether magnetic circuit principles can be a reasonable alternative to a finite element analysis to determine a SRM's output characteristics during the preliminary design phase. Our study shows that the magnetic circuit analysis of a SRM can give results that are comparable to finite element analysis, sufficiently accurate for making preliminary design evaluations. Figure 5 shows a basic flowchart of the overall project plan. On one hand, the dimensions of the machine are translated to magnetic circuit equations which when solved produce machine parameters such as flux linkage (λ). On the other hand, operating conditions are implemented with the differential equations describing the machine performance characteristics to produce the steady state waveforms. The flux linkage calculated from the magnetic circuit is used as data for the steady state simulation. As the simulation progresses, the variables of the machine (θ, i) influence the magnetic circuit equation. The continuous update of the machine parameters that are functions of rotor position and current during simulation enables the output of the machine

to give a proper portrayal of its steady state characteristics. By finding flux linkage (λ) with respect to current and rotor position, torque can be determined from the change in co-energy (W_c) over a small angular displacement. In addition to torque, plots of flux linkage vs. current and vs. position are provided.

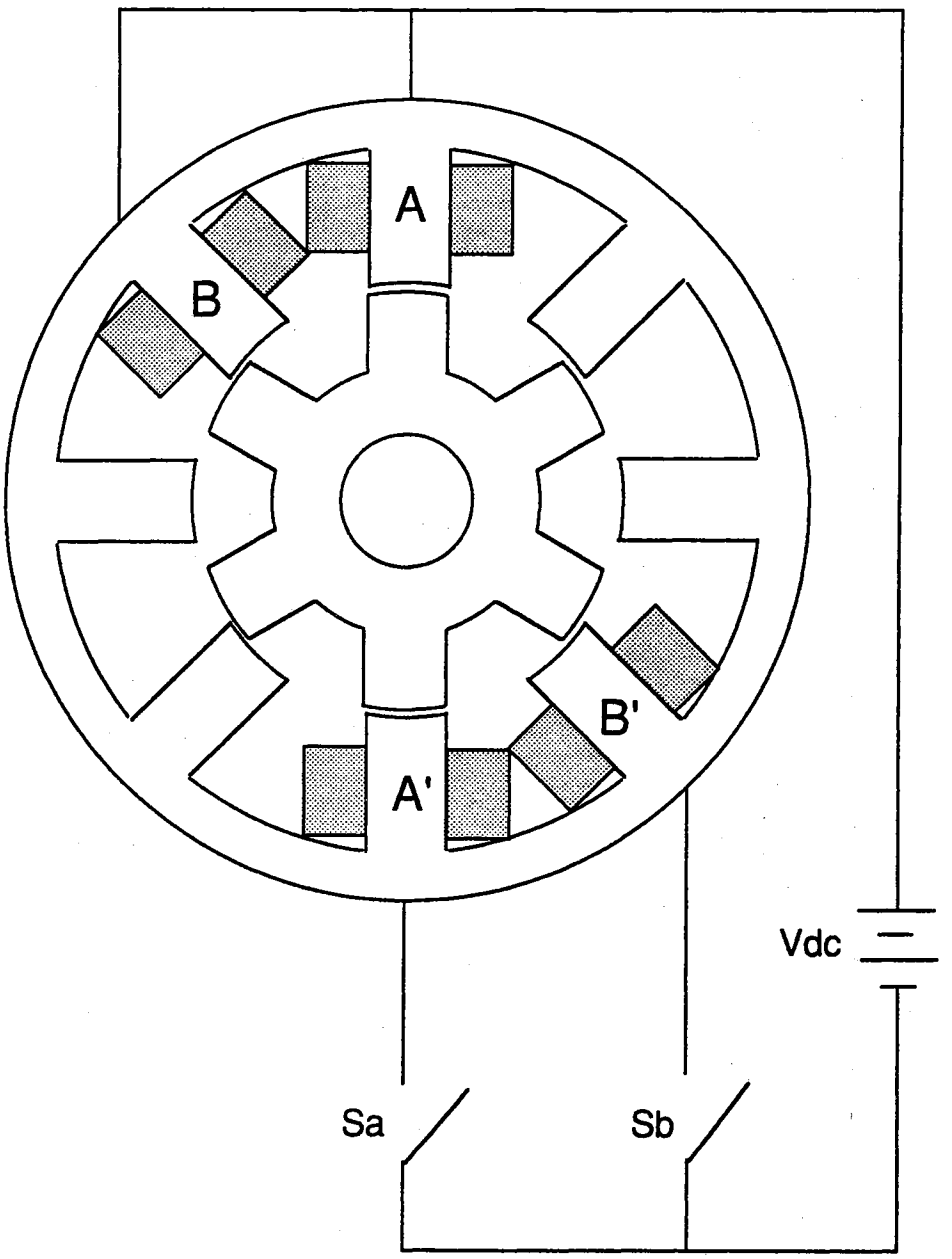

Figure 1 SRM When Phase AA' Energized

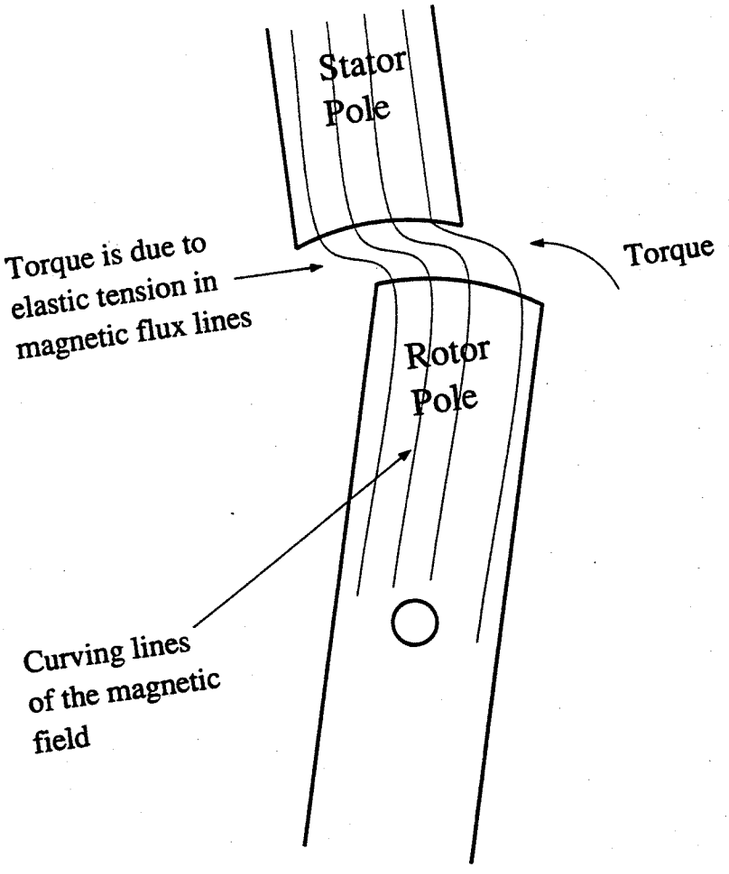

Figure 2 Maxwell Stress in an SRM

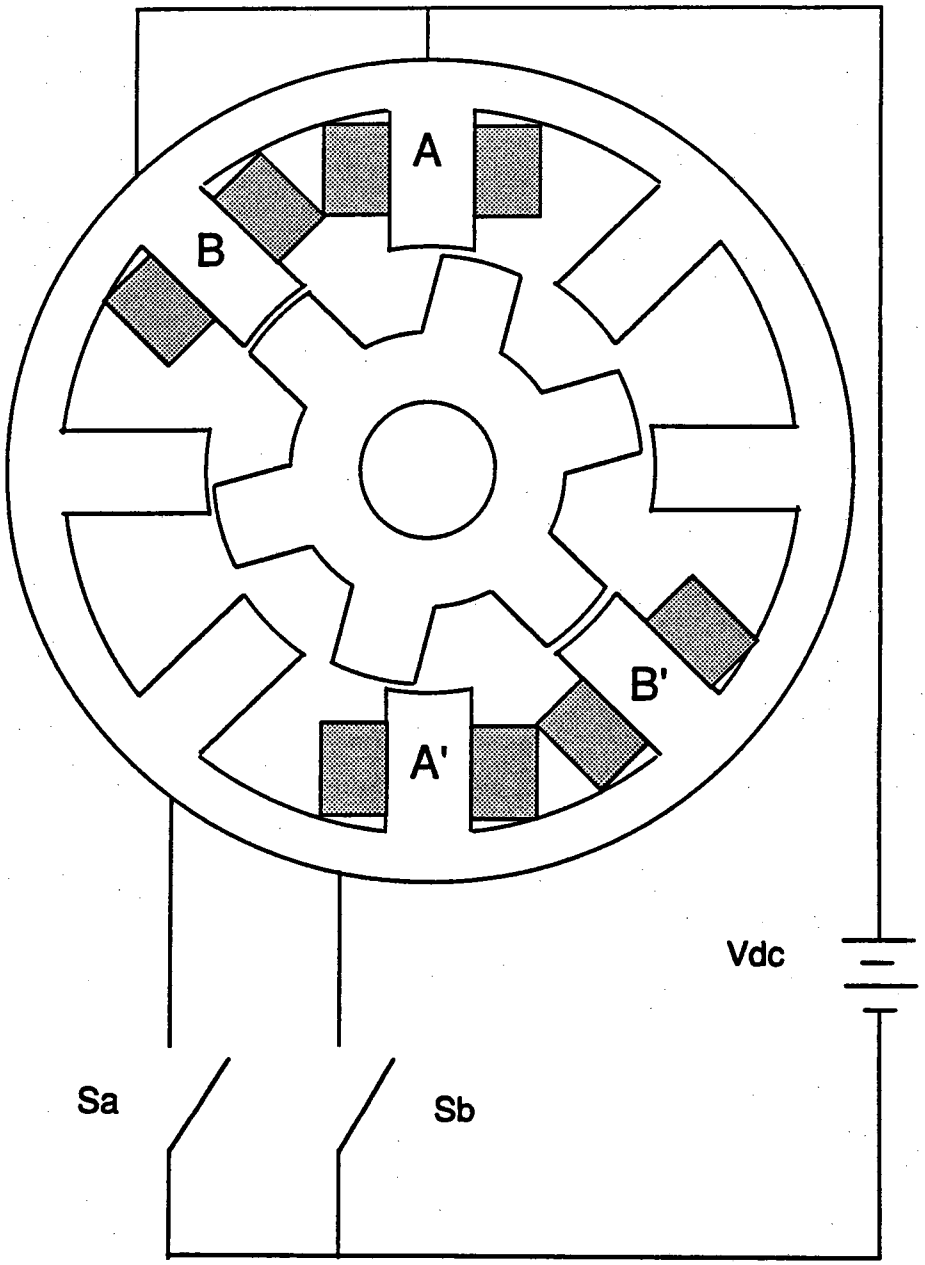

Figure 3 SRM When Phase BB′ Energized

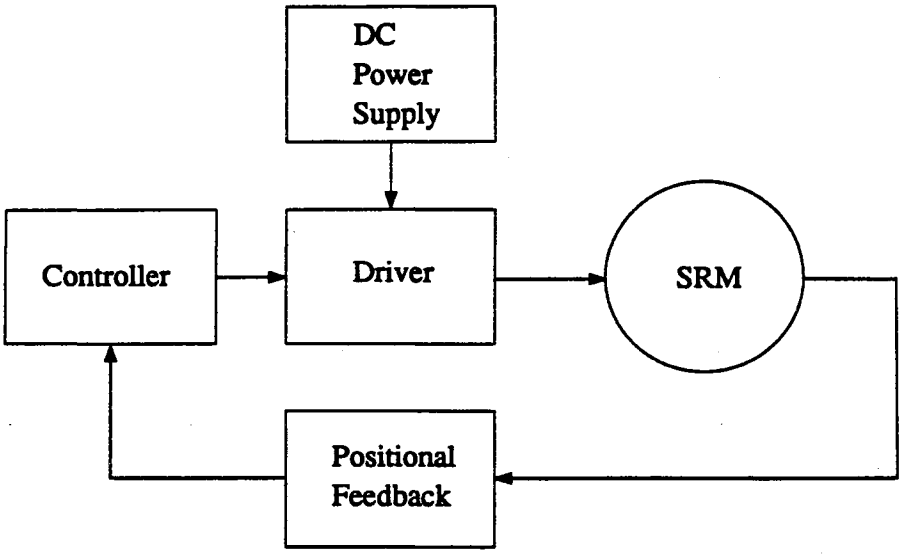

Figure 4 A Typical SRM Control System

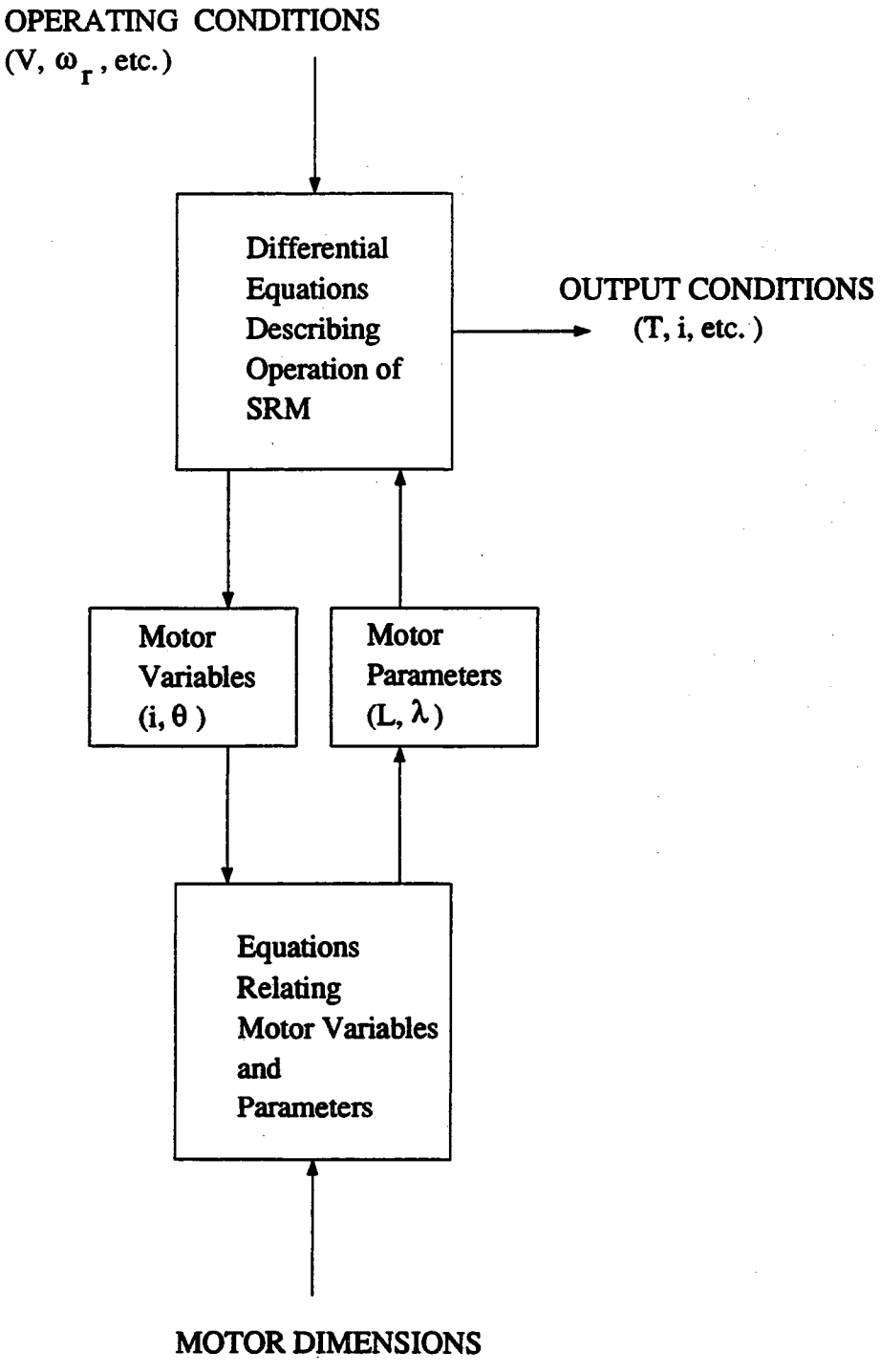

Figure 5 Flowchart of Overall Project Plan

CHAPTER 2
MAGNETIC CIRCUIT MODEL

This chapter begins with a description of the magnetic circuit approach used in this project. The magnetic circuit is undoubtedly the most important aspect of this research effort. The magnetic circuit provides a description of flux within the machine given the machine dimensions. This portion of the program provides the alternative to finite element analysis in determining the key parameters of the machine needed for proper characterization of the SRM.

The chapter is divided into three major sections. The first section discusses the calculations of the iron reluctances in conjunction with a cubic spline interpolation technique to handle the B-H characteristic of the iron. In the second section, the determination of air gap flux paths, as described in Roter's [8], is illustrated. The calculation of the fluxes enables the inductance and reluctances at various rotor positions and current levels to be found. Due to the magnetic non-linearity, an iterative procedure to compute flux is needed. The third section of this chapter describes the Newton-Raphson approach in finding the flux of the magnetic circuit. All of these steps have been incorporated in a FORTRAN program which produces the flux

linkages of a machine vs. current and rotor position, given the machine's dimensions.

2.0.1 Magnetic Circuit of SRM

Figure 6 shows the equivalent magnetic circuit of the SRM used in this project. Each distinct part of Figure 6 is represented as a lumped reluctance. The rotor itself has one reluctance but in the program it is split in halves for symmetry. There are two air gap reluctances in the circuit for both ends of the rotor pole. The air gap reluctances change with respect to rotor position. Each stator pole is represented by a reluctance. The yoke has one reluctance but it is again halved since the yoke reluctance on the other side is in parallel with the yoke shown in the Figure 6. All of these reluctances shown have to be determined before the flux of the circuit can be established.

2.1 Calculation of Iron Reluctances

A simple approach to the simulation of an SRM would be to ignore the saturation of iron, in which case the resultant magnetic circuit will be linear. Granted, ignoring iron saturation provides for easier machine simulation but will give less than accurate results. Ignoring saturation basically assumes that the flux density (B) is uniform throughout the stator and rotor poles. This cannot be possible in an SRM because of local and bulk saturation of

the iron.

When saturation of the iron is included, an accurate prediction of machine performance to within 10-15% of the results obtained from finite element analysis is possible. Since one of the stated objectives of this research is to obtain an acceptable representation of the machine for preliminary design evaluation purposes, the accuracy of the model should approach the finite element accuracy of [6]. Hence, the saturation effects of iron must be considered.

2.1.1 Saturation Characteristics of Iron

Figure 7 shows the B-H curve of the M19 steel that is used for the stator and rotor iron core of the SRM given in Appendix A. The initial portion of the curve from the origin to the "knee" is considered to be the un-saturated region of the machine iron. On this linear part of the curve, an increase in the field intensity (H) will bring about a rapid change in flux density (B). In the SRM, the field intensity is produced by the stator excitation current. That is:

$$Hl=Ni \tag{2.1}$$

where:

H -field intensity within the core

l -length of the magnetic path

N -number of turns of the stator windings

i -stator current

As the field intensity (H) increases, there is a corresponding increase in the flux density (B). This increase of B depends on the type of material. Each material, whether it is steel or air, has a different B-H relationship described by a dimensionless variable known as the permeability (μ). For example, μ for air is $4\pi \times 10^{-7}$ which gives a different curve than one for steel which is a much smaller number. The relationship between μ, B and H is:

$$B=\mu H \tag{2.2}$$

where:

B -flux density in the material

H -field intensity in the material

μ -Permeability of the material

The amount of flux through the material can be determined from the flux density and the effective cross-sectional area of the flux path.

$$\phi=BA \tag{2.3}$$

where:

ϕ -flux through the material

B -flux density in the material

A--cross-sectional area of flux path

2.1.2 Bulk and Local Saturation of Iron

Saturation can be observed in two different ways: bulk and local saturation. Bulk saturation occurs in all electric machines. At a certain point in the operation of a machine, most of the major components of the machine become saturated. Thus, if the stator, rotor and yoke are saturated then the machine is said to be bulk saturated. This saturation occurs if a current increase pushes the B-H relationship beyond the "knee" of Figure 7. Local saturation, on the other hand, occurs primarily on doubly salient machines [7]. Doubly salient machines have poles that extend out from the yoke and the rotor. These poles have tips which are involved with the transfer of magnetic flux across the air gaps. These tips become important when the machine is approaching non-alignment (rotor is leaving the stator pole area) as shown in Figure 8. Since the pole tips have a smaller cross-sectional area, they are liable to saturate quickly; even before the rest of the pole. When the excitation current is high at the point of small rotor-stator overlap, the flux through the pole tip is extremely high. This results in "intense fields [that] develop in the pole tip regions resulting in a distortion of the effective air gap [7]." This distortion causes the pole tip to locally saturate while the remainder of the iron may or may not be saturated.

2.1.3 Model of Iron Saturation

In this research, the saturation of the iron core must be taken into account if the results are to be comparable to the finite element approach of [6]. Therefore, the B-H curve in Figure 7 cannot be estimated; the curve has to be interpolated using a point-to-point case. Curve fitting of the B-H relationship would give a precise estimation of values between two known points. The cubic spline method was chosen for the interpolation since it usually provides " a superior approximation of...functions that have local, abrupt changes [9]."

The objective of the cubic spline method is to derive a third-order polynomial for each interval between a finite number of points. Using the various conditions of the method, as established in [9], an interpolation of the B-H table in Appendix B is calculated given a point in question. If the B-H table of Appendix B is interpolated with the cubic spline method using every in-between point of the B-H curve, Figure 9 shows the resultant output. In comparison to Figure 7 the curves are exactly the same which is a testimony to the accuracy of the spline method. Appendix C shows the necessary derivations for the cubic spline method used in the program.

Within the program, a connection matrix details which parts of the machine (i.e. stator poles, yoke, rotor poles, etc.) need an updated B-H approximation when the position and

current change. The air gap between the rotor and stator would not require a B-H interpolation since μ for air is assumed to be constant. On the other hand, the stator pole iron, for example, would need an updated B-H approximation for each new iteration. Based on the rotor position and the current flowing through the windings, the flux inside the stator pole will vary.

2.1.4 Implementation of Iron Saturation Model

When the flux at a particular part of the machine needs to be re-evaluated, B is solved using equation (2.3). The cubic spline subroutine in the program is called to find the value of H using the second-derivatives calculated earlier in a previous subroutine. The flowchart of this procedure is shown in Figure 10. The purpose of having separate subroutines for these functions is flexibility. The connection matrix allows the B and H values to be found only for the necessary parts of the machine. Thus, the air gaps are not calculated since the values of H are known via μ for air. This saves on the execution time of the program. On the other hand, the iron parts of the machine need to have B and H recalculated each time the current and position change.

2.1.5 SRM Iron Reluctance Calculation

The reluctances of the stator, rotor and yoke are found using the results of the cubic spline of the B-H curve for a

given "initial" flux value. The flux value is used in equation (2.3) to compute B for a specific part of the SRM. In turn, the cubic spline method interpolates H for the given flux density. Using the B and corresponding H, the reluctance ($\mathfrak{R}$) can be solved for all the iron segments. Utilizing the length and areas for each reluctance in the circuit, the reluctance can be found by:

$$\mathfrak{R}=\frac{H \cdot l}{B \cdot A} \tag{2.4}$$

where:

$\mathfrak{R}$ -reluctance of a piece of iron within the circuit

H -flux intensity of the piece

B -flux density of the piece

l -length of the flux path through the piece

A -cross sectional area of the flux path in the piece

This process would be repeated for each new value of flux found since the permeability of the iron changes with excitation current.

2.2 Calculation of Air Gap Reluctances

The flux of the magnetic circuit varies for each change in current and rotor position. More specifically, the flux paths for the air gap reluctances change for each change in rotor position. Thus, each rotor position, in the range from 0° to 45°, produces different reluctances ($\mathfrak{R}$) and, in turn,

different inductances (L). The ability to determine the reluctance of the air gap region as the rotor moves is dependent on the flux paths established. The ability to determine the inductance with respect to rotor position as the rotor moves, otherwise known as "the inductance profile," is dependent on the computation of the flux path linked by the stator winding [7].

2.2.1 Definition of Air Gap Reluctance

When the rotor is held fixed in a position with some overlap between the stator and rotor poles, the reluctance of the air gap within the overlap region is given by:

$$\mathfrak{R} = \frac{l}{\mu_o \cdot A} \tag{2.5}$$

where:

l -length of air gap

μ_o -permeability of air (constant)

A -area of the overlap air gap

The complicated reality of the SRM is that the rotor moves and the length and area of the flux paths in air will not be constant with respect to the rotor angle. Therefore, a simplistic estimation of the air gap reluctance using the value given by equation (2.5) will not be sufficiently accurate. This value does not take into account the fringing and leakage fluxes of the air gap.

2.2.2 Flux Path Determination Using Roter's Method

The reluctance of the various flux paths in the air can be determined using the approach described by Roter [8]. This technique offers simplicity and ease of use; especially for the kind of iron air boundary conditions encountered in the SRM. Roter's, in his introduction, remarked that "the precise mathematical calculation of the permeance of flux paths through air,..., is a practical impossibility [8]." (This book was written before the advent of computers and finite element analysis.) Permeance is simply the inverse of the reluctance, that is:

$$P=\frac{1}{\mathfrak{R}} \tag{2.6}$$

where:

$\mathfrak{R}$ -reluctance

P -permeance

Roter's uses permeances in place of reluctances due to ease of use. If many paths are in parallel, it is simpler to add up the permeances. Roter's justifies his method by acknowledging that permeance calculations "are carried out by making simplifying assumptions regarding the flux paths...[8]."

For example, Figure 11 shows the flux in a SRM with its rotor off alignment from the stator. The flux plot was obtained from a finite element solution in [6] and gives a

fairly accurate portrayal of the machine flux paths. Using Roter's method of permeance approximation, we can estimate the P between the stator and the rotor in Figure 11 using Roter's approach.

Using the finite element result as a guide, Figure 12 shows how flux paths in a SRM can be approximated. Figure 12 shows five different flux paths; the total comprising the permeance of the air gap region. The paths are numbered from 1 to 5. Path 3 is the easiest to determine since it is a straight-forward rectangle. The permeance of path 3 can be found by using equation (2.5). Paths 2 and 4 are trickier than path 3. The permeance cannot be found using the simple straight line concept of path 3. However, path 2 can be described as a quarter-circle. Path 4 is the mirror image of path 2 so what applies to path 2 is applicable to path 4 too. Realizing that path 2 changes in connection with α, the equation describing the permeance of paths 2 and 4 is:

$$P(2) = P(4) = \frac{\left(\mu \cdot \left(\frac{g \cdot z}{2.0}\right)\right)}{(1.29 \cdot g)} \qquad (2.7)$$

where:

P -permeance of path

g -air gap dimension

μ -permeability of air

z -axial length of machine

Paths 1 and 5 can be solved using the very same methodology

as equation (2.7). Figure 12 shows that path 1 (again path 5 is a mirror image of path 1) resembles a "doughnut-shaped" quarter circle. Path 1 is highly dependent on α which changes with respect to θ_r. As the rotor moves further away from alignment, path 1 becomes larger. Making the necessary geometrical deductions the permeance of path 1 and 5 can be described as:

$$P(1) = \frac{(\mu \cdot x1 \cdot z)}{\left(\frac{(x1 + g)\cdot(1.57 + \theta_r) + (g \cdot 1.57)}{2.0}\right)}$$

$$P(5) = \frac{(\mu \cdot x2 \cdot z)}{\left(\frac{(x + g)\cdot(1.57 + \theta_r) + (g \cdot 1.57)}{2.0}\right)} \qquad (2.8)$$

where:

P - permeance of path

g -air gap dimension

$$x1 = \frac{\beta_r}{2}\cdot r1 - \frac{\alpha}{2}\cdot r1 - g - (\theta_r \cdot r1)$$

$$x2 = \frac{\beta_r}{2}\cdot r1 - \frac{\alpha}{2}\cdot r1 - g$$

θ_r -angle of rotor with respect to origin

μ -permeability of air

z -axial length of the rotor

Many of the path lengths are averages between the highs and lows of the corresponding dimension. The derivations of some

of these expressions for the SRM are illustrated in Appendix D. As the rotor position changes, a different model with additional or fewer flux paths may be necessary. In addition, there are SRM's, such as the one used in this project, that have different widths of rotor and stator poles. The difference in pole width complicates matters but are worked out too.

Together with the reluctances found for the iron core segments, the complete circuit of the reluctances for the magnetic system can be determined in this manner. Therefore, all of the reluctances are known for Figure 6. As mentioned before, the reluctances of the circuit in Figure 6 vary with the rotor angle, and also the level of current excitation.

2.2.3 Inductance Profile Using Air Gap Reluctances

A good way of showing the relationship between the air gap reluctance and the angular position is to plot an inductance profile. Inductance is "a measure of the ability of a coil to oppose any change in current through the coil and to store energy in the form of a magnetic field [flux] in the region surrounding the coil [10]." A relationship between stator winding inductance (L) and the reluctance ($\mathfrak{R}$) of the magnetic circuit can be found by beginning with the usual equation for inductance, which is:

$$L=\frac{\lambda}{i} \tag{2.9}$$

where:

L -inductance of stator winding

λ -flux linkage of stator winding

i -current in stator winding

Utilizing equation (2.13) and equation (2.1), equation (2.9) can be re-written as:

$$L=\frac{N^2\phi}{\mathcal{F}} \tag{2.10}$$

where:

$\mathcal{F}$ -mmf in Amperes-turns

N -number of turns of coil around stator pole

ϕ -flux linked by the stator winding

Using equation (1.1), equation (2.10) can be finalized into a relationship between inductance and reluctance as:

$$L=\frac{N^2}{\mathfrak{R}} \tag{2.11}$$

where:

$\mathfrak{R}$ -reluctance of material in question

The inductance profile for the entire range of rotor position can be found once the corresponding reluctances are known. In addition, the flux linkages for each of the rotor

positions can be found by multiplying equation (2.11) by the current used. Figure 13 shows the inductance profile of the SRM described in Appendix A at 10A. The profile from -45° to 0° is simply the mirror image of Figure 13 by virtue of the geometric symmetry. At 0° or the aligned position, the reluctance of the air gap is very low due to the small length and large overlap area of the gap. As the rotor moves away from the totally aligned position, the reluctance of the air gap increases due to the decrease in overlap and the increase in path length of the fringing fluxes. Figure 13 shows the rise in reluctance as the rotor angle increases. As the reluctance increases, the inductance declines since flux flows less freely. At 45°, the reluctance is so elevated that the inductance, based on equation (2.11), is very small due to the limited flux flow through the air gap region. The maximum and minimum inductance, L_{max} and L_{min}, are important parameters in the prediction of the SRM performance.

Due to the lack of numerical information given in [6], a quantitative comparison between the inductance profile found using Roter's method and that given in [6] cannot be done. However, in [11], the necessary numerical data was given for a different machine and a quantitative comparison of the Roter's method inductance profile can be made against the finite element inductance profile. The machine data for [11] is given in Appendix E. Figure 14 shows the graphical comparison at 10A. Obviously, Roter's method is subject to

error in approximating the flux paths and that explains the difference in curves. The finite element method takes into account all possible flux paths (as shown in Figure 11) whereas the Roter's method cannot. Any flux paths not included in the analysis automatically increases the predicted reluctance from Roter's method. This increase in the reluctance explains the difference in the inductance profiles shown in Figure 14. Given the error of the inductance profile for the machine described in Appendix E, the same assumption can be made about the machine used in Appendix A.

2.2.4 Inclusion of Leakage Inductances using Roter's Method

In general, most magnetically coupled circuits have leakage fluxes. The leakage fluxes from stator pole to stator pole and stator pole to yoke coupled with the magnetizing flux form part of the total flux linked by the stator winding. Though they form only a small part of the total flux when the overlap between stator and rotor poles is finite, its role in the non-overlapping region is a major one.

In an effort to match the finite element inductance profile, approximate leakage paths from stator pole to stator pole and from stator pole to the yoke shown in Figure 12 are included. Path RP travels from the top stator pole to the adjacent stator and path RY ranges from the stator to the

yoke above. Both path lengths are independent of rotor position; they are a function of the fixed angles and lengths of the machine dimensions listed in Appendix A. The equations for the reluctances of these leakages are:

$$RP=\frac{\left(\frac{((R1+g)\cdot\delta)+(((\frac{SL}{2})+R1+g+(2((\frac{SL}{2})TAN(\frac{\beta_s}{2}))))\delta)}{2}\right)}{(\frac{SL}{2})\cdot\mu\cdot Z} \qquad (2.12)$$

$$RY=\frac{\left(\frac{(SL\cdot\gamma)+(\frac{SL}{2.0})\cdot\gamma}{2.0}\right)}{\left(\frac{SL}{2.0}\cdot z\cdot\mu\right)}$$

where:

γ -angle between stator pole and yoke

δ -angle between tips of both stator poles

R1 -radius of rotor pole

g -air gap length

SL -stator pole length

z -SRM axial length

μ -permeability of air

The flux paths found in equation (2.12) can be used to represent the leakage flux that occurs whenever the windings are energized. The leakage inductance paths are lumped together with the magnetizing inductance paths to establish the total inductance of the system. The magnetizing inductance includes the iron core sections of the SRM and is

subject to saturation. The total inductance can be determined from the total flux:

$$\phi_{tot}=\phi+L_l \cdot i \qquad (2.13)$$

where:

ϕ -flux for parts of the SRM subject to saturation

$L_l \cdot i$ -flux for leakage paths through air

2.2.5 Inductance Profile Using Leakage Paths

The inclusion of these leakage flux paths contributes to a slight increase in the inductance of both the aligned and non-aligned stages of the machine inductance profile. A comparison of the inductance profiles in Figure 14 and Figure 16 at 10A show a slight improvement when the leakage paths are included.

2.3 Calculation of Magnetic Circuit Flux

The purpose of finding the reluctances of the assumed flux paths in the SRM is to employ them in the equivalent magnetic circuit shown in Figure 6 that we will use to solve for the flux linked by the stator winding. If equation (1.1) describing the circuit is satisfied then the stator winding flux linkage (λ) can be calculated for a specific value of rotor position (θ) and current (i). The relationship between flux (ϕ) and the flux linkage can be described as:

$$\lambda = N\phi \tag{2.14}$$

where:

λ -stator winding flux linkage

ϕ -flux linked by stator winding

N -number of turns of stator winding

The flux linkage, in turn, can be used to describe the other SRM output characteristics such as torque.

2.3.1 Newton-Raphson Method

The equivalent circuit shown in Figure 6 is non-linear because iron saturation is modelled. Therefore, an iterative numerical method is required to solve the non-linear flux equations. The Newton-Raphson (N-R) method was chosen because it offers fast convergence and acceptable accuracy. The N-R method, however, requires the derivative of the non-linear function or the Jacobian to refine the solution. The derivatives are contained in the Jacobian matrix [12]:

$$J = \begin{bmatrix} \frac{\partial f}{\partial x_1} & \frac{\partial f}{\partial x_2} \\ \frac{\partial f}{\partial x_1} & \frac{\partial f}{\partial x_2} \end{bmatrix} \tag{2.15}$$

where:

J -Jacobian matrix variable

f -function of system

x_1 and x_2 -unknown variables

The N-R iterative equation to solve for flux is [12]:

$$X_{n+1}=X_n-J^{-1}\cdot F(X_n) \tag{2.16}$$

where:

X_{n+1} -next value of unknown variable

X_n -present value of unknown variable

J^{-1} -inverse of the Jacobian

$F(X_n)$ -value of function evaluated with the present value of the unknown variable

When $F(X_n)$ falls within some predefined tolerance (usually set around 0.0001), the iteration can be stopped; this signifies that the unknown variable is acceptably close to the solution.

2.3.2 Magnetic Circuit Equations for N-R Method

In the case of finding the flux, the N-R equation is:

$$\boldsymbol{\phi}_{n+1}=\boldsymbol{\phi}_n-J^{-1}\cdot F(\boldsymbol{\phi}) \tag{2.17}$$

The equation to be solved is the relationship between flux and mmf described by equation (1.1) of the equivalent circuit shown in Figure 6. The flux linkage program has been written to accommodate up to five flux paths. Therefore, Figure 17 shows the full magnetic circuit representation of the SRM. With five flux paths there are five equations with five

unknowns. One equation for each loop through a leg of the magnetic circuit. The equations are as follows:

$$\begin{aligned} f_1 &= \Re_1\phi_1 - 2Ni + \Re_y(\phi_1+\phi_2+\phi_3+\phi_4+\phi_5) = 0 \\ f_2 &= \Re_2\phi_2 - 2Ni + \Re_y(\phi_1+\phi_2+\phi_3+\phi_4+\phi_5) = 0 \\ f_3 &= \Re_3\phi_3 - 2Ni + \Re_y(\phi_1+\phi_2+\phi_3+\phi_4+\phi_5) = 0 \\ f_4 &= \Re_4\phi_4 - 2Ni + \Re_y(\phi_1+\phi_2+\phi_3+\phi_4+\phi_5) = 0 \\ f_5 &= \Re_5\phi_5 - 2Ni + \Re_y(\phi_1+\phi_2+\phi_3+\phi_4+\phi_5) = 0 \end{aligned} \qquad (2.18)$$

where:

$\Re_n$ $-\Re_{stator}+\Re_{airgap}+\Re_{rotor}+\Re_{rotor}+\Re_{airgap}+\Re_{stator}$

$\Re_y$ -reluctance around one half of the yoke

N -number of turns stator winding

i -stator winding current

ϕ_n -flux through path n^{th} in the air gap

2.3.3 Elements of the Jacobian Matrix for N-R Method

The elements of the Jacobian matrix are as follows:

$$\frac{\partial f_i}{\partial \phi_j} = \frac{\partial \Re_y}{\partial \phi}(\phi_1+\phi_2+\phi_3+\phi_4+\phi_5) + \Re_y \quad for\ i \neq j$$

$$\frac{\partial f_i}{\partial \phi_j} = \phi_i \frac{\partial \Re_i}{\partial \phi_j} + \Re_i + \frac{\partial \Re_y}{\partial \phi}(\phi_1+\phi_2+\phi_3+\phi_4+\phi_5) + \Re_y \quad for\ i = j \qquad (2.19)$$

where:

i -number of equations

j -number of flux paths

There are two computational problems with equation (2.19).

First, the yoke $\frac{\partial \mathfrak{R}_y}{\partial \phi}$ must be taken with respect to all flux paths passing through. Therefore, when $\mathfrak{R}$ is calculated, the flux density (B) used takes into account all the pertinent flux paths passing through the yoke. The programming of this complexity was simplified by using a connection matrix to describe the number of flux paths through each reluctance shown. In other words, the $\phi \frac{\partial \mathfrak{R}}{\partial \phi} + \mathfrak{R}$ was solved for each reluctance of Figure 17, except for the air gaps reluctance because of the absence of saturation. Second, $\frac{\partial \mathfrak{R}}{\partial \phi}$ is not immediately known. Some method has to be formulated to find this value. Appendix F shows the necessary derivations for $\frac{\partial \mathfrak{R}}{\partial \phi}$.

Once the Jacobian is computed, the N-R iteration can proceed. Figure 18 displays a flowchart of the steps taken to iterate for the fluxes. Once the fluxes are found for a given rotor position and stator current, the total flux linkage can be calculated from equation (2.14).

Overall, the use of this flux linkage program is to compute the flux linkage (λ) vs. current (i) and rotor position (θ) for a given set of machine dimensions. Later in this thesis, the computed flux linkage data of the machine

is utilized in producing the steady state characteristics of the SRM.

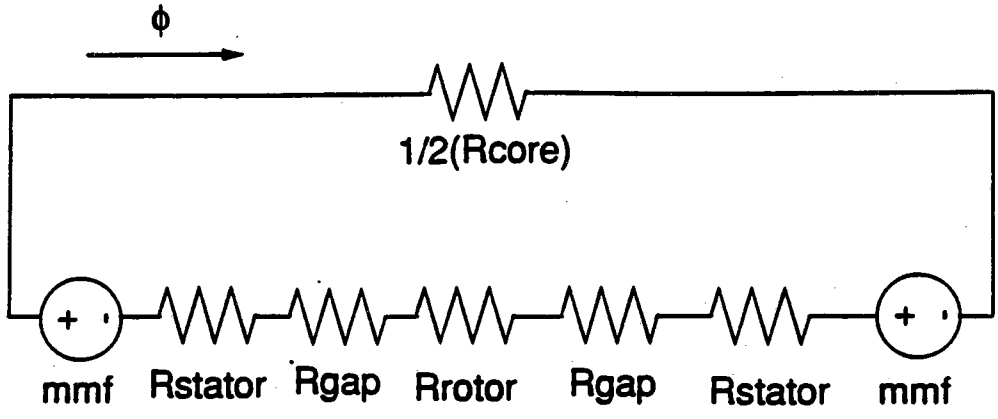

Figure 6 Equivalent Magnetic Circuit of SRM

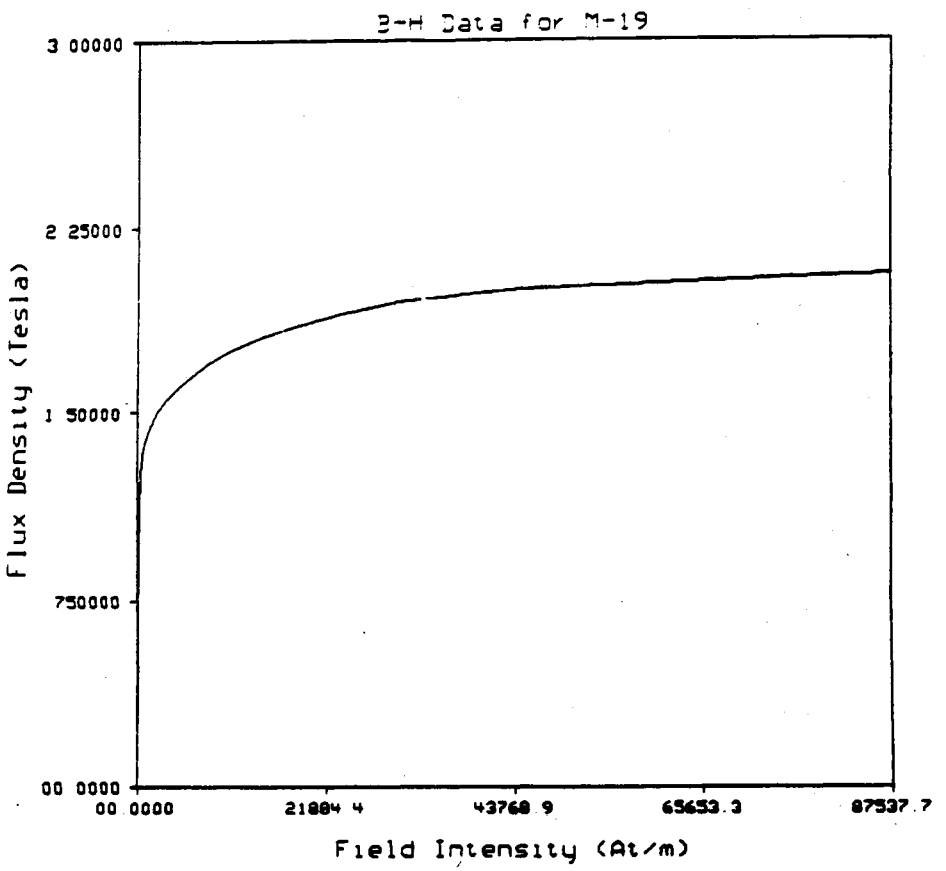

Figure 7 B-H Curve for M19 Steel

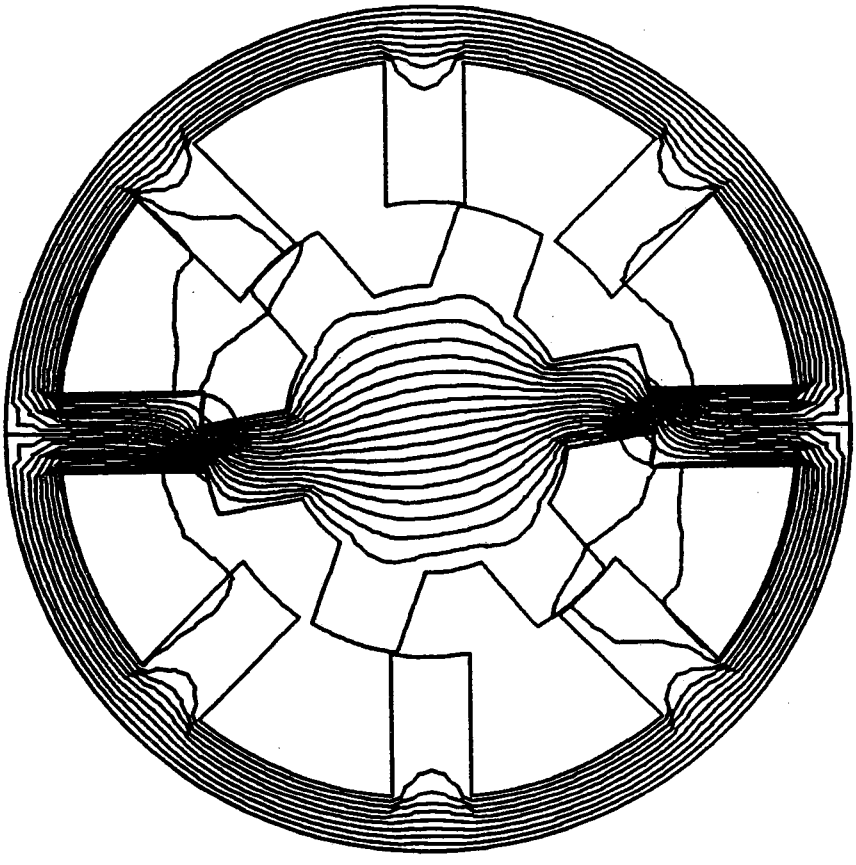

Figure 8 Flux Paths at 10° from Finite Element Analysis
(From reference [6])

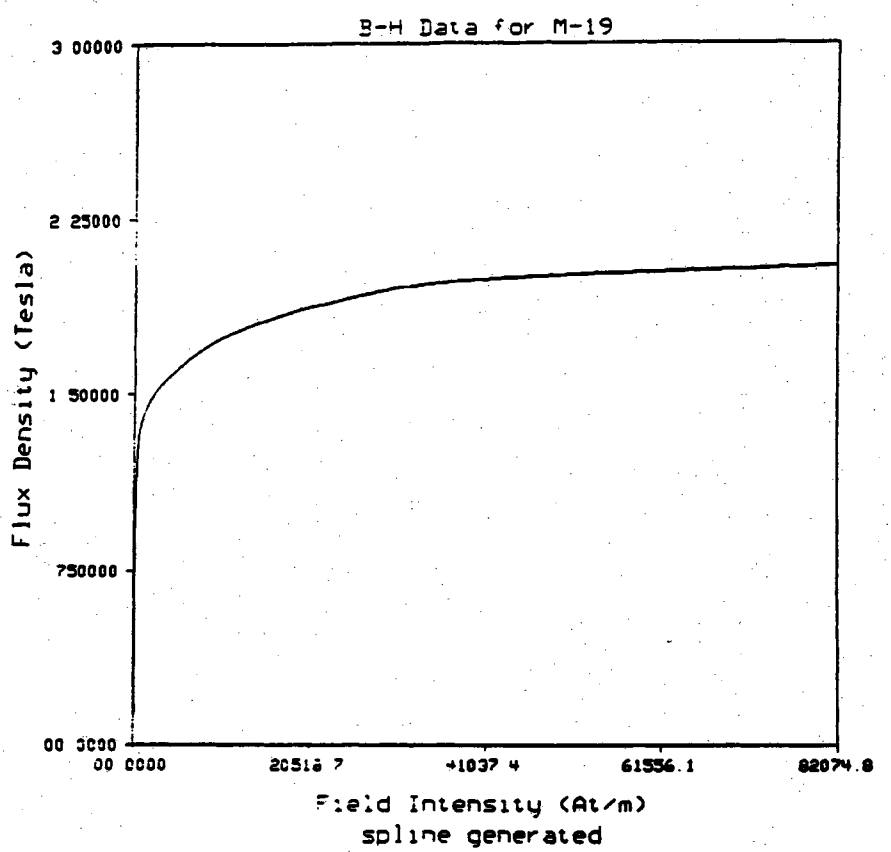

Figure 9 Cubic Spline Generated B-H Curve

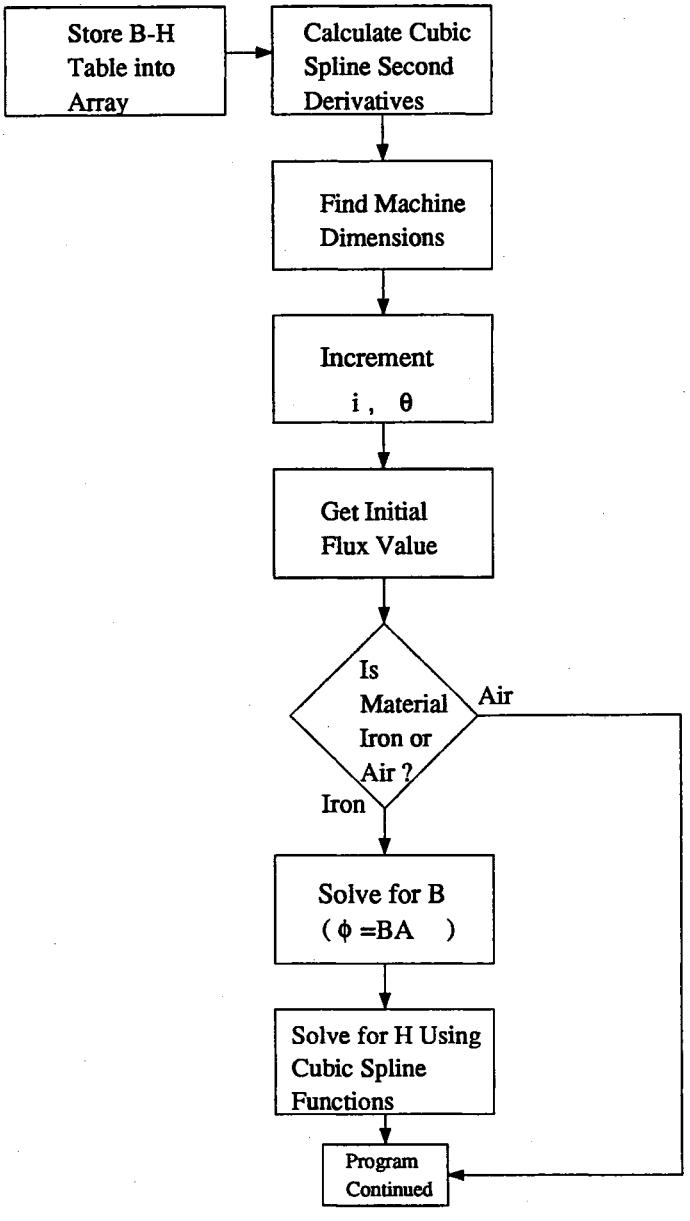

Figure 10 Flowchart of Cubic Spline Procedure

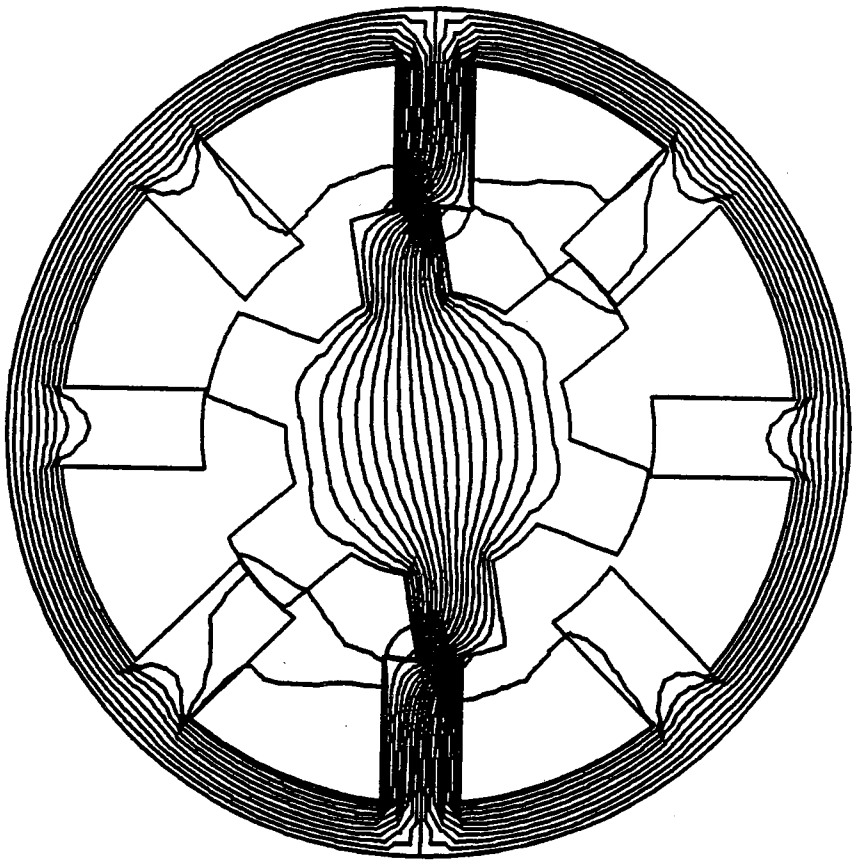

Figure 11 Finite Element analysis of Flux Paths
(From reference [6])

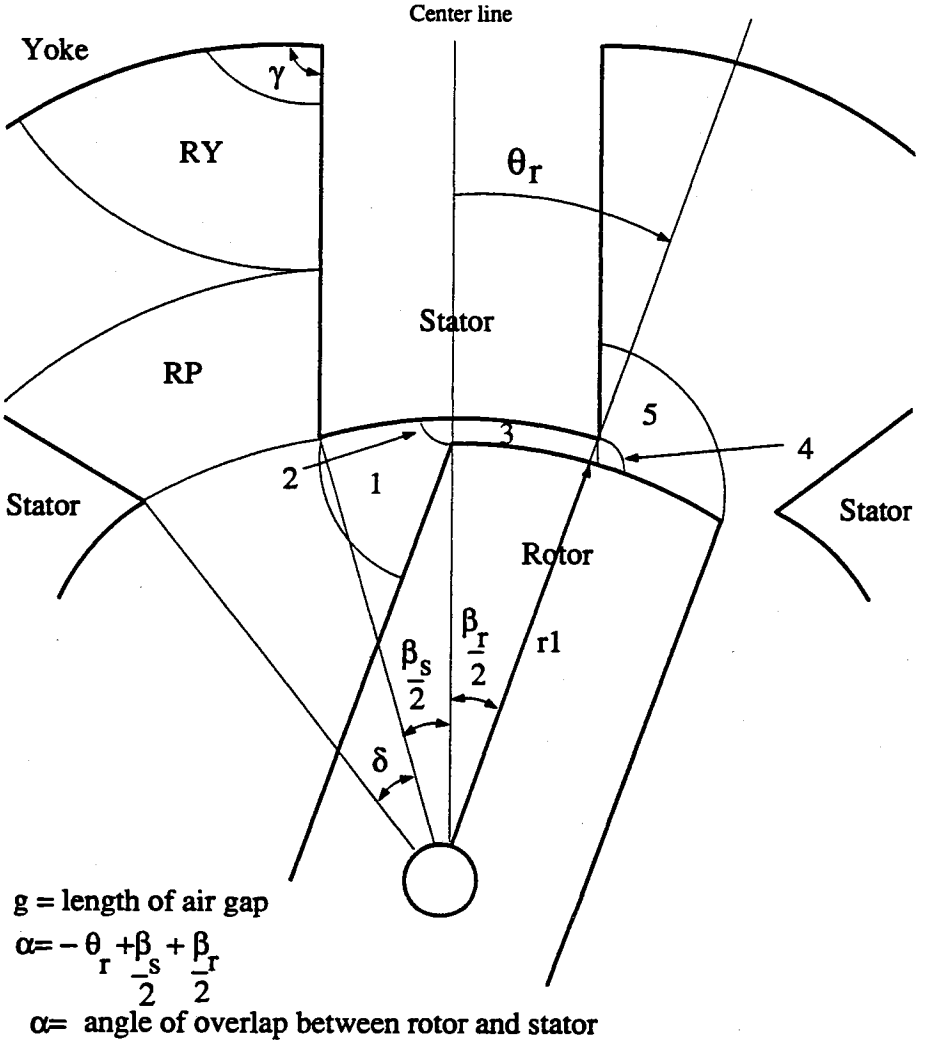

Figure 12 SRM Flux Paths Analyzed using Roter's Method

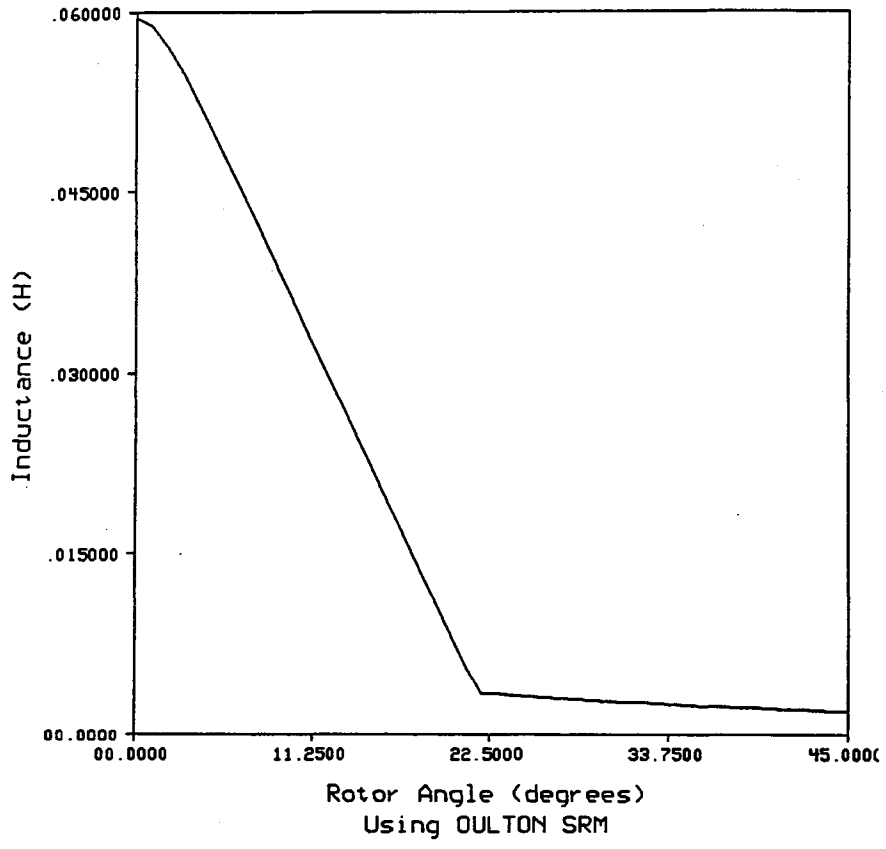

Figure 13 Inductance Profile at 10A for Appendix A SRM

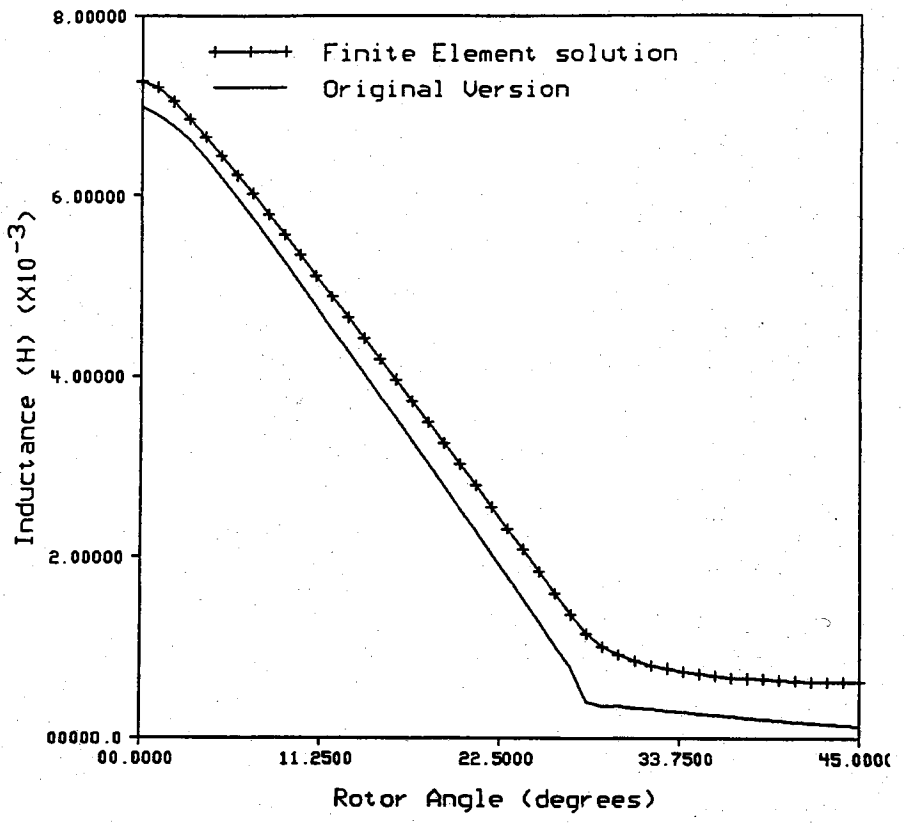

Figure 14 Inductance Profile at 10A for Appendix E SRM

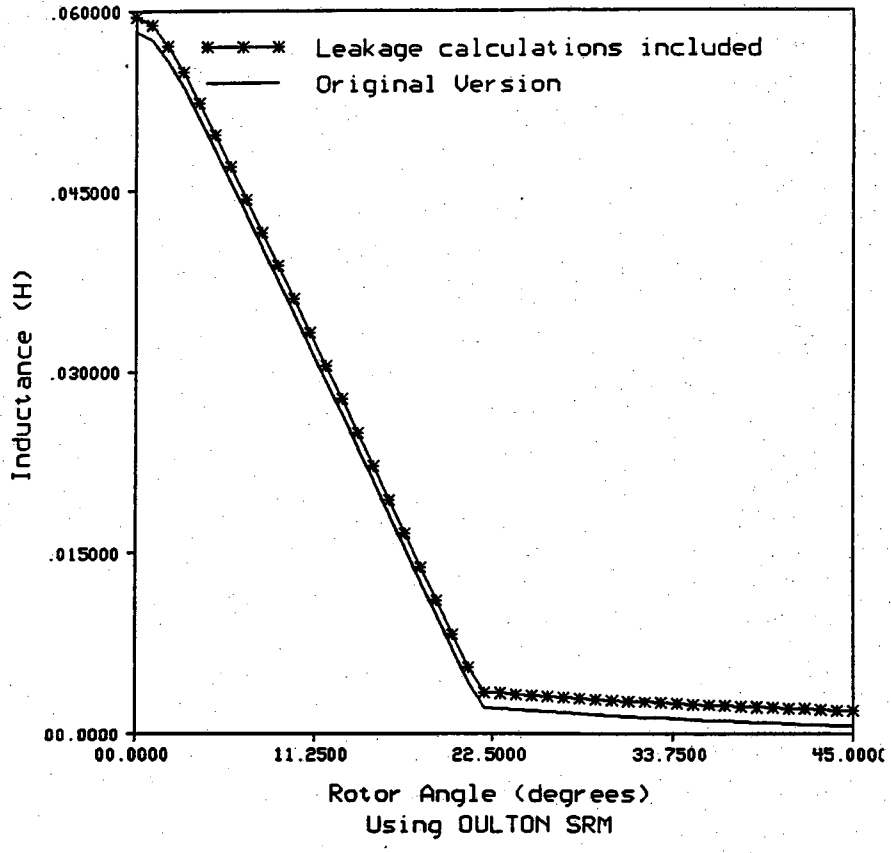

Figure 15 Inductance Profile at 10A for Appendix A SRM

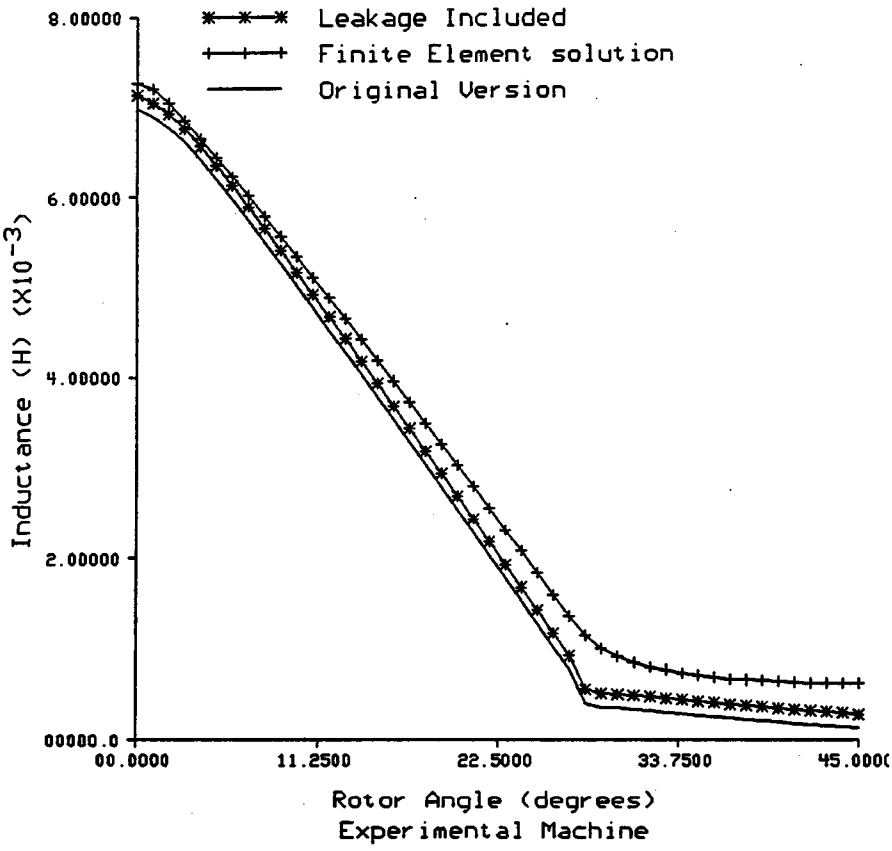

Figure 16 Inductance Profile at 10A for Appendix E SRM

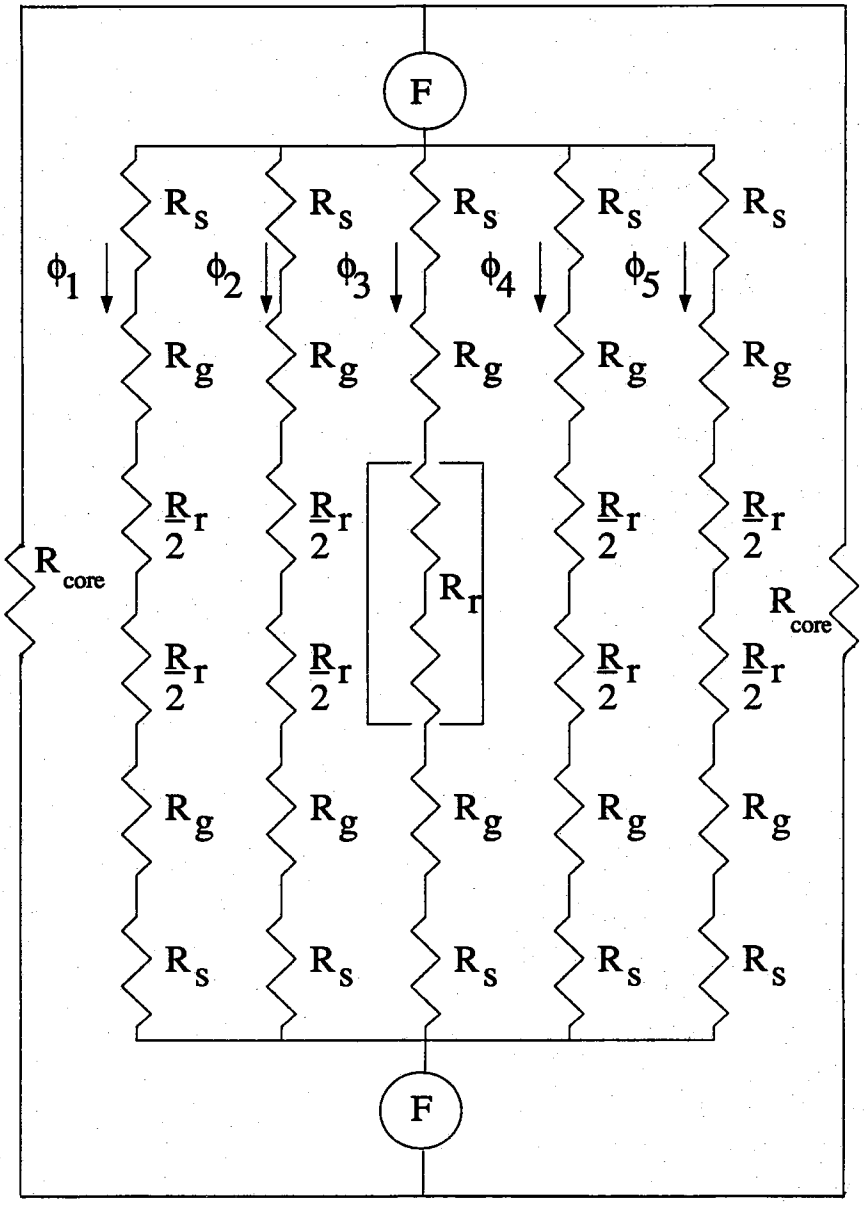

Figure 17 Magnetic Circuit for SRM

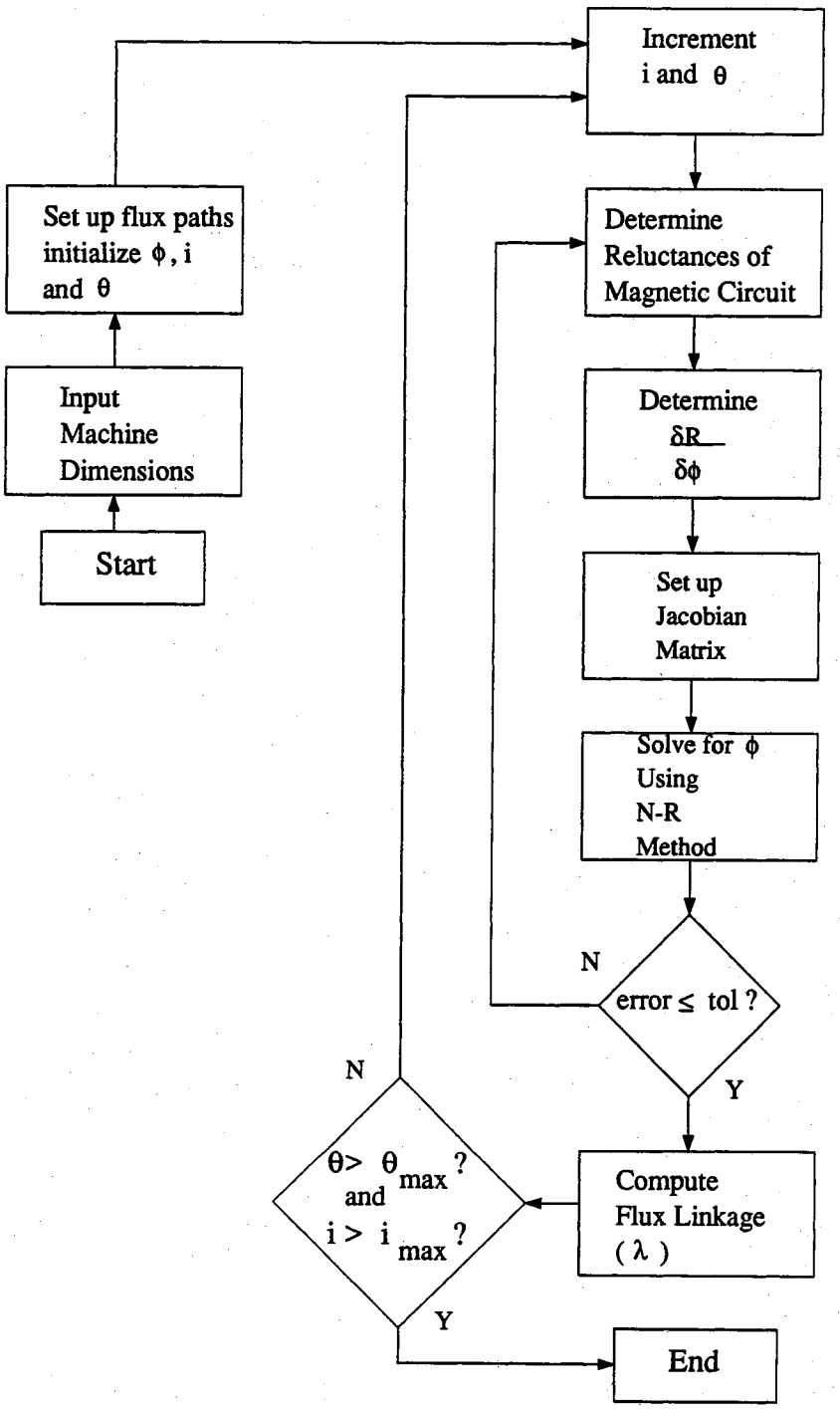

Figure 18 Flowchart of N-R Procedure

CHAPTER 3
COMPARISON OF FLUX LINKAGE PROGRAMMING RESULTS

As mentioned in the previous chapter, the objective of the flux linkage program is to determine the machine flux linkage (λ) with respect to current (i) and rotor position (θ_r) for a given machine. The flux linkage (λ) is the key parameter that characterizes the machine. It can be used in a dynamic simulation to obtain the stator current and torque waveforms. In this chapter we will compare the computed λ with that obtained from a finite element analysis of the same machine to ascertain the accuracy of the result. Earlier on, the results of the finite element analysis have been validated by a similar comparison with experimentally measured results.

3.1 Finite Element Flux Linkage Profile Description

Figure 19 shows the three-dimensional plot of λ vs. current and rotor position from a finite element calculation [6]. This figure can be called a flux linkage profile in the same sense as the inductance profile discussed in the last chapter. As shown, the closer the rotor is to full alignment with the stator pole, the higher the λ or the amount of flux

linking the stator and rotor poles. As the rotor pole moves away from alignment (full alignment is at θ_r=0°), the angle θ_r in the plot increases. This increase in θ_r means the air gap flux pathways are longer resulting in higher reluctances. The rise in circuit reluctance lowers the stator flux for a given ampere-turn ($\mathcal{F}$). As the current in the stator winding rises, the mmf increases proportionally owing to the relationship of equation (2.1). The higher winding currents increases the flux linking the stator pole due to the proportional growth in the mmf. This increase in the λ occurs for all rotor positions shown in Figure 19.

3.2 Results of the Analytical Flux Linkage Profile

Figure 20 shows the λ vs. i and θ_r found using the flux linkage program. The profile in Figure 20 appears similar to that shown in Figure 19. Based on their similarity, the validity of the magnetic circuit modelling approach of a SRM may be confirmed. However, there are distinct differences of the two profiles around the 21° region as well as the peak value. In Figure 20, the flux linkage drops sharply as θ_r approaches 21°. In addition, the flux linkage does not change considerably over the range of rotor position between 0° and 20°. The peak value of Figure 20 is higher than that of Figure 19. This overall increase in the flux linking the windings can be attributed to the rough estimate of the

leakage flux paths.

This discrepancy between Figure 20 and Figure 19 suggests a basic limitation of the analytic magnetic circuit model. Simply put, the local saturation of the rotor and stator pole tips as these poles part were not taken into account. Figure 21 shows the finite element model of the SRM at 20° from the origin [6]. The pole tips of the rotor and stator poles closest to each other show tremendous amounts of flux passing through. These tips are obviously highly saturated. However, even though the tips of the poles are saturated, the rest of the pole may still be unsaturated. Therefore, the pole tips experience local saturation while the remainder of the poles are not saturated; bulk saturation of the machine has not been reached. To include local saturation in the flux linkage program would be complicated because of the difficulty in identifying the region of local saturation and the saturation level.

Since local saturation of the pole tips was not taken into account in our method, the tips could accommodate more flux than they can actually absorb. In other words, the values of computed flux and corresponding flux linkages are on the high side. This can be seen from Figure 20 which displays a nearly constant λ until about 21° when non-alignment occurs. However, as soon as the overlap between the rotor and the stator poles ceases, the reluctance increases and the inductance decreases rapidly. With local

saturation, such a drop in inductance would be more gradual and would happen even when the overlap is still finite.

The abrupt change in λ of Figure 20 around 21° corresponds to the "elbow" of the inductance profile in Figure 15. This "hiccup" is hard to avoid using Roter's methodology due to the analytical nature of the modelling procedure. In other words, Roter's method cannot account for all the leakages within the SRM system. In addition, the lack of a "smooth" transition between the aligned and non-aligned regions of the flux linkage curve can be attributed to the difficulty of "meshing" the aligned and the non-aligned portions of the analytical method of estimation.

The results in this chapter show that the magnetic circuit approach used is feasible and gives acceptable results. However, the accuracy of the simulation will be compromised due to the limitations in gauging the pole tip saturation and the paths of the leakage fluxes.

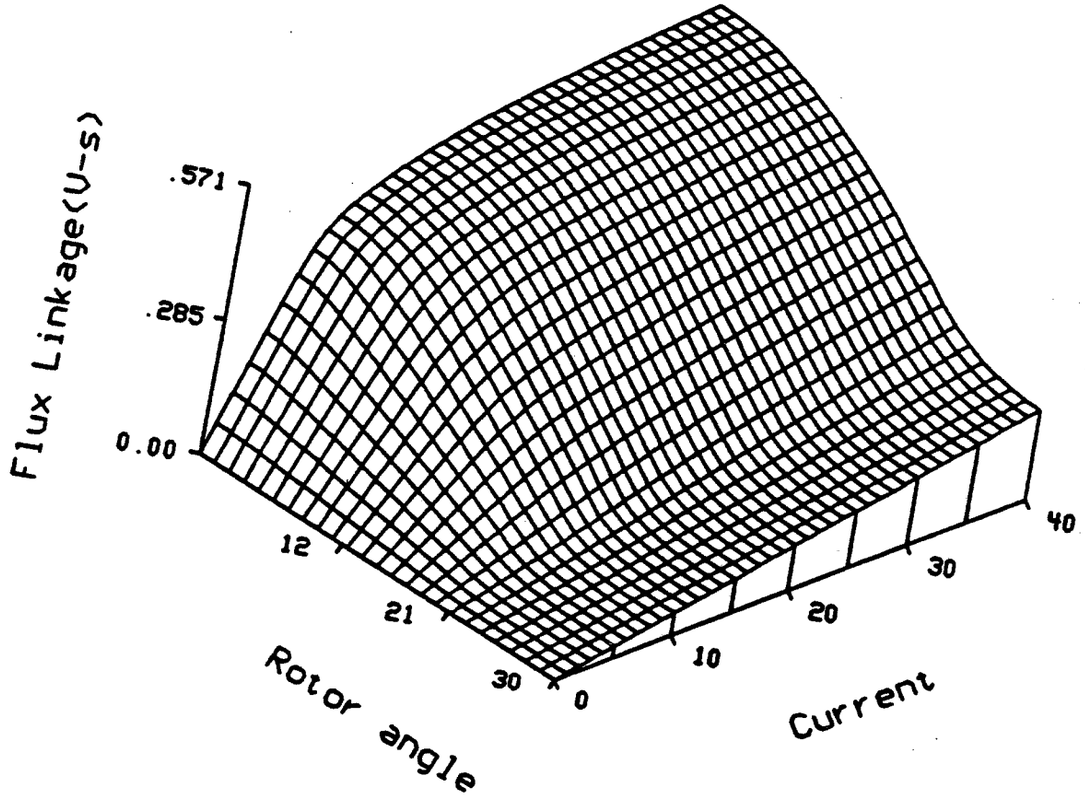

Figure 19 Flux Linkage Profile from Finite Element
(From reference [6])

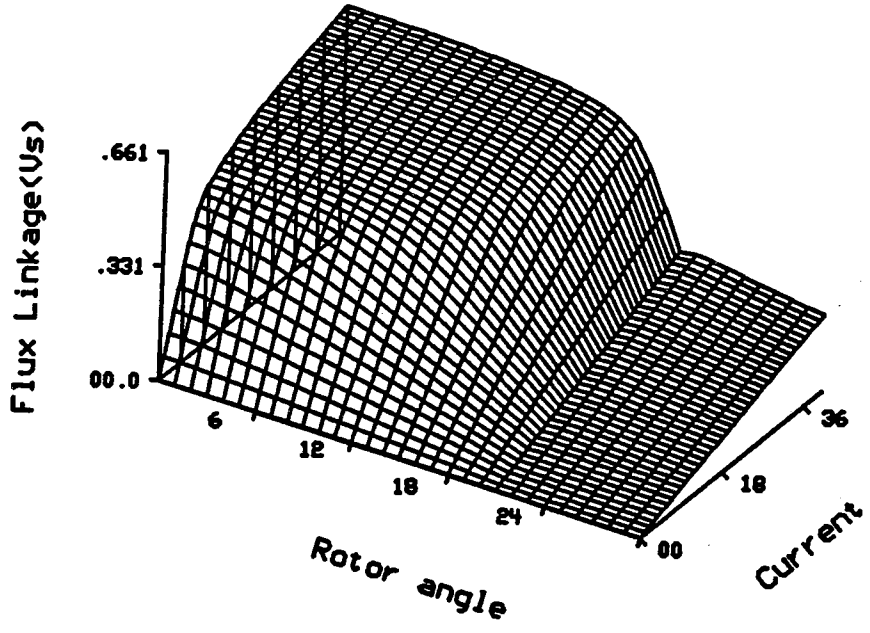

Figure 20 Flux Linkage Profile

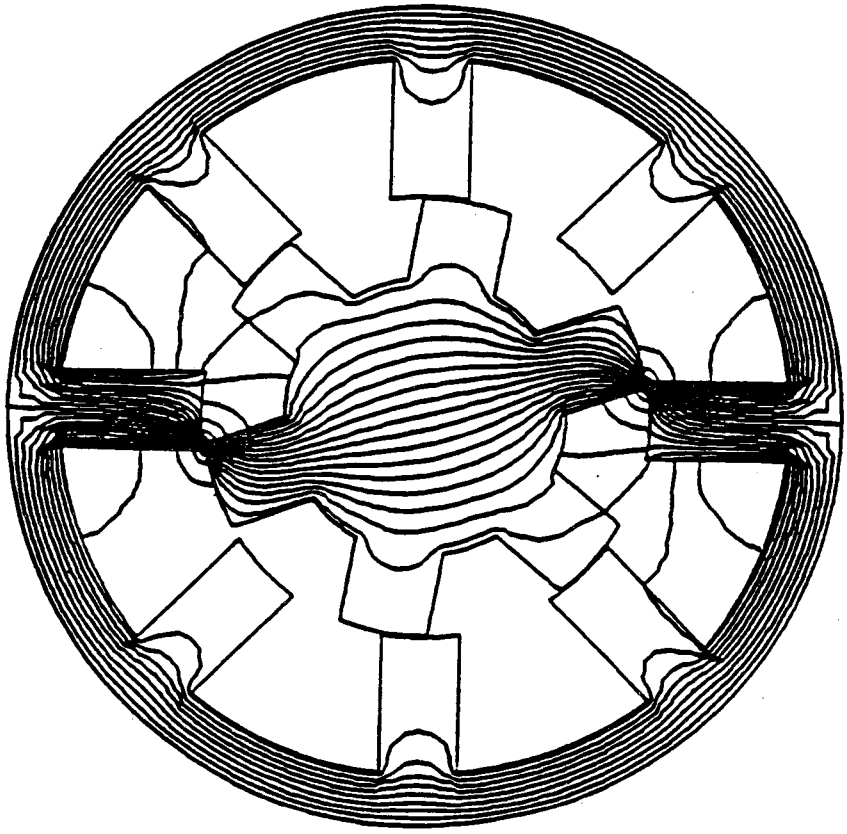

Figure 21 Flux Distribution at 20° Rotor Angle
(From reference [6])

CHAPTER 4
MACHINE PERFORMANCE PREDICTION

The main objective of this project is to develop a simple and efficient method for evaluating preliminary designs, in particular, the steady state performance of a SRM. The steady state machine performance, usually characterized by the torque and current waveforms at various operative speeds, provides useful information about the different designs. An excellent design could result in lower manufacturing costs, better torque profile, higher efficiency and torque-to-mass ratio [2]. These advantages can be accomplished by careful and thorough design studies. Because attempts to maximize certain machine advantages involves compromises with the need to minimize converter costs, inexpensive simulations can help the designer with such decisions.

This chapter covers three crucial aspects of machine simulation: the machine's electrical circuit modelling, flux linkage interpolation technique, and the numerical integration of the machine's voltage equation for the constant speed case. The simulation results obtained are then compared to those based on the finite element method described in [6] to gauge the accuracy and also to help

establish the viability of the proposed analytical magnetic circuit modelling approach used in this project.

4.1 Machine Electrical Circuit Description

Before an effective simulation of the SRM can be accomplished, the circuit describing the electrical system must first be established. Figure 22 shows the circuit representation of the four stator phases with the source. The resistance and inductance of the stator phase windings are represented as lumped circuit components. The inductance (L) is a function of both current and rotor positions. The free-wheeling diode enables energy stored in the stator windings to be returned to other parts of the circuit not shown. When the switch is closed, the voltage equation of the stator phase shown is given simply by:

$$V_{DC}=i\cdot R_{int}+\frac{d\lambda}{dt} \qquad (4.1)$$

where:

V_{DC} -DC source voltage

R_{int} -stator winding resistance (internal resistance)

i -stator current

λ -stator phase winding flux linkage

For the present purpose, we will consider only the single current pulse mode of excitation. The current chopping mode at low speed operation merely involves a more

complicated switching scheme; it will not be considered here. This simulation ignores iron losses, assumes idealized characteristics for the diode and switch, and assumes constant rotor speed. The ignition and extinction angles are chosen to correspond to those used in [6] to facilitate comparison. When the switch S_A in Figure 22 is closed, the current in the stator winding rises rapidly because of the lower inductance and absence of a back-emf. As the rotor rotates, back-emf in the winding opposes the source voltage moderating the rise of the stator current. In this forward conduction mode, the diode is backward-biased and carries no current. The left hand side of Figure 23 [6] from point O to point A shows the rise in the current. For high speed operation, the back-emf is sufficiently large to cause the current to finally level off. At the turn-off angle, a reverse voltage of $-V_{DC}$ is applied and the switch is turned off; the stator winding current is diverted through the diode which is forward biased by the inductive voltage developed across the winding. Without the free-wheeling diode, the inductive voltage can build up to a dangerously large level possibly creating an arc across the switch. The reverse supply voltage ($-V_{DC}$) is obtained from a center-tapped capacitor pair across the diode bridge. The current decay following turn-off is shown on the right-hand side of Figure 23 from point B to point O. The basic switching for a single pulse current operation at sufficiently high speed is [6]:

$$V_{in}=\begin{pmatrix} +V_{dc}\ if\ \theta_{on} \le \theta \le \theta_{off} \\ -V_{dc}\ if\ \theta_{off} < \theta \le \theta_{ext} \\ 0\ if\ \theta > \theta_{ext} \end{pmatrix} \qquad (4.2)$$

where:

V_{in} -voltage applied across stator winding

θ -angular position of rotor

θ_{on} -turn-on angle

θ_{off} -turn-off angle

θ_{ext} -extinction angle of current

θ_{ext} is the angle when the winding current decays to zero. For steady state operation, the simulation over a basic period shown is sufficient as the response over the other periods are the same, assuming periodic symmetry.

Equation (4.1) describes the relationship between applied voltage and flux linkage. Since a change in the electrical current will bring about a change in the flux linkage, and vice versa, their relationship has to be established.

The data in question is an array of flux linkages with respect to current and rotor position found previously from the magnetic circuit modelling. However, the machine voltage relationship of equation (4.1) shows the flux linkage changing with time. Therefore, the relationship of the flux linkage with respect to the machine voltage equation has to

be re-defined in order for the data be used. Using the chain-rule principle, $\frac{d\lambda}{dt}$ can be rewritten as:

$$\frac{d\lambda(i(t),\theta(t))}{dt}=\frac{\partial\lambda}{\partial i}\left(\frac{di}{dt}\right)+\frac{\partial\lambda}{\partial\theta}\left(\frac{d\theta}{dt}\right) \tag{4.3}$$

where:

λ -flux linkage

t -time

i -current in stator windings

θ -angular position of rotor

$\frac{\partial\lambda}{\partial\theta}\left(\frac{d\theta}{dt}\right)$ -back-emf of machine

Expressing the rotor speed as:

$$\frac{d\theta}{dt}=\omega_r \tag{4.4}$$

and the incremental inductance as:

$$L_{inc}=\frac{\partial\lambda}{\partial i} \tag{4.5}$$

the voltage equation of (4.1) can be re-stated as:

$$V=R_{int}\cdot i+\left(L_{inc}\left(\frac{di}{dt}\right)+\left(\frac{\partial\lambda}{\partial\theta}\right)\omega_r\right) \tag{4.6}$$

Figure 24 shows the relationship between incremental inductance and inductance. Inductance is defined as $\frac{AB}{OA}$ which signifies one point in the plot. On the other hand, incremental inductance is defined as $\frac{AD}{OA}$, on the slope of the inductance curve. Since equation (4.5) specifies a change in the inductance with i at a fixed θ, the incremental inductance is used.

As mentioned before, the machine voltage equation is integrated to obtain the phase winding current:

$$\frac{di}{dt} = \frac{V - R_{int} \cdot i - \left(\frac{\partial \lambda}{\partial \theta}\right) \cdot \omega_r}{L_{inc}} \qquad (4.7)$$

The value of L_{inc} and $\frac{\partial \lambda}{\partial \theta}$ for the corresponding i and θ has to be determined from a numerical interpolation of the flux linkage data shown in Figure 20.

4.2 Flux Linkage Interpolation

The flux linkages found from the magnetic circuit model are stored in an array where the row and column coordinates are current and rotor position. This particular method was chosen to conserve memory requirements and to facilitate the

plotting of the flux linkages. Interpolation will be required for in-between values of current and rotor position. The interpolation method chosen for the flux linkages is the same one used to interpolate functions of two variables for the finite element system. Figure 25 shows a sample patch of the flux linkage surface from Figure 20. In order to find the value of this patch, the values of the flux linkages for each of the four corners around the patch are found and used to interpolate the value of the flux linkage for the patch itself. As described in [13], an approximation function can be derived for rectangular elements of any surface plot.

$$\lambda(\theta, i) = a_1 + a_2\theta + a_3 i + a_4\theta i \qquad (4.8)$$

where:

λ -flux linkage

θ -rotor position

i -current in winding

a -constant

The four coefficients, a_1 through a_4, are determined using the nodal values of λ at the corners of the patch. Appendix G details the method for determining these coefficients from equation (4.8). This interpolation method is also being used to determine the co-energy and torque.

4.2.1 Interpolation of L_{inc} and $\frac{\partial \lambda}{\partial \theta}$

Having the analytic expression for λ within a patch, the corresponding values of L_{inc} and $\frac{d\lambda}{d\theta}$ can be determined as follows:

$$L_{inc}=\frac{\partial \lambda}{\partial i}=a_3+a_4\theta \tag{4.9}$$

and

$$\frac{\partial \lambda}{\partial \theta}=a_2+a_4 i \tag{4.10}$$

4.3 Simulation of the SRM by Integration of Machine Voltage Equation

The accuracy of the numerical integration of the machine voltage relationship described in equation (4.7) is important. If the integration is error-prone, the results will not be reliable. For this purpose, a fourth-order Runge-Kutta predictor method was chosen due to the inherent numerical stability [12]. The disadvantage of Runge-Kutta is the programming of four function calculations for each integration step [12]. The formulas for the integration of equation (4.7) are [12]:

$$K^{(1)}=F(X_n, t_n)$$

$$K^{(2)}=F(X_n+\frac{h}{2}K^{(1)}, t_n+\frac{h}{2})$$

$$K^{(3)}=F(X_n+\frac{h}{2}K^{(2)}, t_n+\frac{h}{2}) \qquad (4.11)$$

$$K^{(4)}=F(X_n+hK^{(3)}, t_n+h)$$

$$X_{n+1}=X_n+\frac{h}{6}(K^{(1)}+2K^{(2)}+2K^{(3)}+K^{(4)})$$

where:

K -intermediary variable

F(X,t) -function being integrated

h -step size

X -variable integrated with respect to time; current (i)

The flowchart in Figure 26 details the steps taken to simulate the SRM. The simulation utilizes the desired operating condition of turn-on and turn-off angles, speed, and voltage. Reasonable initial values are essential to set the simulation off to a good start. The simulation utilized the turn-on and turn-off angles, speed, voltage, and the internal resistance. The initial values used in the simulation are detailed in Appendix A. The simulation program interpolates for the value of flux linkage given the present rotor position and current value. With the flux linkage known, L_{inc} and $\frac{\partial\lambda}{\partial\theta}$ can be determined for some θ and

i. This process is repeated within the Runge-Kutta routine until the new current value is found. When the turn-off

angle is reached, the polarity of the source voltage is reversed. The result of the machine simulation is the current for each rotor position over the basic period. Once the current is established, the torque can be determined from the partial of the co-energy with respect to a small change in rotor position.

4.4 Calculation of Co-energy

In addition to finding the current, the torque developed is often of interest. The co-energy is the right-hand part of the magnetic field curve shown in Figure 24 [6] bounded by the points O, A, and B. The left-hand part of the curve, bounded by points O, C, and B, is the stored energy (W) in the winding. This curve is also known as the λi curve [14]. The torque developed per basic period can be expressed as:

$$T_e = \frac{\partial W_c}{\partial \theta} \tag{4.12}$$

where the co-energy (W_c) can be expressed as:

$$W_c = \int \lambda \, di \tag{4.13}$$

The W_c is found with the position of the SRM held constant. Substituting equation (4.8) into (4.13), the co-energy can be

interpolated from Figure 20 as:

$$W_c=\int \lambda \, di=a_1 i+a_2\theta i+\frac{1}{2}a_3 i^2+\frac{1}{2}a_4\theta i^2 \qquad (4.14)$$

Given the values of current and rotor position, the co-energy can be computed from equation (4.14). A plot of the co-energy is shown in Figure 32 of the next chapter.

4.4.1 Calculation of Torque from Co-energy

With the co-energy (W_c) expressible in terms of i and θ, the torque can be found from taking the partial of the interpolation equation of (4.8):

$$T_e=\frac{\partial W_c}{\partial \theta}=a_2+a_4 i \qquad (4.15)$$

Torque values for various values of current and rotor position can be pre-calculated. Interpolation of this data produces the instantaneous torque of the SRM for a particular current and rotor position.

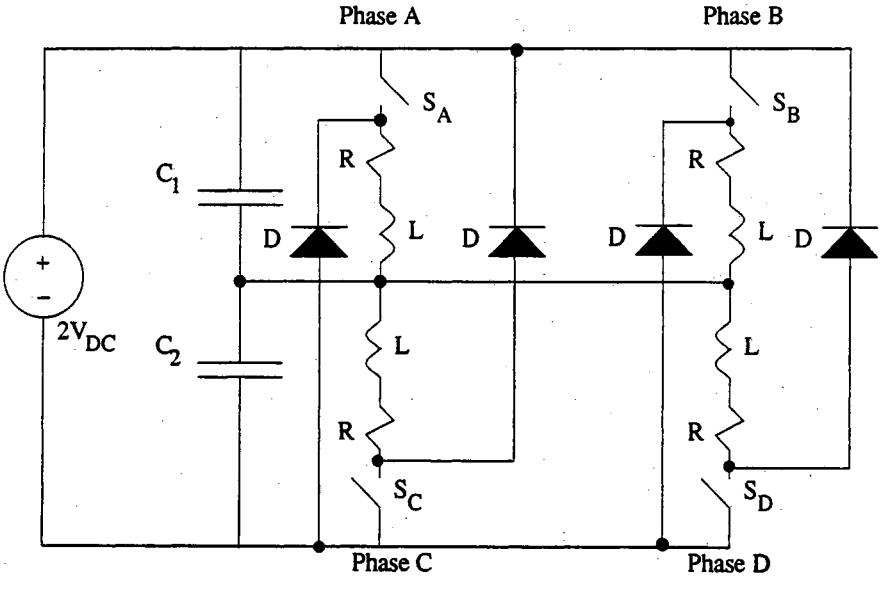

$D=D_{free\text{-}wheeling}$

$R=R_{internal}$

S=switch

Figure 22 Electrical Circuit of a SRM

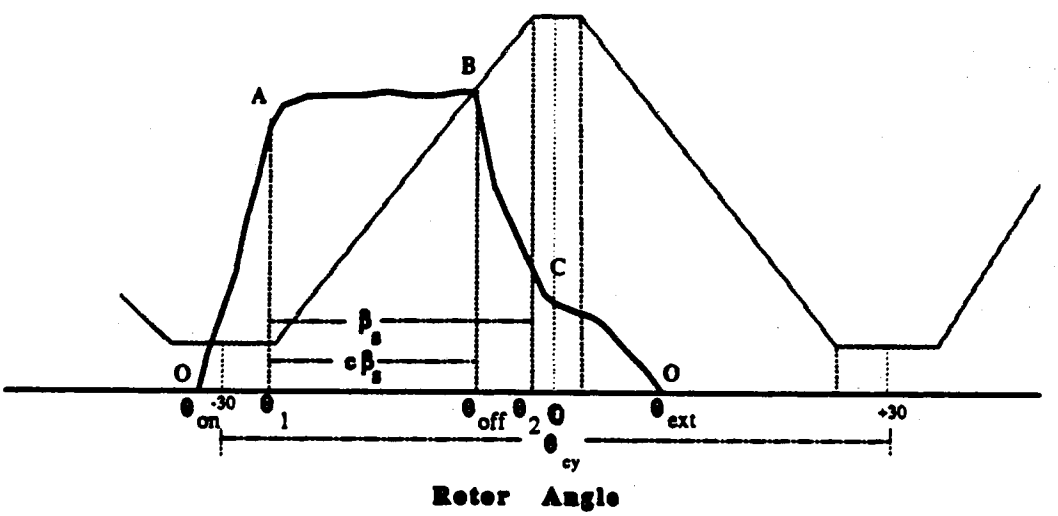

Figure 23 Steady State Current Response
(From reference [6])

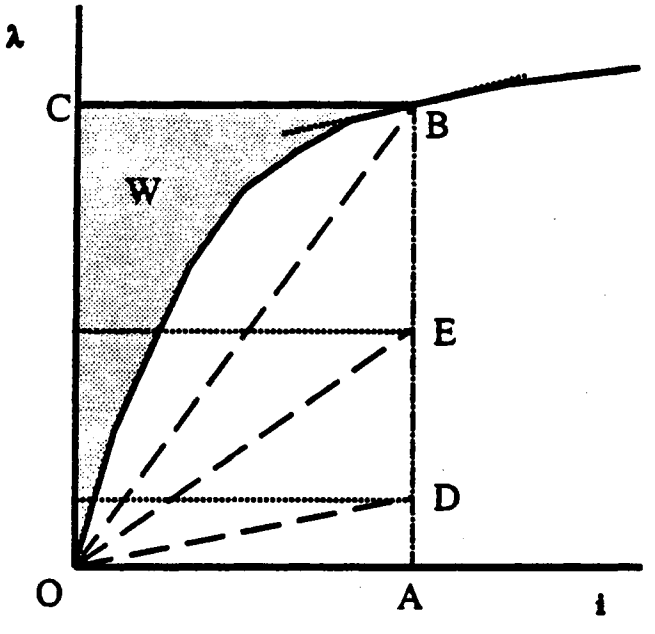

Figure 24 λi Curve
(From reference [6])

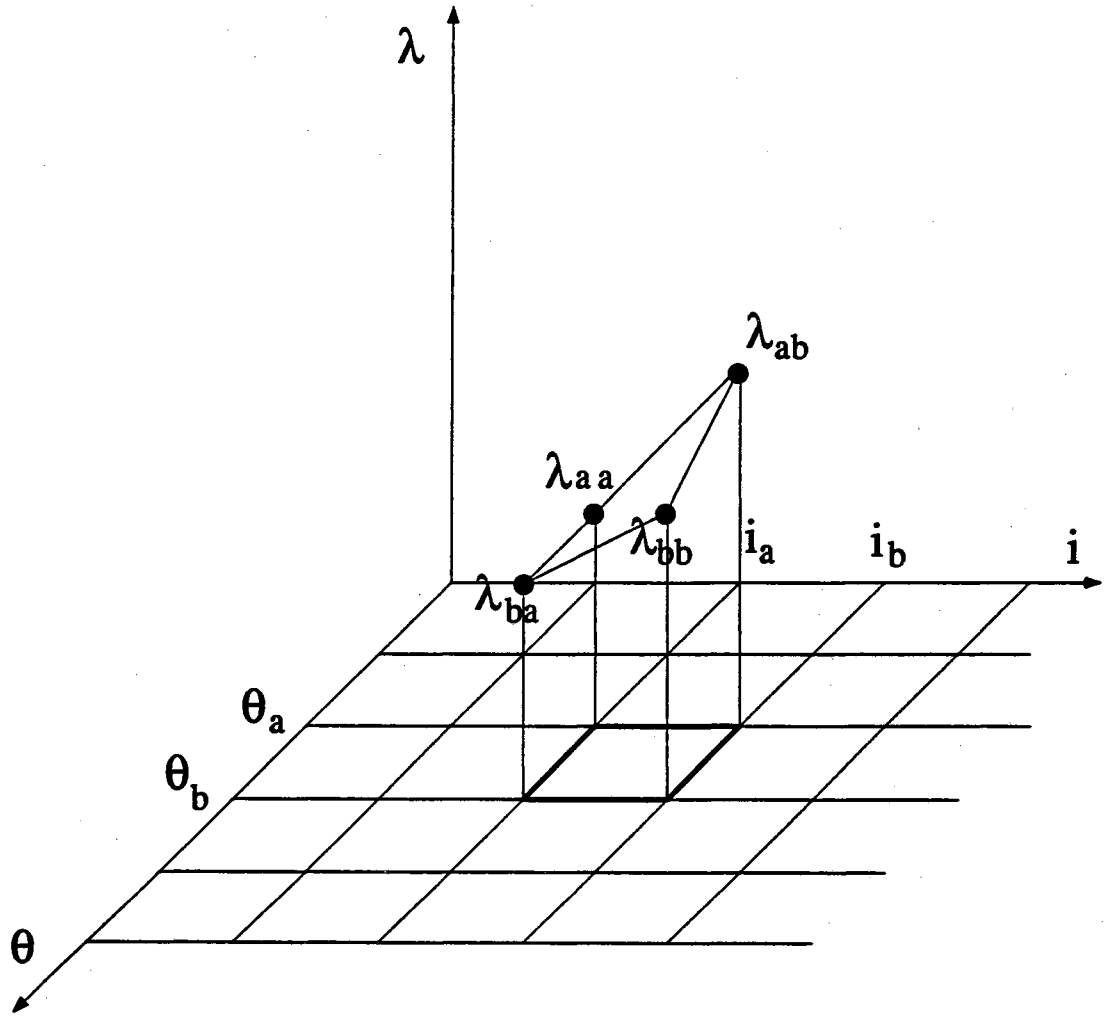

Figure 25 Rectangular Interpolation Patch

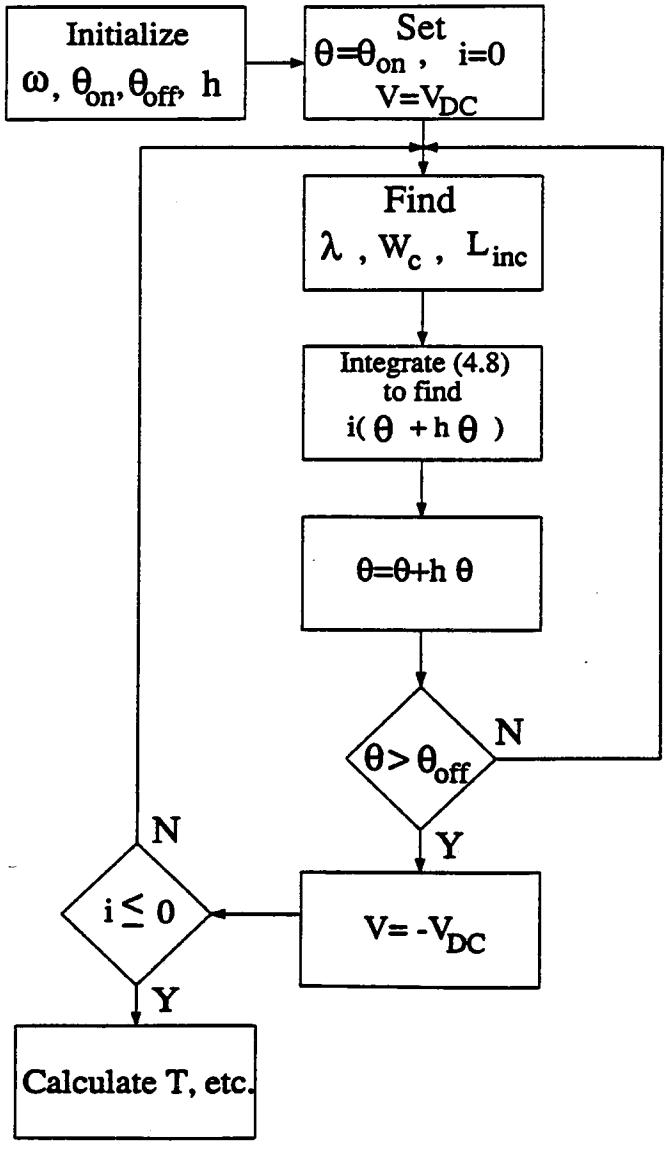

Figure 26 Flowchart of Simulation Program

CHAPTER 5
COMPARISON OF SIMULATION RESULTS WITH THE FINITE ELEMENT RESULTS

To judge the effectiveness of the analytical method, we compare its results with those obtained from a finite element analysis [6] which were verified against experimentally measured values earlier. Comparisons of the incremental inductance, speed voltage, co-energy, torque, current and flux linkages are made, and the differences in results are pointed out. Finally, specific reasons for the discrepancies between methods are given.

5.1 Incremental Inductance Profile

The incremental inductance of [6] is shown in Figure 27. As the iron becomes saturated, the incremental inductance becomes almost constant because there is little or no increase of the magnetic flux in the iron for a small increment of the current.

Figure 28 is the incremental inductance plot from the flux linkages calculated in Figure 20. The peak value of the inductance is very similar to that of Figure 27. However, there is a "kink" in the inductance curve following the separation of the rotor and stator poles. This slight

increase in the inductance is the result of using a different set of flux paths between alignment and non-alignment. There is such an increase in the flux linkage at 21° as shown in Figure 20 that the incremental inductance increases as well. The finite element method provides a much smoother inductance curve. This "kink" or "bump" in the inductance curve of Figure 28, though small in magnitude, produces an undesirable jump in the local gradient.

5.2 Machine Back-Emf Profile

The back-emf or speed voltage is found by multiplying ω_r and $\frac{\partial \lambda}{\partial \theta}$, the latter term derived from the flux linkage profile. The back-emf plays an important role in limiting the winding current along with the inductance. Figure 29 shows the back-emf of the SRM used in [6] on a per-coil basis. As the current increases, the torque developed increases proportionally. However, as the rotor moves under the influence of the developed torque from alignment to non-alignment, the amount of flux linking the winding decreases. This decrease in flux and winding current reduces the back-voltage of the windings as well.

Figure 30 shows the back-emf per phase of the machine as derived from Figure 20 by the analytical method. Figure 30 differs from Figure 29 especially in the non-aligned region. There is a very sudden drop in the back-voltage of the

windings when non-alignment occurs. The drop results from the same problem that affects the flux linkage; that is, the inability of the method to accurately portray the leakage fluxes and the pole tip saturation.

5.3 Co-energy Profile

The co-energy of [6] is shown in Figure 31. As the current increases, the flux linkage and the co-energy rise accordingly. Figures 31 and 32 are plots of the co-energy for the machine detailed in Appendix A from the analytical method and the finite element method, respectively. Both figures, at first glance, are very much alike. Since torque is derived from the spatial derivative of the co-energy, if the gradient of the co-energy profile is comparable then the torque is comparable too.

However, Figure 32 reveals the same drop in values around the 21° region as the flux linkage profile in Figure 20. As discussed in chapter three, the modelling methods used for the saturated pole tips and the leakage fluxes were not adequate. The inability to correctly gauge the pole tip saturation of the parting stator and rotor poles contributes to higher flux linking the stator windings. This and the change to a different set of flux paths for the non-aligned rotor position caused the "kink" in the inductance profile obtained. The same explanation can be attributed to the sudden decline in the co-energy. In addition, the coarse

approximation of the leakage paths in the analytical model resulted in a slightly lower inductance value. Moreover, Figure 32 shows practically no gradient in the co-energy in the non-aligned region compared to Figure 31. The lack of change of the co-energy in the non-aligned region affects the shape of the instantaneous torque.

5.4 Steady State Waveforms

As indicated earlier, of concern is the accurate prediction of the steady state performance. In particular, we would like to predict the steady state current and torque waveforms. The following sections will relate the characteristics of [6] to the simulation results of chapter four. The results presented here are shown using different turn-on angles with single pulse current at 750, 1000, and 1500 revolutions per minute.

5.4.1 Current vs. Rotor Angle

Figure 33a shows the current vs. rotor angle of the machine detailed in Appendix A at 750 rpm from the finite element analysis [6]. The turn-on angle is -23° and the turn-off angle is -13°. Figure 34 shows the current vs. rotor angle for the machine using the analytical method. An obvious difference in the current waveforms is the current surge present in Figure 34 during the start of the simulation. The analytical flux linkage profile of Figure 20

confirms that at angles greater than 21° (the non-alignment of the rotor and the stator for the machine in Appendix A) the flux linkage is lower than that predicted by the finite element method shown in Figure 19. The flatness of the inductance profile in the non-alignmed region resulted in a lower back-emf to counter the applied voltage. As shown in Figure 30, the back-emf at -23° is small. This small back-voltage, coupled with the underestimated inductance, produces a higher surge in current. The current in Figure 34 for a -23° turn-on angle settles before rising again around the 21A mark. This settling is the result of the incremental inductance of the analytical method as shown in Figure 28. The slight "bump" of the λ profile near the parting of the stator and rotor poles causes a slight increase and decrease of the incremental inductance. This "bump" causes the current value to remain slightly constant for some time before rising again. The finite element simulation, however, has no such "bump" in the inductance profile. The underestimation of the inductance becomes even more problematic as the turn-on angle is increased. At 1000 rpm, the machine, as shown in Figure 37, exhibits a sharp current surge before settling. The current surge is nearly double that of the current waveform exhibited in Figure 36a. The current waveform of Figure 37 also has an unusual "dip" at the parting of the stator and rotor poles. Again, this is the result of the "bump" in Figure 28 which tempers the

current surge. However, as the rotor angle continues to increase, the inductance decreases causing the current to rise again. At alignment, the back-voltage of the windings soar providing ample opposing voltage to the applied voltage. However, the back-voltage decreases along with the inductance which enables the current to rise the second time. As the turn-on angle is increased, the inductance increases faster preventing the quick rise in the current present at -26°. Figure 40 shows the SRM current waveform at 1500 rpm for firing angles spaced from -30° to -24°.

5.4.2 Torque vs. Rotor Angle

The steady state torque of the SRM defined in Appendix A provides an insight on the magnitude of the force developed by the machine. A higher torque enables larger loads to be handled. Figure 33b is the torque vs. rotor angle plot taken from [6]. Figure 35 shows the torque vs. rotor angle at 750 rpm from the analytical method. Again, the same problem plaguing the current characteristics of the analytical model appears. The rapid increase in torque is the result of the low inductance of the stator pole winding at angles past non-alignment. Thus, when alignment occurs there is a rapid increase in the inductance. This increase is present in the co-energy plot of Figure 32. As alignment occurs there is such a large increase in the co-energy that torque surges very much like the current due to the large amount of stored

energy in the system. The torque plot of Figure 33b does not, however, exhibit such a rapid increase in torque. However, as the turn-on angle is increased in Figure 35, the torque is much more constrained. At a turn-on angle of -19°, the torque of the SRM at 750 rpm has a much lower peak value. At 1000 rpm, the peak torque in Figure 38 is double that of Figure 36b. In addition, there is a small rise and dip in the torque curve of Figure 35 around the -21° area caused by the same problem that affected the inductance profile in this region. All these irregularities in the current and torque waveforms stresses the importance of having a good inductance profile, especially near the region when the poles are parting.

5.4.3 Flux Linkage vs. Current and Rotor Angle

Figure 42a shows the flux linkage vs. rotor angle at 1500 rpm for a turn-on angle of -30° and a turn-off angle of -17° from the finite element study [6]. As the rotor moves closer to alignment with the stator pole, the flux linkage increases due to the shrinkage in the length of the main flux paths between the rotor and the stator. The peak of the waveform corresponds to the turn-off point. At turn-off, the inductor releases its stored energy through the free-wheeling diode and the current decays over time. Figure 42b shows the instantaneous λ vs. i curve of the machine over a basic switching period. The area enclosed is a measure of the

energy converted to mechanical work. The greater the machine is driven into saturation, the larger the area enclosed per cycle.

Figure 43 shows the analytical simulation of Figure 42a for various turn-on and turn-off angles. For a turn-on angle of -30°, the flux linkage seems rather high compared to that of Figure 42a. This difference in the flux linkages with respect to rotor angle have to do with Figure 20. At -30° the inductance of the windings is very low which enables large currents to flow. As the rotor moves into the aligned portion of Figure 20, the inductance increases. This increase in inductance tempers the rise in current. As the turn-on angle increases (closer to alignment) the time for the current to surge is limited, and the peak current is correspondingly lower.

Figure 42b shows the flux linkage with respect to current from [6]. The flux linkage rises and falls with the excitation current. Therefore, the flux linkage in Figure 42b displays the flux linkage returning to zero. As mentioned earlier, the surge in current that occurs at higher speeds can be attributed to the low inductance values present in the 22° to 30° region of Figure 20. The flux linkages are shown in Figure 44 for the analytical simulation. Again, as the turn-on angle is increased or delayed, the inductance increases at a faster rate curtailing the rapid rise in current. Thus, for a firing angle of -26°, the flux linkage

with respect to current is lower. Figure 47 shows the flux linkage vs. current at 750 rpm at a turn-on angle of -23° and a turn-off angle of -13°. The flux linkage rises to a higher level because of the lower speed. At 750 rpm, the back-voltage of the windings is lower. In addition, the low inductance in the non-aligned region allows the current to rise faster.

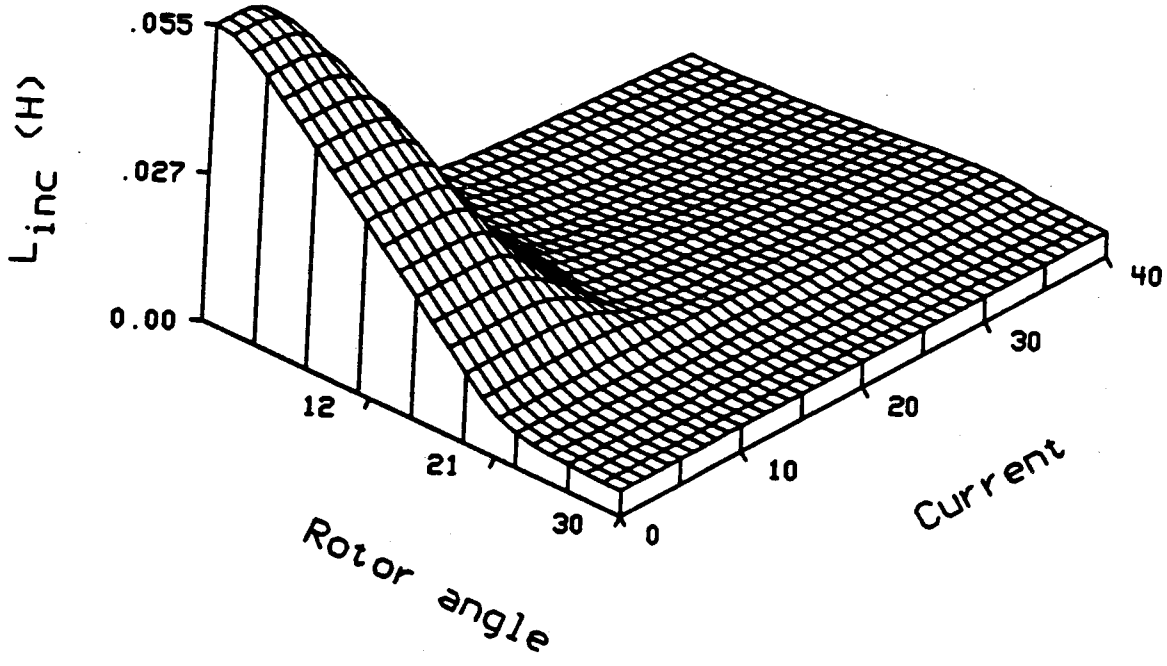

Figure 27 Finite Element Incremental Inductance
(From reference [6])

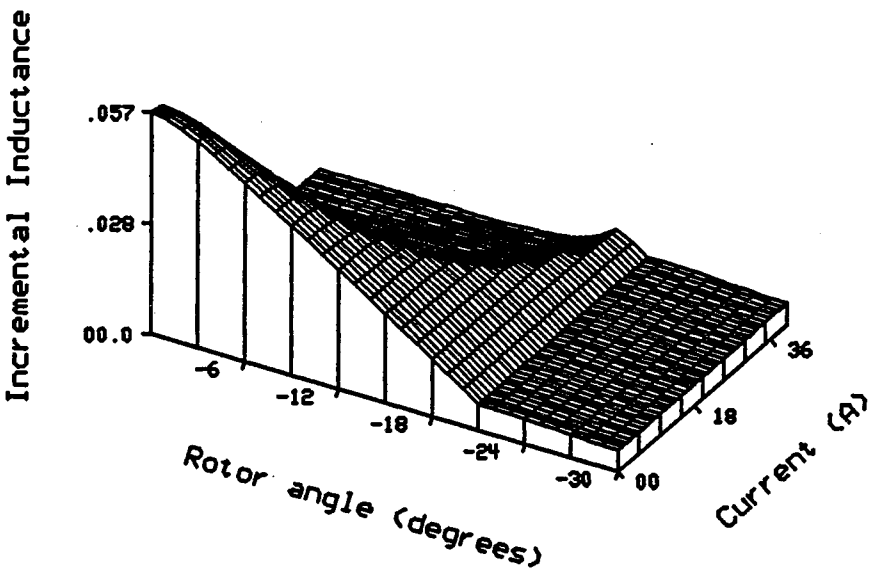

Figure 28 Incremental Inductance from Analytical Method

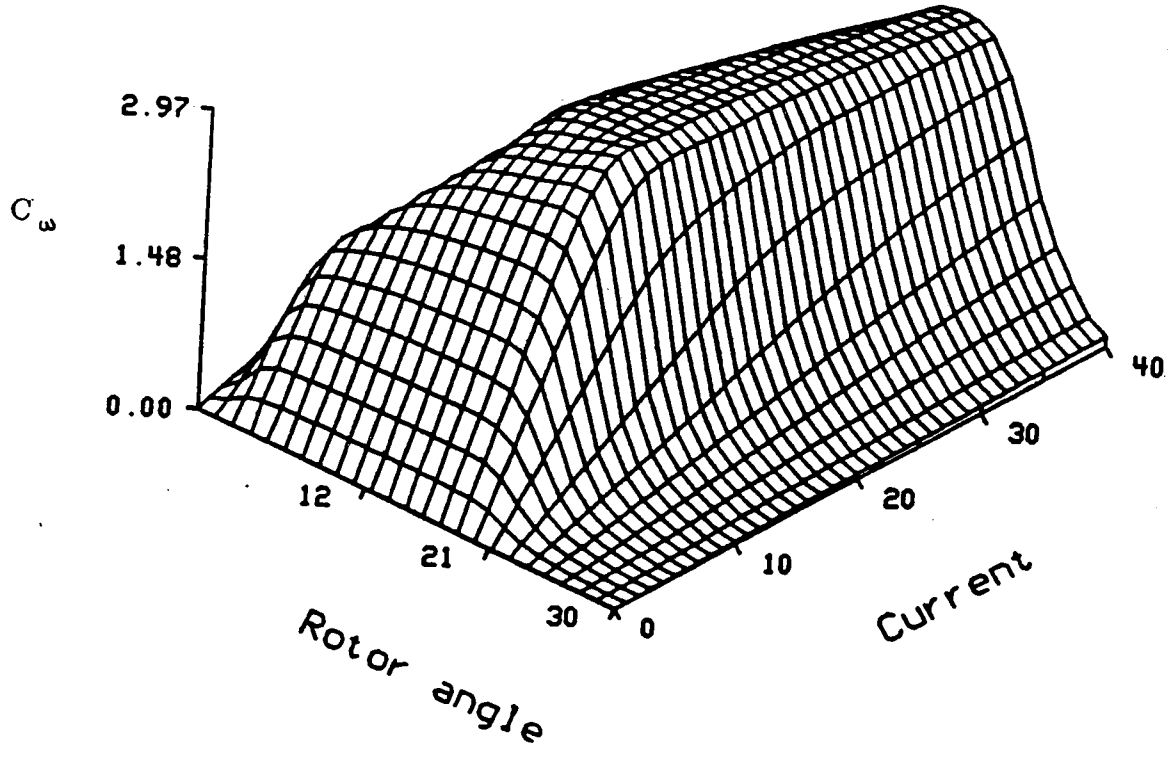

Figure 29 $\frac{\partial \lambda}{\partial \theta}$ from Finite Element Method
(From reference [6])

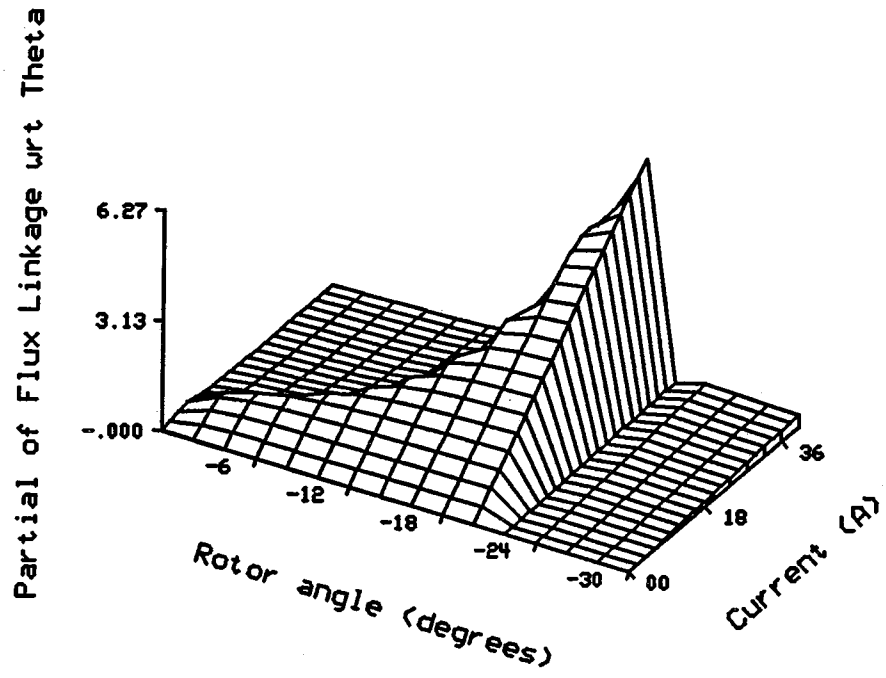

Figure 30 $\frac{\partial \lambda}{\partial \theta}$ from Analytical Method

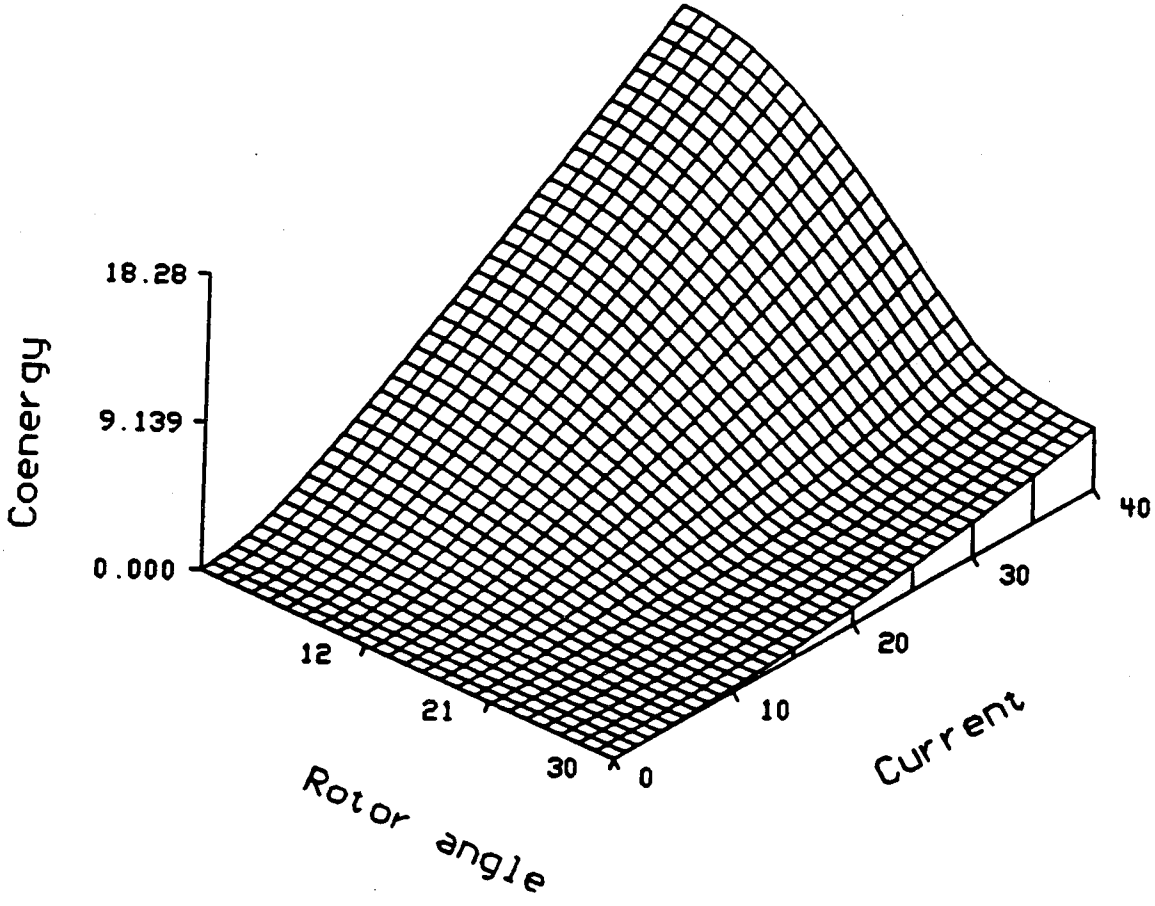

Figure 31 Finite Element Co-energy Plot
(From reference [6])

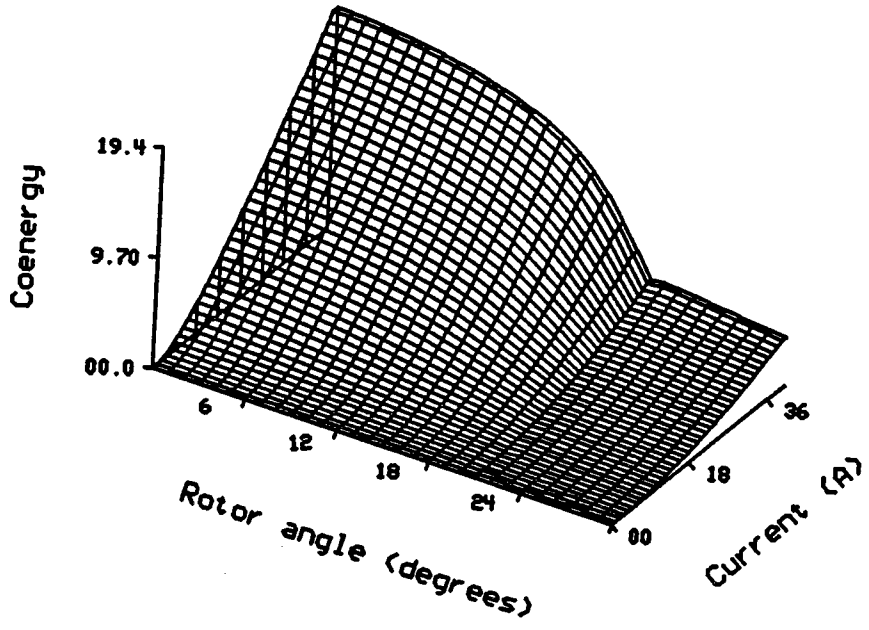

Figure 32 Co-energy from Analytical Modelling

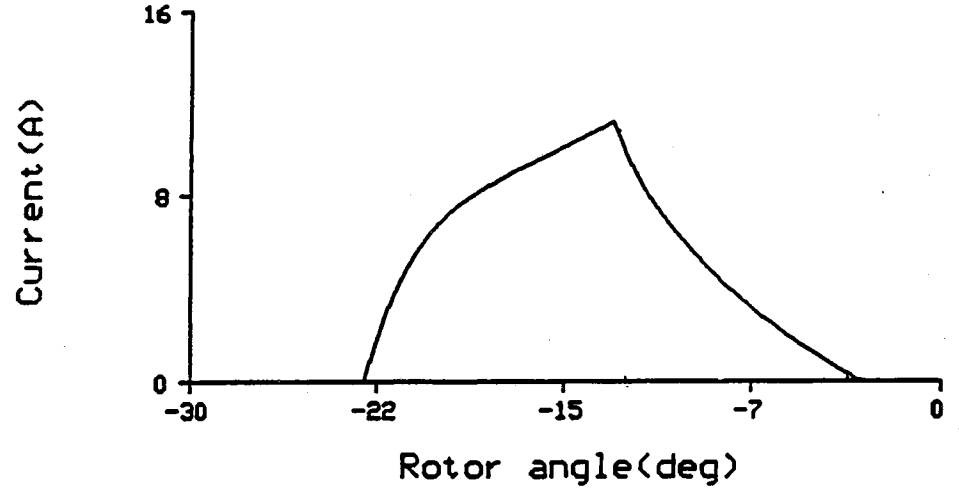

(a)

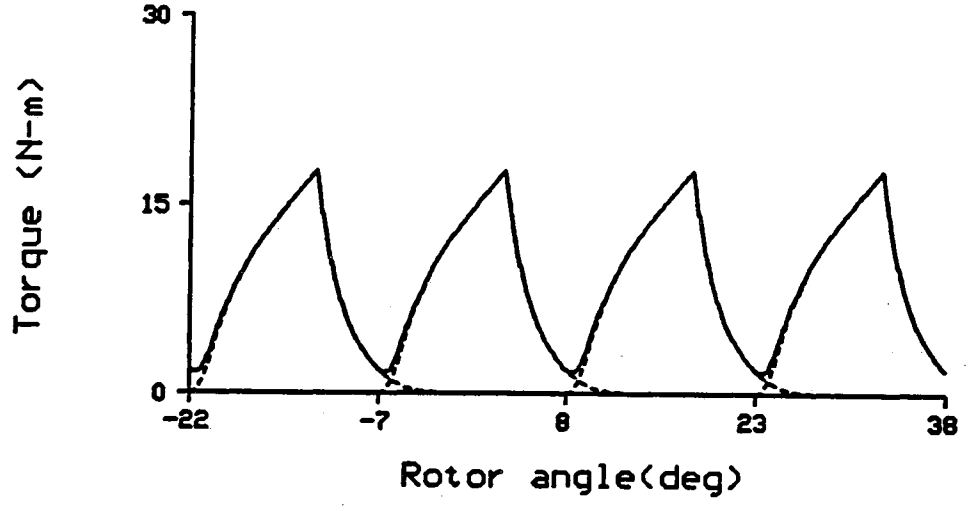

(b)

Figure 33 SRM Steady State Characteristics at 750 rpm
a) i vs. θ and b) T_e vs. θ
(From reference [6])

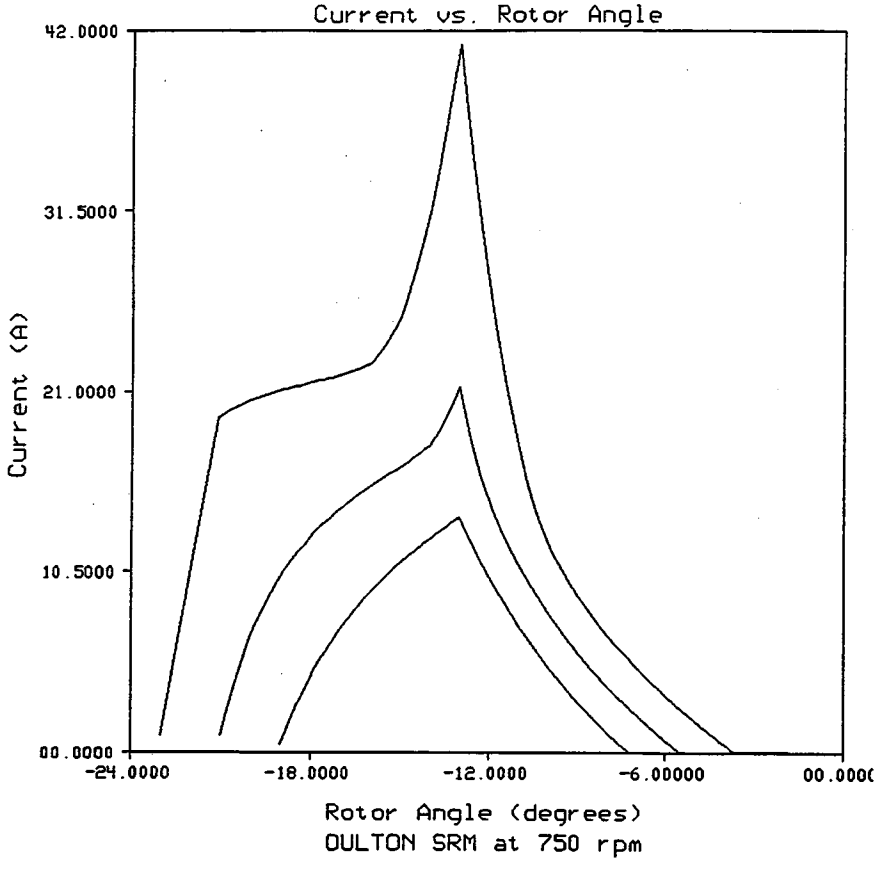

Figure 34 i vs. θ at 750 rpm

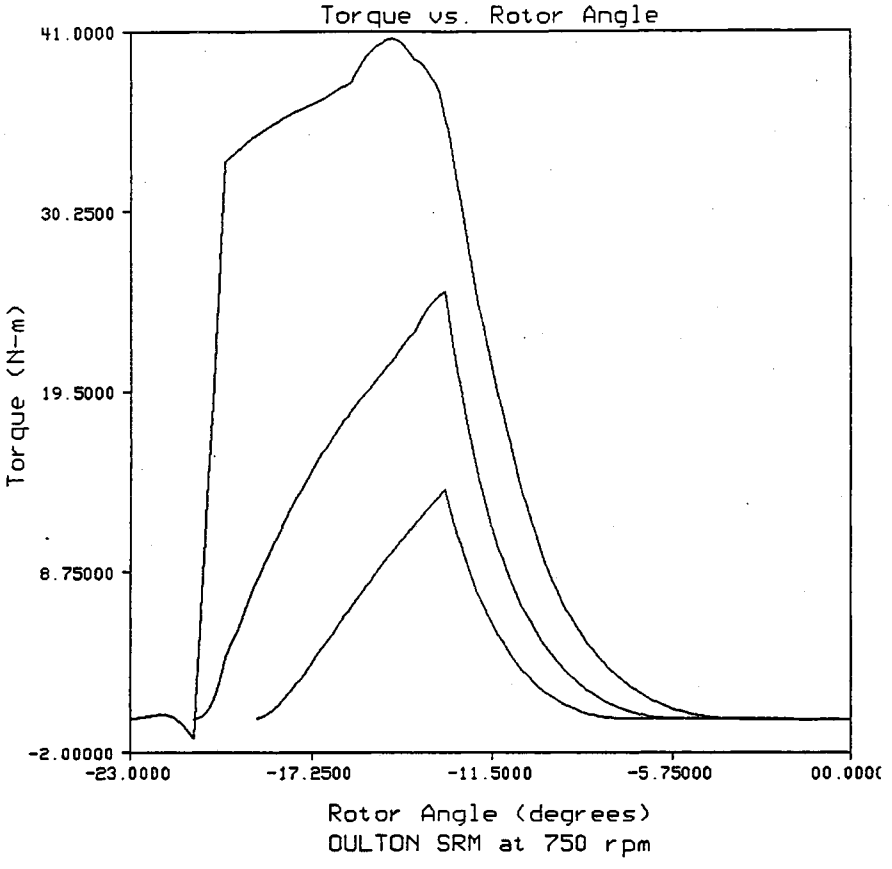

Figure 35 T_e vs. θ at 750 rpm

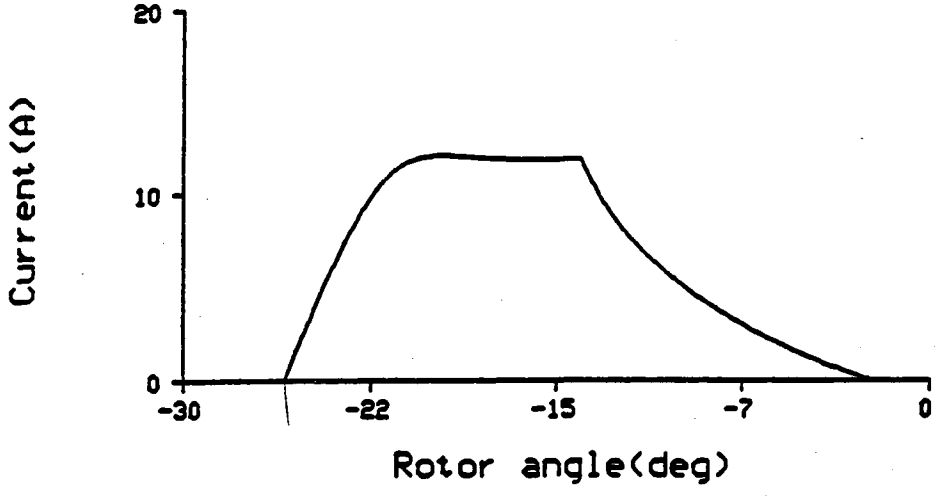

(a)

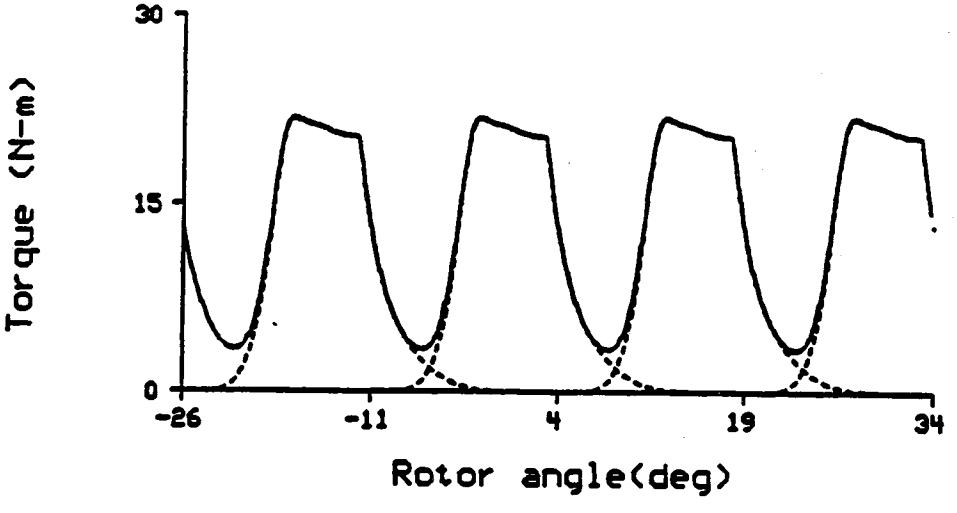

(b)

Figure 36 SRM Steady State Characteristics at 1000 rpm
a) i vs. θ and b) T_e vs. θ
(From reference [6])

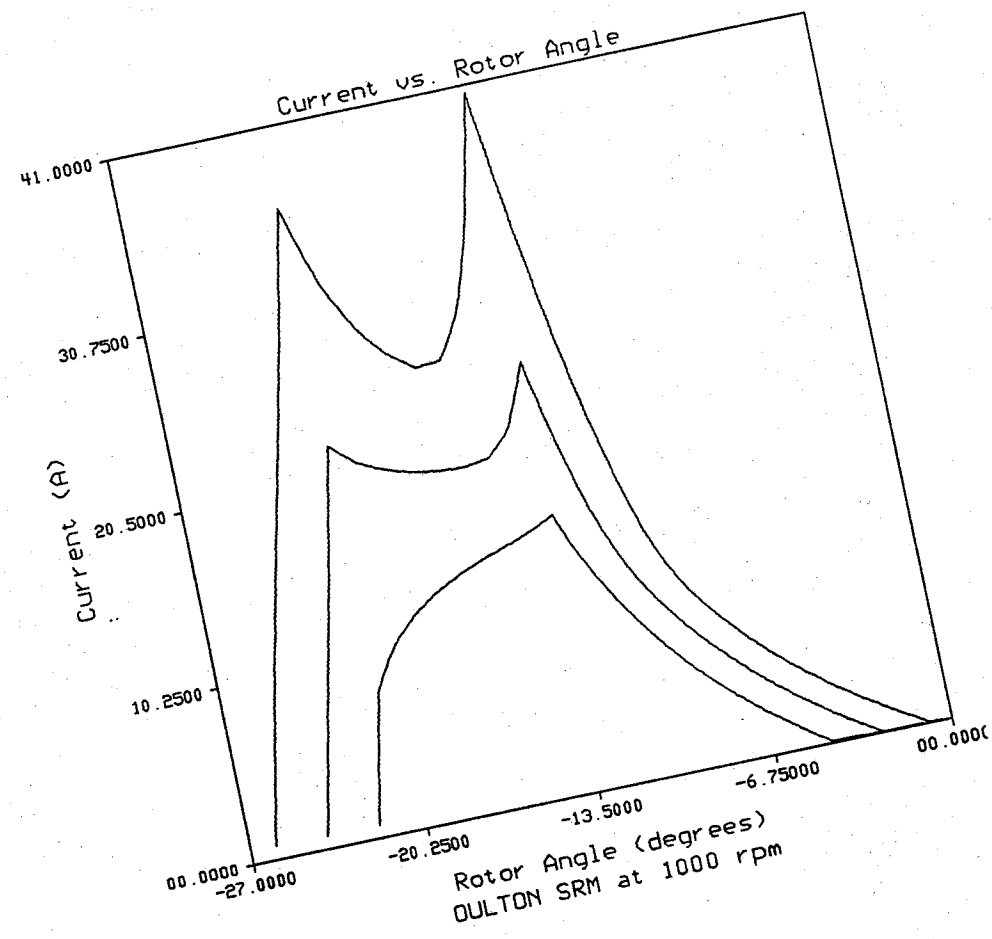

Figure 37 i vs. θ at 1000 rpm

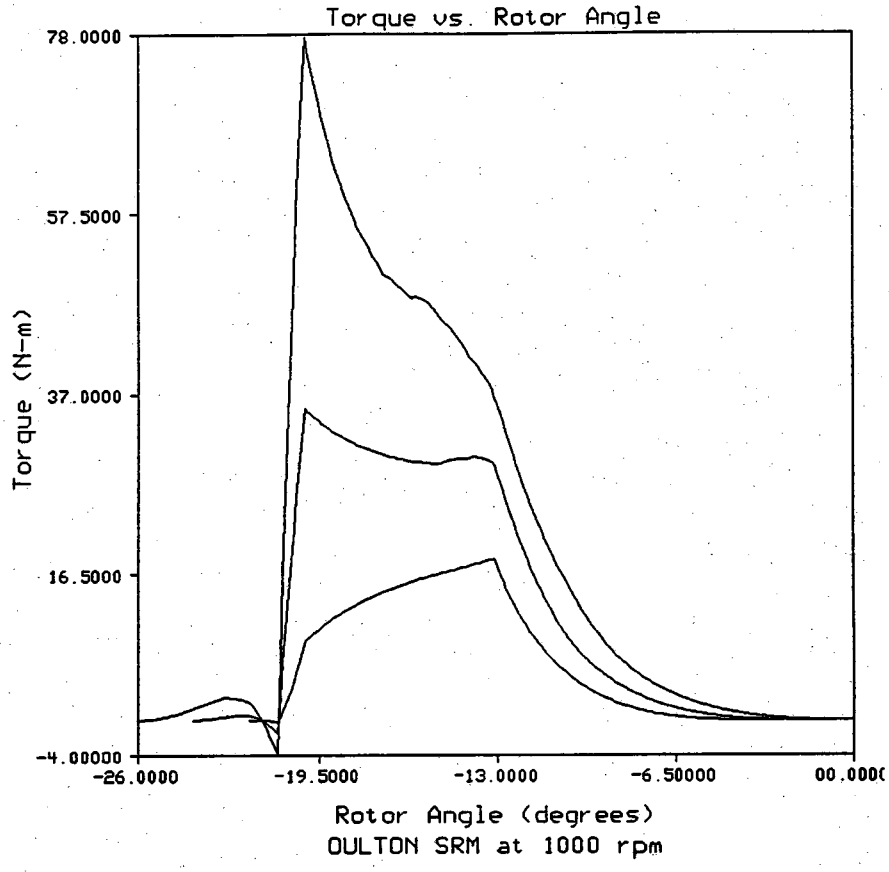

Figure 38 T_e vs. θ at 1000 rpm

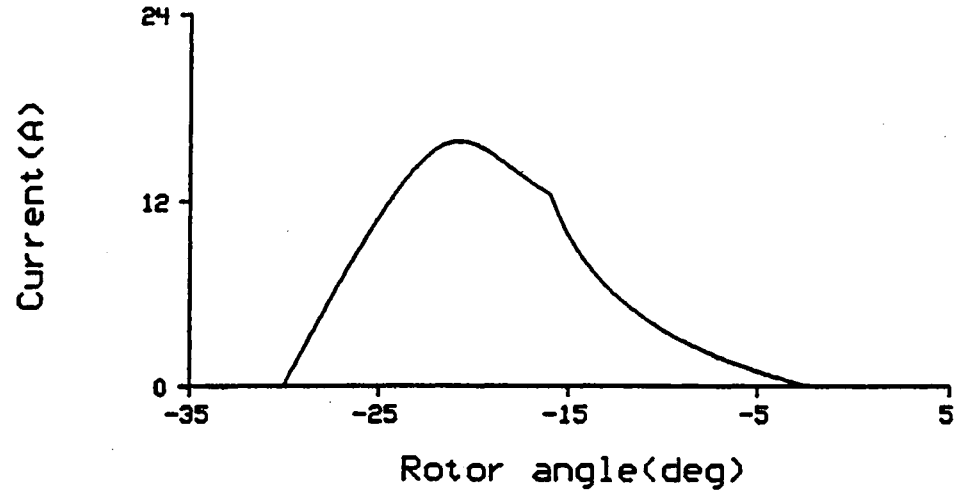

(a)

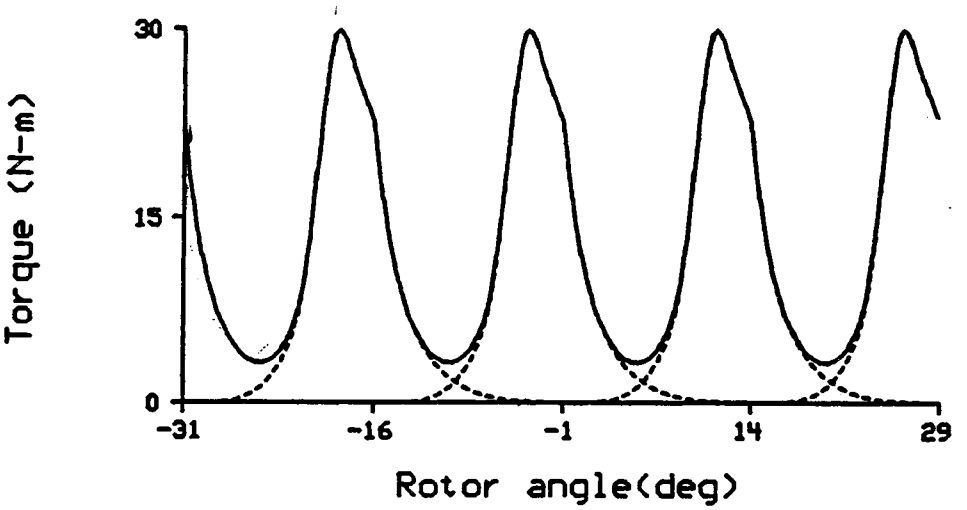

(b)

Figure 39 SRM Steady State Characteristics at 1500 rpm
a) i vs. θ and b) T_e vs. θ
(From reference [6])

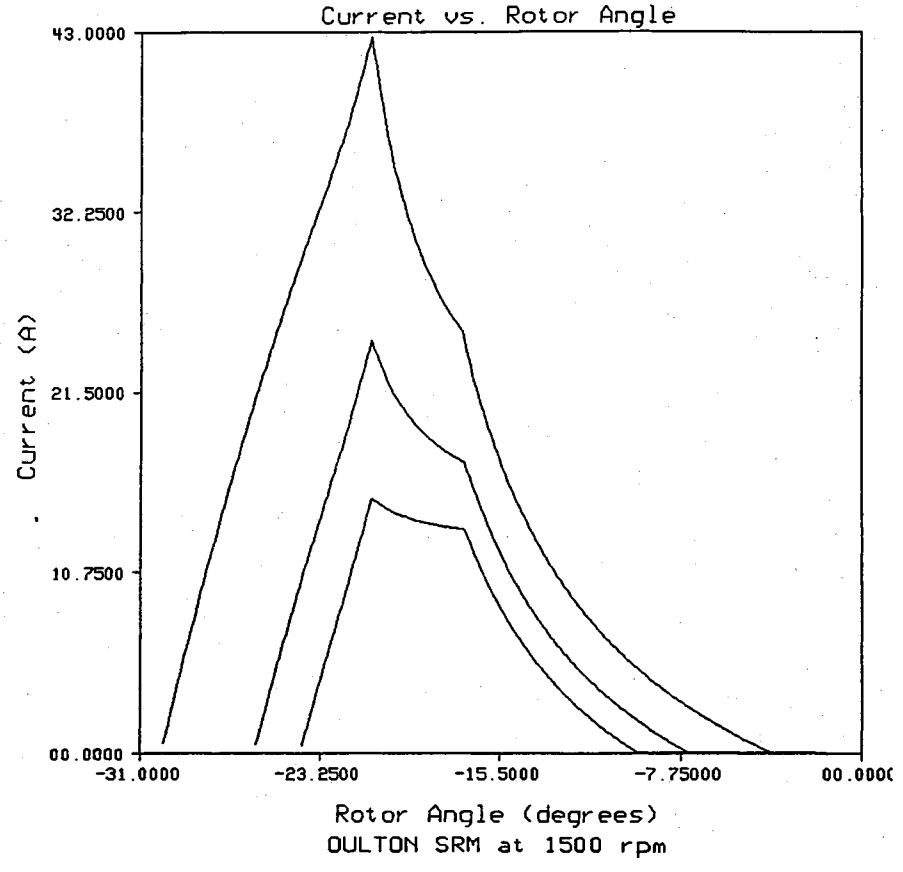

Figure 40 i vs. θ at 1500 rpm

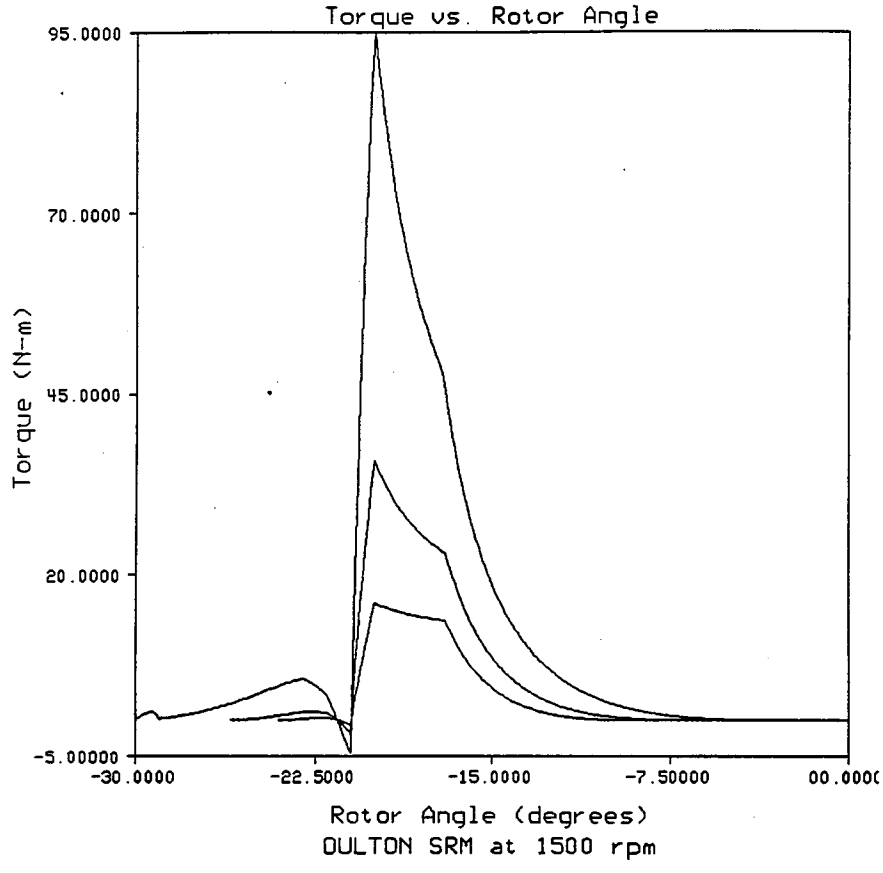

Figure 41 T_e vs. θ at 1500 rpm

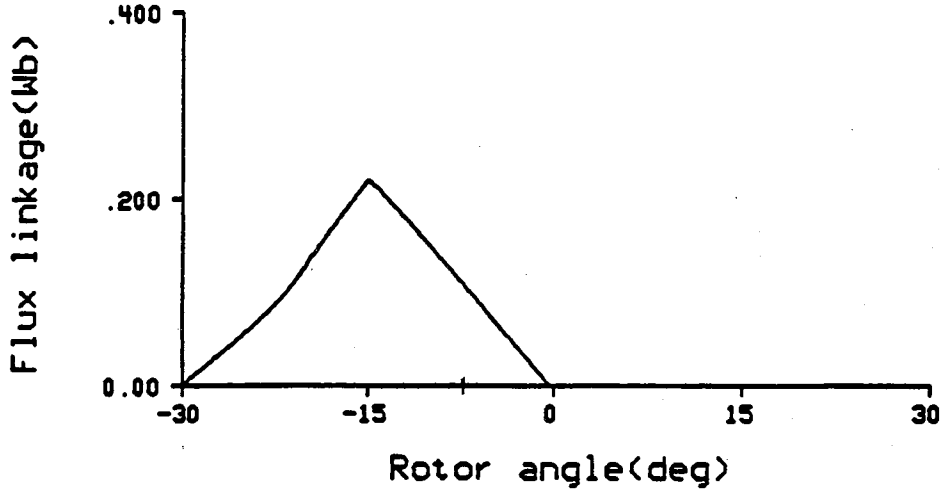

(a)

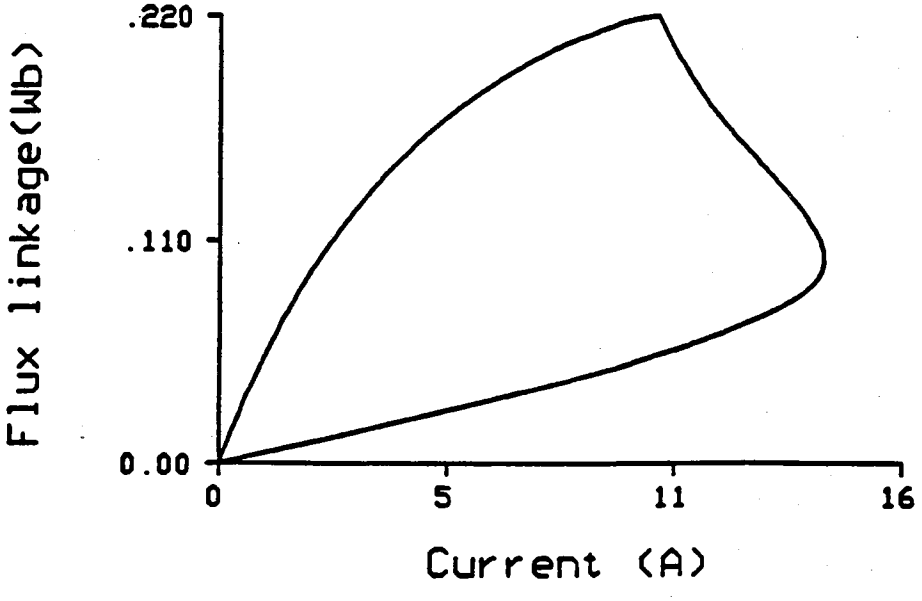

(b)

Figure 42 SRM Flux Linkage Characteristics at 1500 rpm
a) λ vs. θ and b) λ vs. i
(From reference [6])

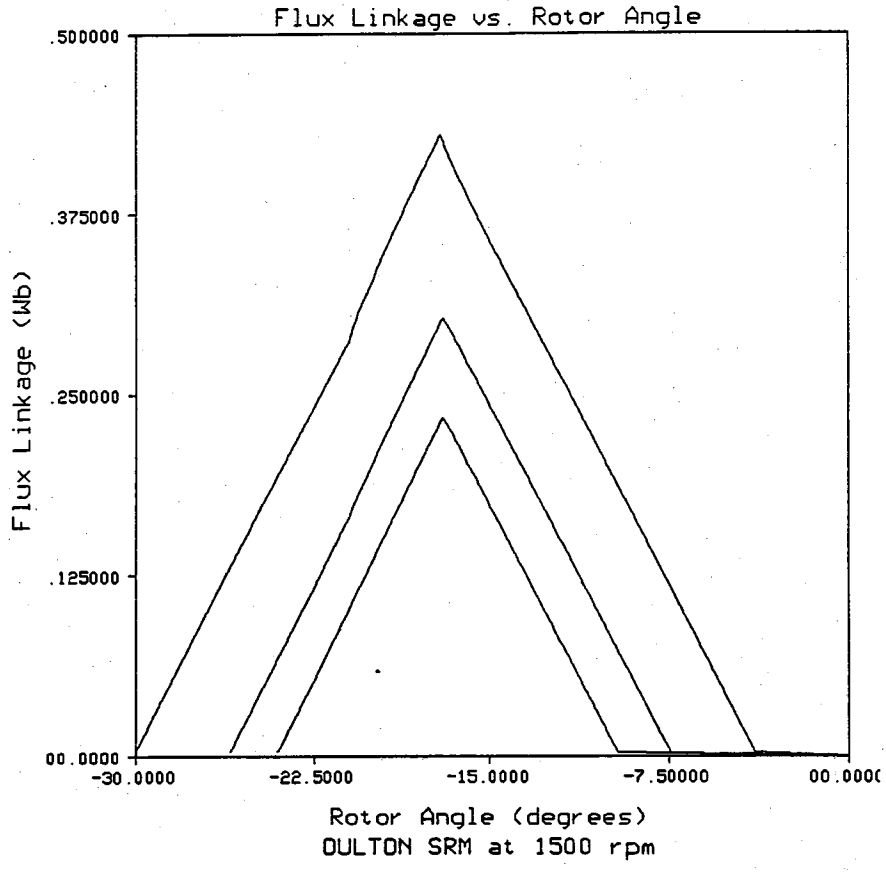

Figure 43 λ vs. θ at 1500 rpm

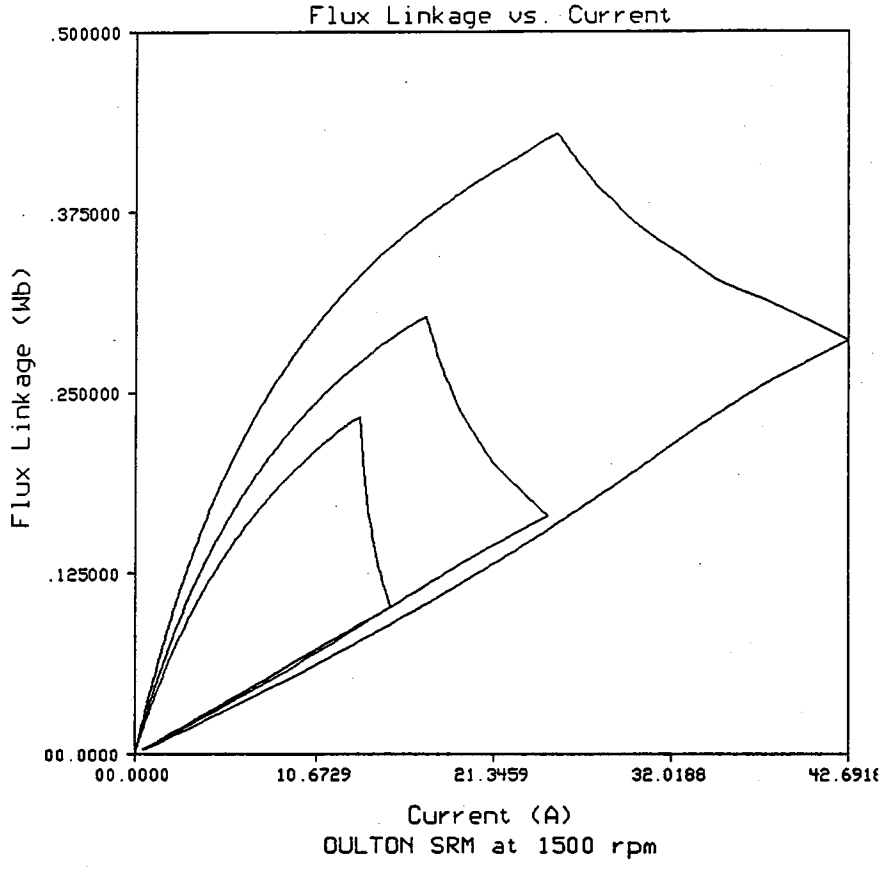

Figure 44 λ vs. i at 1500 rpm

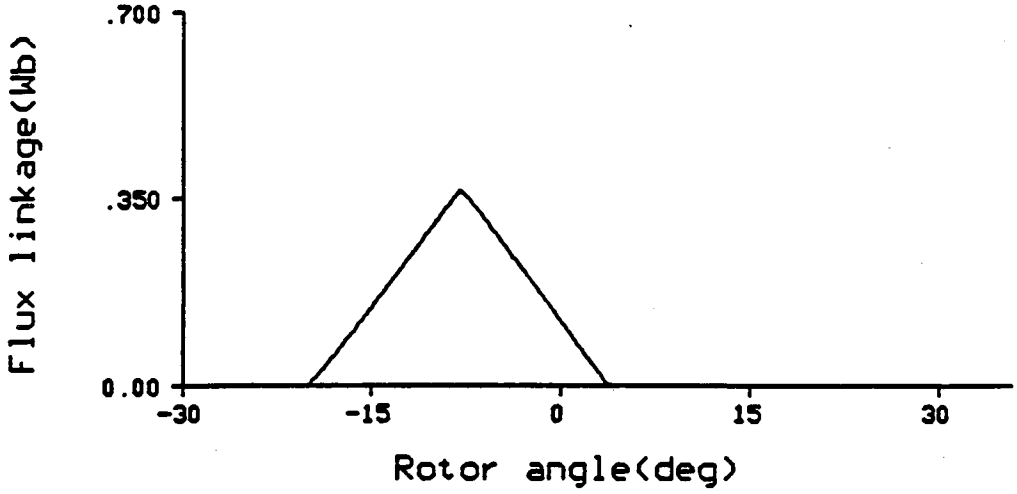

(a)

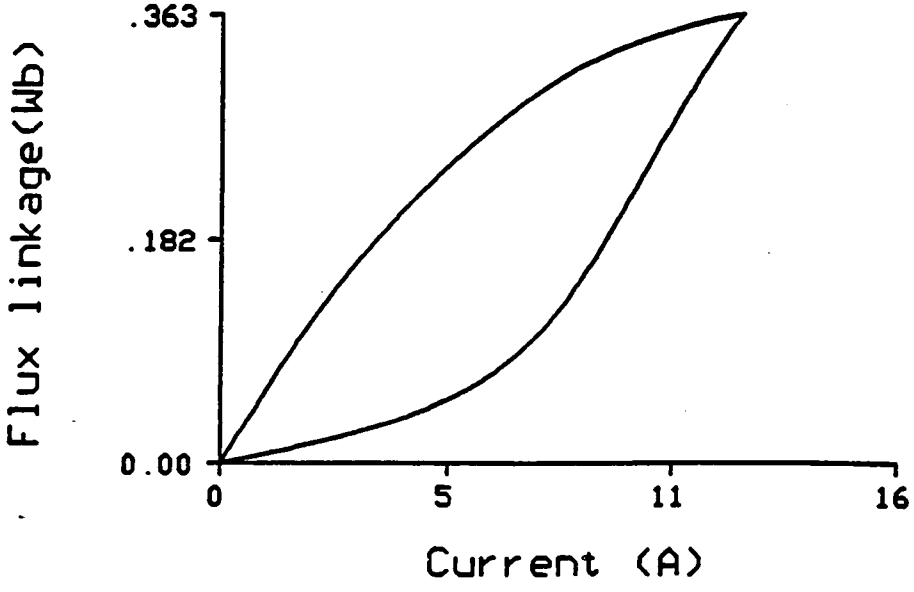

(b)

Figure 45 SRM Flux Linkage Characteristics at 750 rpm
a) λ vs. θ and b) λ vs. i
(From reference [6])

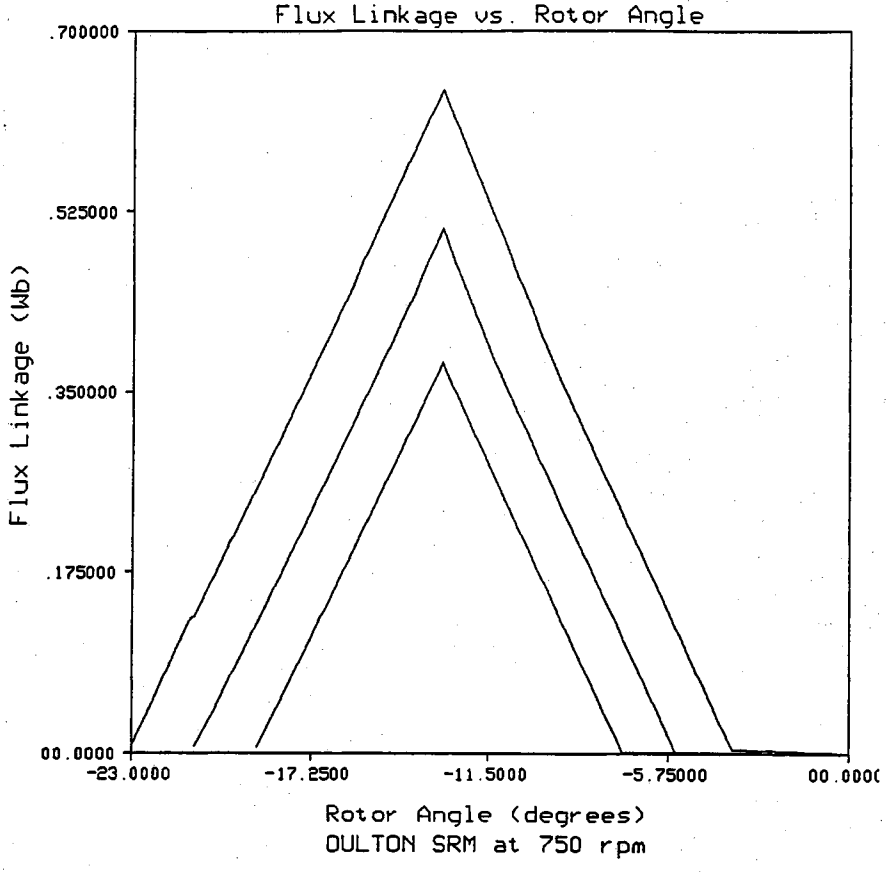

Figure 46 λ vs. θ at 750 rpm

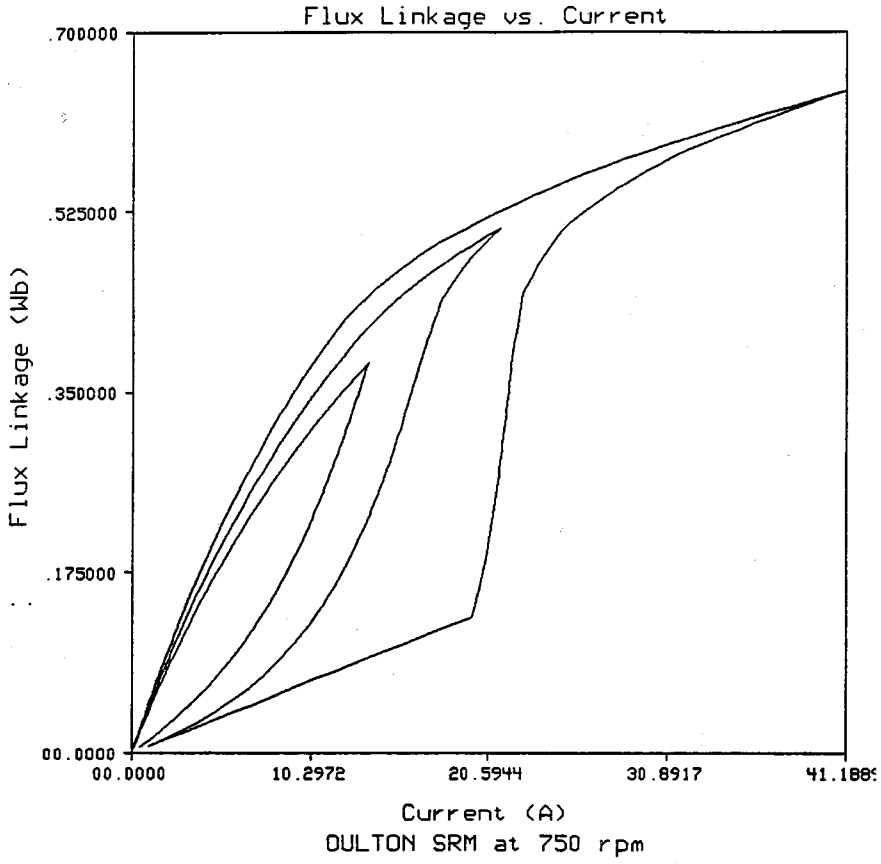

Figure 47 λ vs. i at 750 rpm

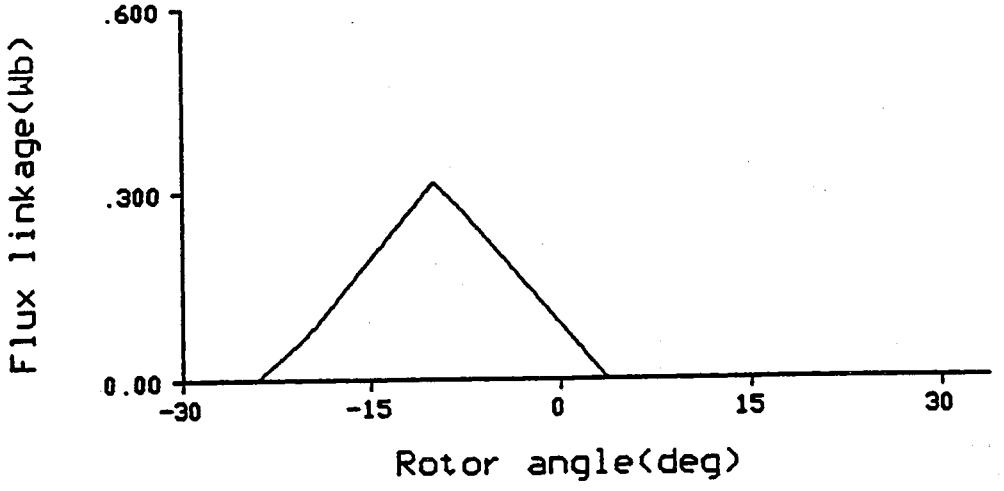

(a)

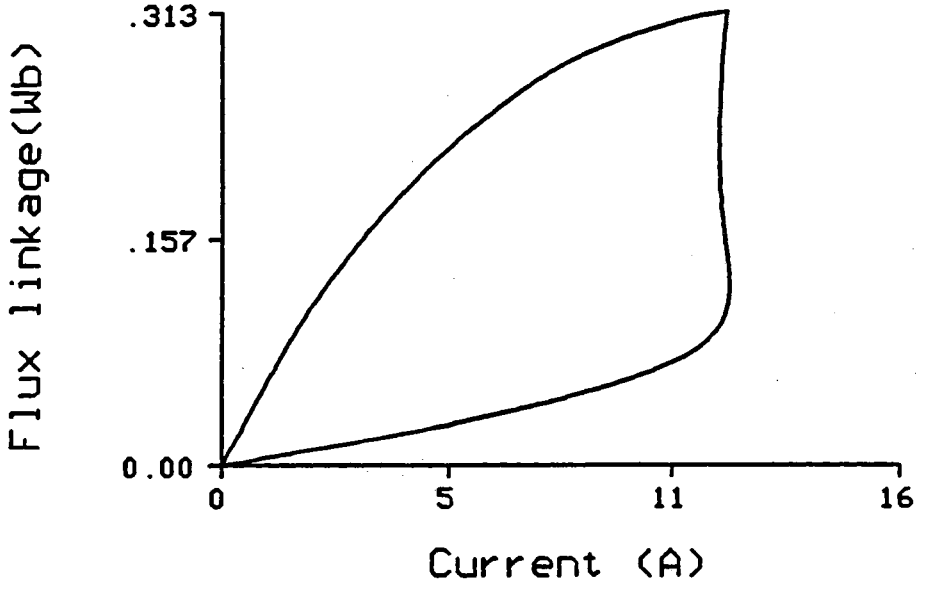

(b)

Figure 48 SRM Flux Linkage Characteristics at 1000 rpm
a) λ vs. θ and b) λ vs. i
(From reference [6])

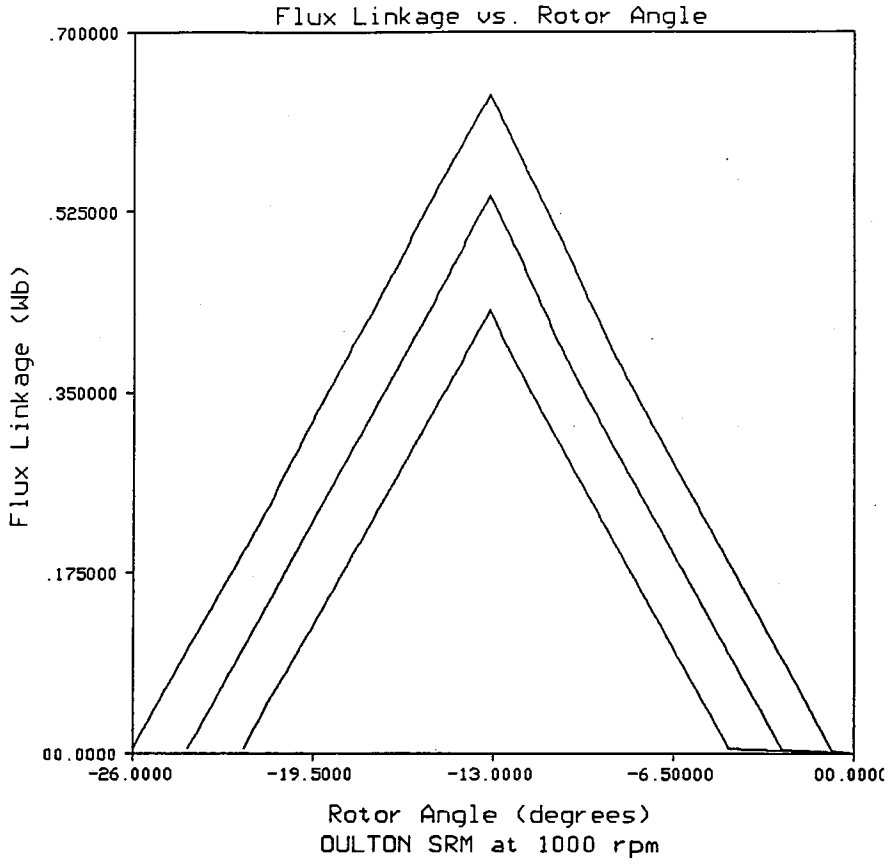

Figure 49 λ vs. θ at 1000 rpm

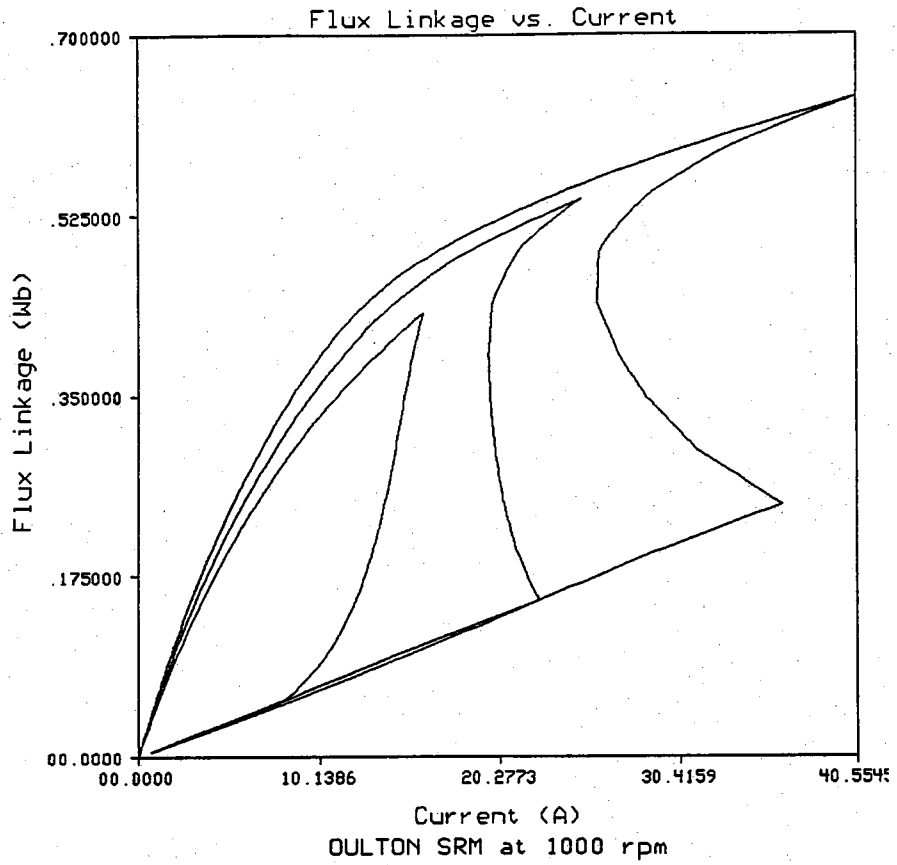

Figure 50 λ vs. i at 1000 rpm

CHAPTER 6
SUMMARY

The objective of this research was to develop an analytical method of predicting the torque, current and flux linkages of an SRM for design purposes. For this, we have investigated the magnetic circuit modelling approach, in which saturation of the iron was included.

The magnetic circuit describing the SRM was perfected and the corresponding equations were formulated. Calculation of the iron reluctances were performed taking into consideration the saturation of the iron. The B-H table was interpolated by the cubic spline method to investigate iron saturation for different values of circuital flux. Methods of finding flux paths through the air gap regions of the SRM were explored. The Roter's method of permeance calculations was chosen for its simplicity of use. An inductance profile of the air gap reluctances was plotted and compared to corresponding finite element results. In addition, leakage paths were incorporated to accurately model the SRM performance.

The resultant non-linear equations of the fluxes were solved using the Newton-Raphson method. The stator flux linkage was found from the flux and was plotted with respect

to the rotor position and current. Comparisons between the flux linkages found from the analytical method and the finite element method were made. The analytical method was found to have some inherent problems related to the approximation of the flux paths.

In order to find the steady state torque and current waveforms, a simulation of the SRM had to be performed. The voltage equation of the phase winding was manipulated into a form from which a numerical integration yields the stator current. Since the flux linkage is a non-linear function of current and rotor position, an interpolation technique was needed to determine the flux linkage from pre-computed data of the machine. Once the instantaneous stator current was found, the co-energy and the instantaneous torque could be determined.

Comparisons between the simulated waveforms of the current and torque using the computed data from the analytical magnetic circuit method and the finite element method were made. Results seem to indicate that the analytical method lacks the accuracy of the finite element analysis because of the inadequacy in modelling the pole tip saturation and the leakage flux paths.

6.1 Areas To Be Further Explored

Based on the findings of this research, the areas that need to be further explored are:

i) Disrepancies in the flux linkage profile can be traced to the present inability to properly model the local saturation regions at the tips of the parting rotor and stator poles. Methods to incorporate this type of saturation must easily integrate into the present framework of the flux path determination scheme used.

ii) Figure 21 exemplifies the underestimation of the inductance in the region past 21°; 21° marks the beginning of non-alignment between the rotor and the stator. The underestimated inductance is the cause of the current surge problematic throughout the simulation phase. The reason for the underestimated inductance lies with the implementation of Roter's method to determine the air gap flux paths. When the rotor is moving further away from the stator pole, fluxes in the leakage paths become more prevalent. As discussed in chapter two, leakage paths were included but were not able to effect an increase in the inductance. The finite element method has the ability to account for all leakage paths and integrate into the overall reluctance of the system. A more refined analytical method of determining the leakages needs to be implemented if the inductance of the non-aligned

machine region is to be increased.

iii) The little "bumps" or "kinks" in the simulated waveforms of the current and torque indicate the importance of having a smooth inductance profile. They could be avoided if the chosen flux paths have a smooth transition from finite overlap to no overlap as the stator and rotor poles part.

LIST OF REFERENCES

LIST OF REFERENCES

[1] Kenjo, Takashi. Stepping Motors and Their Microprocessor Controls. New York: Oxford University Press, 1984.

[2] Kuo, B.C. "Step Motors as Control Devices." 1972/1973 Symposium on Incremental Motion Control Systems and Devices; St. Paul, MN: West Publishing Co., 1974.

[3] Fitzgerald, A.E., Kingsley, Charles, and Umans, Stephen D. Electric Machinery, 5th Ed. New York: McGraw-Hill Publishing Co., pp. 446-484, 1990.

[4] Moreira, Julio and Lipo, Thomas A. "Simulation of a Four-Phase Switched Reluctance Motor Including the Effects of Mutual Coupling." Electric Machines and Power Systems, v.16, pp. 281-299, 1989.

[5] Kuo, B.C. and Coon, W.R. "Computer-Aided Design (CAD) of Step Motors." Power Conversion and Intelligent Motion, v.13, n.6, pp. 74-79, June 1987.

[6] Moallem, Mehdi and Ong, C.M. "Performance Characteristics of a Switched Reluctance Motor Drive." TR-EE 89-52, School of Electrical Engineering, Purdue University, W. Lafayette, IN, August 1989.

[7] Materu, P. and Krishnan, R. "Analytical Prediction of SRM Inductance Profile and Steady-State Average Torque." 1990 IEEE-IAS Conference; 25th annual meeting, Westin Hotel, Seattle, pp. 214-223, October 7-12, 1990.

[8] Rotors, Herbert C. Electromagnetic Devices. New York: Wiley and Sons, 1941.

[9] Canale, Raymond P. and Chapra, Steven C. Numerical Methods for Engineers with Personal Computer Applications. New York: McGraw-Hill Book Co., 1985.

[10] Boylestad, Robert L. Introductory Circuit Analysis. Columbus, OH: Merrill Publishing Company, 1990.

[11] Moallem, Mehdi and Ong, C.M. "Some Design Calculations for a 60kW, 6000rpm, 4/6 SRM." TR-EE 90-13, School of Electrical Engineering, Purdue University, W. Lafayette, IN, February 1990.

[12] Heydt, G.T. Computer Analysis Methods for Power Systems. New York: Macmillan Publishing Co., 1986.

[13] Reddy, J.N. An Introduction to the Finite Element Method. New York: McGraw-Hill Book Co., 1984.

[14] Krause, Paul C. and Wasynczuk, Oleg. Electro-mechanical Motion Devices. New York: McGraw-Hill Book Co., 1989.

[15] Krause, Paul C. Analysis of Electric Machinery. New York: McGraw-Hill Book Co., 1986.

[16] Chai, H.D. "Magnetic Circuit and Formulation of Static Torque for Single-Stack Permanent Magnet and Variable Reluctance Step Motors." 1972/1973 Symposium on Incremental Motion Control Systems and Devices; St. Paul, MN: West Publishing Co., 1974.

[17] Chai, H.D. "Permeance Model and Reluctance Force Between Toothed Structures." 1972/1973 Symposium on Incremental Motion Control Systems and Devices; St. Paul, MN: West Publishing Co., 1974.

[18] Corda, J. and Stephenson, J.M. "Analytical Estimation of the Minimum and Maximum Inductances of a Double-Salient Motor." Proceedings of Int. Conference on Stepping Motors and Systems, University of Leeds, pp. 50-59, September 1979.

[19] Krishnan, R., Arumugam, R., and Lindsay, James F. "Design Procedure for Switched-Reluctance Motors." IEEE Transactions on Industry Applications, v.24, n.3, May/June 1988.

[20] Miller, T.J.E. and McGilp, M. "Nonlinear Theory of the Switched Reluctance Motor for Rapid Computer-Aided Design." IEE Proceedings, v.137, pt.B, n.6, November 1990.

[21] Corda, J. and Stephenson, J.M. "Computation of torque and current in doubly salient reluctance motors from nonlinear magnetisation data." IEE Proceedings, v.126, n.5, May 1979.

APPENDICES

Appendix A
TASK SRM Specifications

The test machine is a 4kW, 6/8, 4 phase SRM from TASK Drives of United Kingdom. The system controller is the OULTON 112. [6]

Table A1 Nameplate Data of OULTON Machine

Nameplate data of SRM test machine	
number of phases	4
Rated HP	5.5
Rated Voltage (V)	380/415
Nominal Current (A)	9
Supply Frequency (Hz)	50/60
Nominal Speed (rpm)	1500

According to [6], the exact dimensions of the SRM are not known. All measurements given were estimated from direct measurement [6].

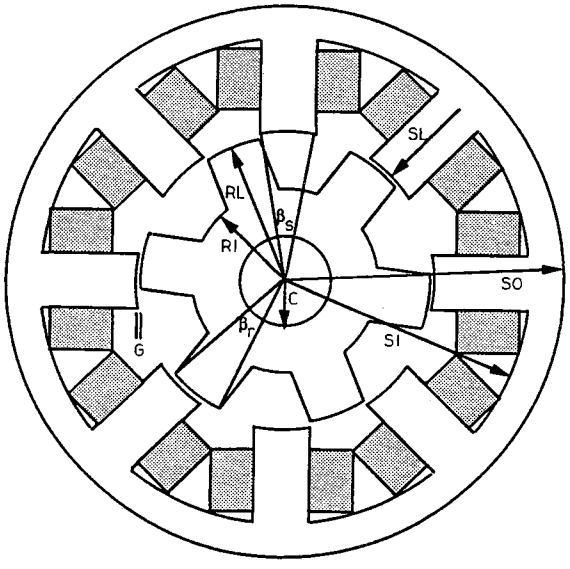

Figure A1 Description of OULTON Machine Dimensions

Table A2 Dimensions of OULTON Machine

Geometric Information of SRM	
all dimensions given in mm	
Z (axial length)	151.0
SI	78.4
SO	89.8
SL	30.22
SW	found from angle
β_s (degrees)	20.2°
RL	47.82
RI	30.3
RW	found from angle
β_r (degrees)	22.5°
G	0.36
RT	6 teeth
ST	8 teeth
N (turns/pole)	56 turns
C	15.0
V_{DC} (volts)	300.0
(internal) R_{int} (Ω)	0.6226

Appendix B
B-H Data Table

Table B1 B-H Table Data

B-H Curve of Motor Laminations	
B (Tesla)	H (Ampere-turn/m)
0.0	0.0
0.5	54.0
0.55	60.5
0.6	67.6
0.65	74.8
0.7	83.5
0.75	93.5
0.8	104.4
0.85	116.9
0.9	131.3
0.95	148.2
1.0	167.1
1.05	187.8
1.1	214.9
1.15	250.7
1.2	298.4
1.25	374.0
1.3	485.5
1.35	652.6
1.4	1010.6
1.45	1551.8
1.5	2308.0
1.55	3342.0
1.6	4775.0

Table B1, continued

1.65	6366.0
1.7	8356.0
1.75	10743.0
1.8	14165.0
1.85	18303.0
1.9	23874.0
1.95	30240.0
2.0	44565.0
2.05	79580.0
2.06	87537.7

Appendix C
Cubic Spline Derivations

The cubic spline method utilizes a third-order polynomial for each interval between knots or the points of the given data. The objective of the cubic spline method is to find the corresponding flux intensity (H) given a flux density (B). The function relating the two variables is $B=\mu H$. Using the mathematical derivations given in [9], the cubic equation for each interval is:

$$f_i(x) = \frac{f''(x_{i-1})}{6(x_i - x_{i-1})}(x_i - x)^3 + \frac{f''(x_i)}{6(x_i - x_{i-1})}(x - x_{i-1})^3 + \left[\frac{f(x_{i-1})}{x_i - x_{i-1}} - \frac{f''(x_{i-1})(x_i - x_{i-1})}{6}\right](x_i - x) + \left[\frac{f(x_i)}{x_i - x_{i-1}} - \frac{f''(x_i)(x_i - x_{i-1})}{6}\right](x - x_{i-1}) \quad \text{(C.1)}$$

where:

f(x) -function to be interpolated (flux intensity (H))

x -known variable (flux density (B))

x_i, x_{i-1} -the flux density knots above and below the known value of B

$f''(x)$ -second derivatives of the function to solve

Before equation (C.1) can be utilized, the second derivatives of the function must be found. The second derivatives of equation (C.1) are described as [9]:

$$(x_i - x_{i-1})\,f''(x_{i-1}) + 2\,(x_{i+1} - x_{i-1})\,f''(x_i) + (x_{i+1} - x_i)\,f''(x_{i+1})$$
$$= \frac{6}{(x_{i+1} - x_i)}\,[f(x_{i+1}) - f(x_i)] + \frac{6}{(x_i - x_{i-1})}\,[f(x_{i-1}) - f(x_i)] \qquad \text{(C.2)}$$

where:

f(x) -function to be interpolated (flux intensity (H))

x -known variable (flux density (B))

x_i, x_{i-1} -the flux density knots above and below the known value of B

$f''(x)$ -second derivatives of the function to solve

Since the second derivatives for each and every interval of the B-H relationship has to be known, all the derivatives are calculated at once. Therefore, the right-hand side of equation (C.2) is solved for each B and H value known from the table in Appendix B. The results are stored in an array which is referenced by the derivative number. Thus, for the B values of 0.5 and 0.55 of Appendix B, the second derivative indexing numbers are one and two respectively. The end knots or the beginning and ending B's are not counted since the second derivatives of those points are zero. This array can be denoted as array G. The difference equations for B on the left-hand side of equation (C.2) (i.e. $x_i - x_{i-1}$) are solved and stored in an array in a block format. This array can be generalized as:

$$A=\begin{bmatrix} 0.0 & 2(x_{i+1}-x_{i-1}) & (x_{i+1}-x_i) & 0.0 & & \\ 0.0 & (x_i-x_{i-1}) & 2(x_{i+1}-x_{i-1}) & (x_{i+1}-x_i) & 0.0 & .... \\ 0.0 & 0.0 & (x_i-x_{i-1}) & 2(x_{i+1}-x_{i-1}) & 0.0 & ... \\ 0.0 & 0.0 & 0.0 & ... & & \\ ... & & & & & \\ ... & & & & & \end{bmatrix} \quad (C.3)$$

where:

A -matrix containing all relationships of left-hand side of equation (C.2)

x -known variable (flux density (B))

x_i, x_{i-1} -the flux density knots above and below the known value of B

Thus, the relationship for the second derivatives can be described as:

$$A*Y=G \quad (C.4)$$

where:

A -matrix containing all relationships of left-hand side of equation (C.2)

G -array containing solved equations of the right-hand side of equation (C.2)

Y -array containing the second derivatives of each knot in B-H table with the exception of the end knots

Y is found by inverting the A matrix and multiplying the G array to A^{-1}. With Y known, equation (C.1) can be used to interpolate any value of H with any given value of B.

Appendix D
Roter's Derivations

The Roter's derivations are based on the methodology described in [8]. There are different flux path calculations for each rotor position. The derivation of Roter's has three distinct regions: aligned, non-aligned and leakage. The derivation will set up the angles and flux paths for each region.

Aligned

There are three different cases to consider in the aligned position. While the stator and the rotor may be aligned the rotor width could be larger or smaller than the stator. Figure D1 shows the rotor and the stator the same width. Note that θ_r is some value even as the rotor is aligned. This was done as an example and in reality the rotor would be aligned at some point away from the origin. Alignment is the portion of the air gap between the rotor and stator poles. As the rotor moves away from the stator pole, the air gap alignment decreases. Eventually, R(3) will disappear as non-alignment occurs. The relationship between air gap alignment and the rotor position can be described as:

$$\alpha = -\theta_r + \frac{\beta_s}{2} + \frac{\beta_r}{2} \qquad (D.1)$$

where:

θ_r -rotor position

β_s -half of the stator pole angular width

β_r -half of the rotor pole angular width

The programming considers cases were the rotor pole is larger or smaller than the stator and finds α accordingly. For Figures D2 and D3 an IF statement checks the stator and rotor widths respectively. For example, the IF statement describing Figure D3 would be described as:

$$IF\left(\frac{\beta_r}{2}-\theta_r \ .GE. \ \frac{\beta_s}{2}\right) THEN \ \alpha=\beta_s$$
$$ELSE\left(-\theta_r+\frac{\beta_s}{2}+\frac{\beta_r}{2}=\alpha\right) \qquad (D.2)$$

α is the angular distance of the air gap overlap between the rotor and the stator. To find the real distance (d) of the overlap the geometrical relationship of $d=r\theta$ is used. Once α is determined, the actual flux paths can be marked and the reluctances calculated. Figure D4 shows the flux path marked R(3). This path is far by the easiest to calculate due to its rectangular nature. The reluctance is calculated using the equation given in [8]:

$$dR=\int \frac{dl}{\mu s}=\int_{r=r1}^{r=r1+g} \frac{dr}{\theta\ \mu\ r1\ z}=\int_{r=r1}^{r=r1+g} \frac{dr}{\alpha\ z\ r1\ \mu}= \tag{D.3}$$

$$R(3)=\frac{1}{\alpha\ \mu\ z}\left(\log\left(\frac{r1+g}{r1}\right)\right)$$

where:

r1 –radius of rotor pole

g –air gap length

s –area of gap

z –axial length of machine

μ –permeability of air

Figure D5 shows a situation when the rotor pole width is larger than the stator. In effect, two more flux paths other than R(3) become evident. These paths are quarter-circle shaped since the flux leaves the tip of the stator pole. Since the paths are symmetrical, R(2) and R(4) are the same. The programming allows for these paths by checking an IF statement. The formulation is:

$$IF((\alpha \cdot r1).LT.(\beta_r \cdot r1-g))\ THEN$$

$$R(2)=R(4)=\frac{(1.29g)}{\left(\mu\left(\frac{gz}{2}\right)\right)} \tag{D.4}$$

In addition, figure D6 shows an instance when the stator pole width is larger than the rotor. Again, the formulation is:

$$IF((\alpha \cdot r1).LT.(\beta_s \cdot r1 - g))\ THEN$$

$$R(2) = R(4) = \frac{1.29g}{\mu\left(\frac{gz}{2}\right)} \qquad \text{(D.5)}$$

If the rotor and stator poles are the same widths then the reluctance of paths R(2) and R(4) are zero.

As the rotor moves further away from alignment, paths R(2), R(3) and R(4) will not adequately describe the flux paths. Figure D7 shows the two additional flux paths and by far the largest ones for the case of a larger rotor pole width. Paths R(1) and R(5) are highly dependent on the rotor position with respect to alignment. As the rotor moves further away from the stator, path R(5) will increase while path R(1) will decrease. The programming decides through IF statements which situation is taking place via rotor position. The procedure for path R(1) is:

$$(IF(\beta_r \cdot r1 - \alpha \cdot r1 - 2g) \ .LT. \ (\beta_r \cdot r1)) \ THEN$$

$$x1 = \frac{\beta_r}{2} \cdot r1 - \frac{\alpha}{2} \cdot r1 - g - (\theta_r \cdot r1)$$

$$IF(x1 \ .GT. \ 0) \ THEN$$

$$R(1) = \frac{\left(\frac{(x1+g)\ (1.57+\theta_r) + (1.57g)}{2} \right)}{\mu \cdot x1 \cdot z} \qquad (D.6)$$

$$ELSEIF(\ \beta_s \cdot r1 - \alpha \cdot r1 - g \ .GT. \ 0)$$

$$x = \beta_s \cdot r1 - \alpha \cdot r1 - g$$

$$R(1) = \frac{\left(\frac{(x+g)\ (1.57+\theta_r) + (1.57g)}{2} \right)}{\mu \cdot x \cdot z}$$

Path R(5) is found using the same methodology:

$$x2 = \frac{\beta_r}{2} \cdot r1 - \frac{\alpha}{2} \cdot r1 - g$$

$$IF(x2 . GT . 0) \ THEN$$

$$R(5) = \frac{\left(\frac{(x2+g)\ (1.57+\theta_r) + (1.57g)}{2} \right)}{\mu \cdot x2 \cdot z} \qquad (D.7)$$

$$ELSE \ x = \beta_r \cdot r1 - \alpha \cdot r1 - g$$

$$R(5) = \frac{\left(\frac{(x+g)\ (1.57+\theta_r) + (1.57g)}{2} \right)}{\mu \cdot x \cdot z}$$

In the case where the stator width is larger than the rotor as shown in Figure D8, equations (D.6) and (D.7) are modified to accomodate the change in dimensions. R(1) can be solved

as:

$$x1=\frac{\beta_s}{2}\cdot r1-\frac{\alpha}{2}\cdot r1-g-\theta_r\cdot r1$$

$$IF(x1\ .GT.\ 0)\ THEN$$

$$R(1)=\frac{\left(\frac{(x1+g)\ (1.57+\theta_r)+(1.57g)}{2}\right)}{\mu\cdot x1\cdot z} \qquad (D.8)$$

$$ELSEIF\ (\beta_r\cdot r1-\alpha\cdot r1-g\ .GT.\ 0)\ THEN$$

$$x=\beta_r\cdot r1-\alpha\cdot r1-g$$

$$R(1)=\frac{\left(\frac{(x+g)\ (1.57+\theta_r)+(1.57g)}{2}\right)}{\mu\cdot x\cdot z}$$

The same logic can be used to determine path R(5):

$$x2=\frac{\beta_s}{2}\cdot r1-\frac{\alpha}{2}\cdot r1-g$$

$$IF(x2\ .GT.\ 0)\ THEN$$

$$R(5)=\frac{\left(\frac{(x2+g)\ (1.57+\theta_r)+(1.57g)}{2}\right)}{\mu\cdot x2\cdot z} \qquad (D.9)$$

$$ELSE\ x=\beta_s\cdot r1-\alpha\cdot r1-g$$

$$R(5)=\frac{\left(\frac{(x+g)\ (1.57+\theta_r)+(1.57g)}{2}\right)}{\mu\cdot x\cdot z}$$

Figures D9 and D10 show the method used to determine the average length and area of the quarter-circle paths used for R(1), R(2), R(4) and R(5). The average length of the

quarter-circles is the line marked d_2 in Figure D9. The area found is the average between the top of the quarter-circle (A=0) and the bottom of the shape (A=gz). In Figure D10, w varies with the change in α for path R(1) and R(5). The lengths and areas calculated in Figures D9 and D10 are used in equations (D.4) to (D.9) for determining the reluctances of the flux paths.

Non-Aligned

The non-aligned portion of Roter's method relies on angle relationships for determining the flux path reluctances. At non-alignment, α is not used due to the lack of any alignment between the rotor and the stator. Figure D11 shows the angular relationships used to describe the distance between the rotor and the stator poles. The variable (l) changes for each movement of the rotor pole. The variable (l) is used for determining the distance of the flux paths during non-alignment.

The angular relationships of Figure D12 change depending on the length between the rotor and stator poles. These angles are used to determine the distances along with (l). Figure D13 shows the actual relationship between the angles and the lengths and areas. The box situated between the tips of the rotor and stator poles allows for easy approximation of the flux paths. Since the length of the box is (l) and the height is (g), the diagonal of the box can be called (c)

which is defined as $\sqrt{(g^2+l^2)}$. The inner path can be described by the lengths of l_1 and l_2. The cross-sectional area of the path can be designated as the diagonal of A_1 and A_2 as well as the variable (c). The final length and area of the center path can be solved by:

$$l_1 = YANG \cdot c \quad A_1 = (\sqrt{j^2+k^2}) \cdot Z$$

$$l_2 = SIG \cdot c \quad A_2 = (\sqrt{l^2+g^2}) \cdot Z$$

$$A_3 = (\sqrt{j^2+k^2}) \cdot Z$$

$$where\ c = \sqrt{l^2+g^2} \qquad (D.10)$$

total length and area is:

$$length = \frac{l_1+l_2+c}{3} \ and$$

$$area = \frac{A_1+A_2+A_3}{3}$$

where:

YANG, SIG -angles solved in Figure D12

$j = \sqrt{l^2+g^2} - l$

$k = \sqrt{l^2+g^2} - g$

z -axial length

The outer paths are solved by using the angle relationships too. The outer flux paths are found using the averages of the lengths and the areas. The following equation details the derivation as:

$$OUTL1=\frac{\left(l_1+(YANG\cdot(\frac{SL}{2}-C-G))\right)}{2}$$

$$OUTA1=(\frac{SL}{2}-C)\cdot Z \qquad (D.11)$$

$$OUTL2=\frac{(l_2+(SIG\cdot(NSW+C)))}{2}$$

$$OUTA2=(NSW-C)\cdot Z$$

where:

$\frac{SL}{2}$ -half the stator length

$NSW=(R1+G)\cdot\beta_s$

The lengths and areas of equation (D.11) are used to find the reluctances of those paths. Thus, all the paths found are put in parallel along with the leakage path from the stator pole to the inside radius of the rotor. The reluctance of this path is found by finding the lengths and areas which are described as:

$$l=g+R1-\frac{RI}{2}$$

$$A=\frac{\left((\beta_s\cdot(R1+g))+(\beta_s\cdot(\frac{RI}{2}))\right)}{2}\cdot Z \qquad (D.12)$$

where:

RI -rotor inside diameter

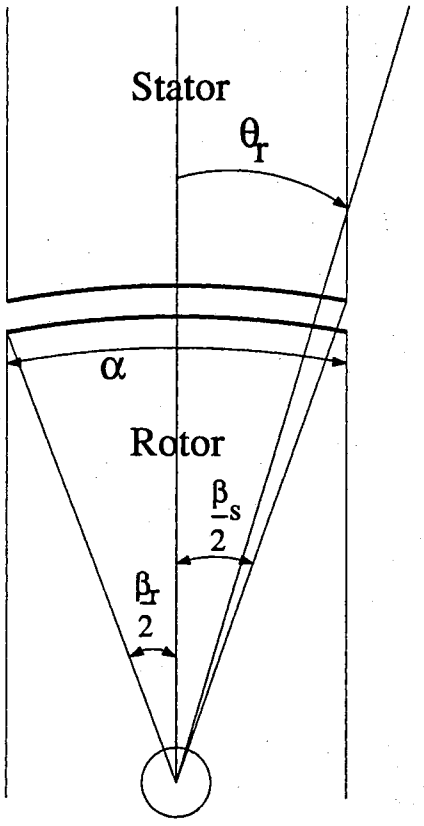

$$\beta_T = \beta_S$$

Figure D1 Finding α When $\beta_s = \beta_r$

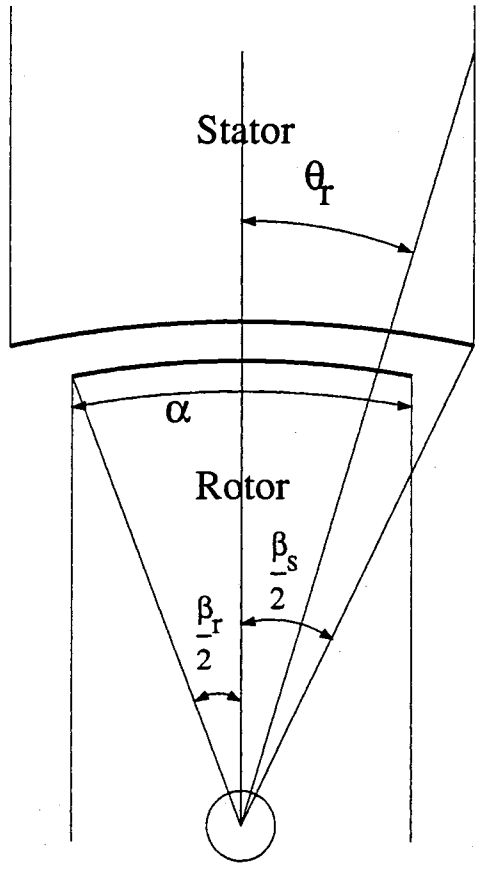

Figure D2 Finding α When $\beta_s > \beta_r$

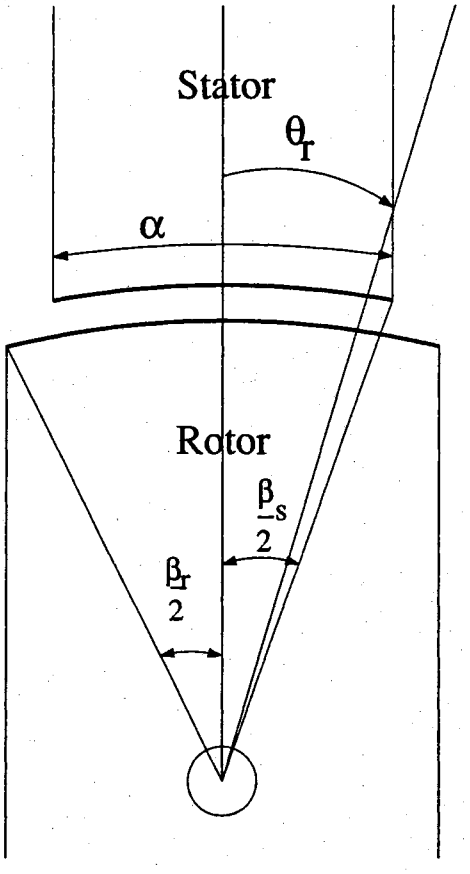

Figure D3 Finding α When $\beta_s < \beta_r$

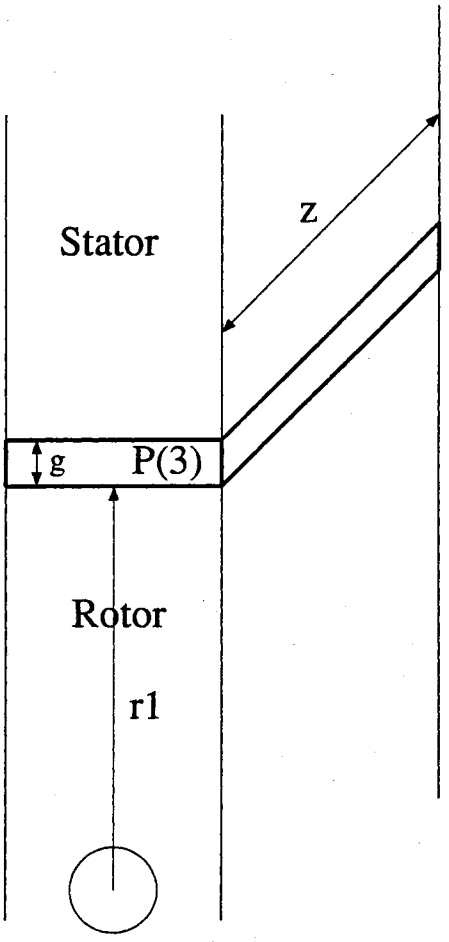

Figure D4 Permeance Path P(3)

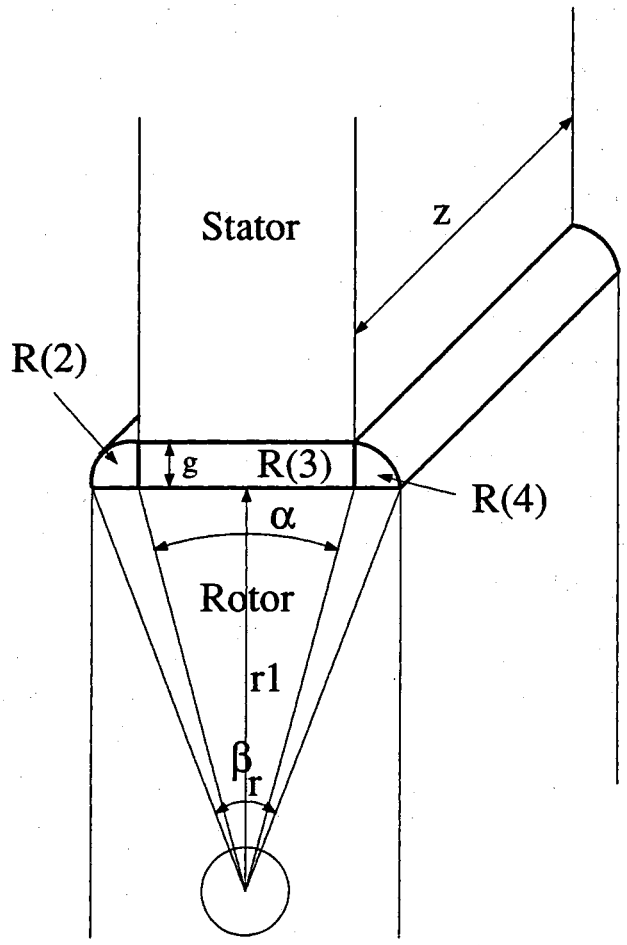

Figure D5 Reluctance Paths When $\beta_s < \beta_r$

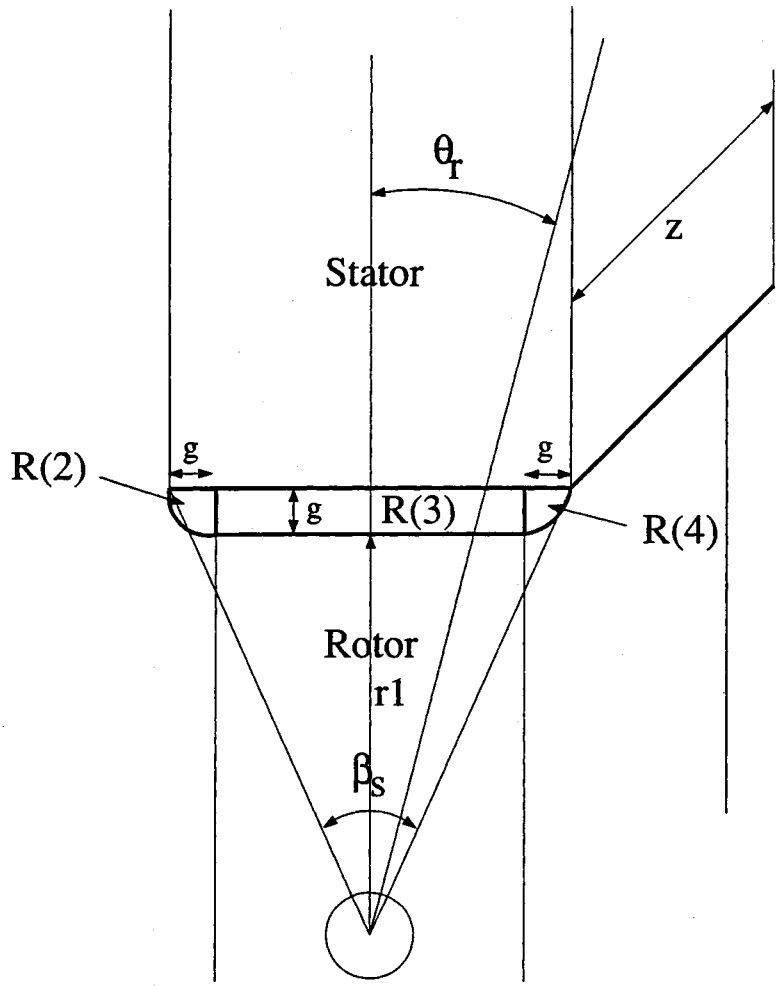

Figure D6 Reluctance Paths When $\beta_s > \beta_r$

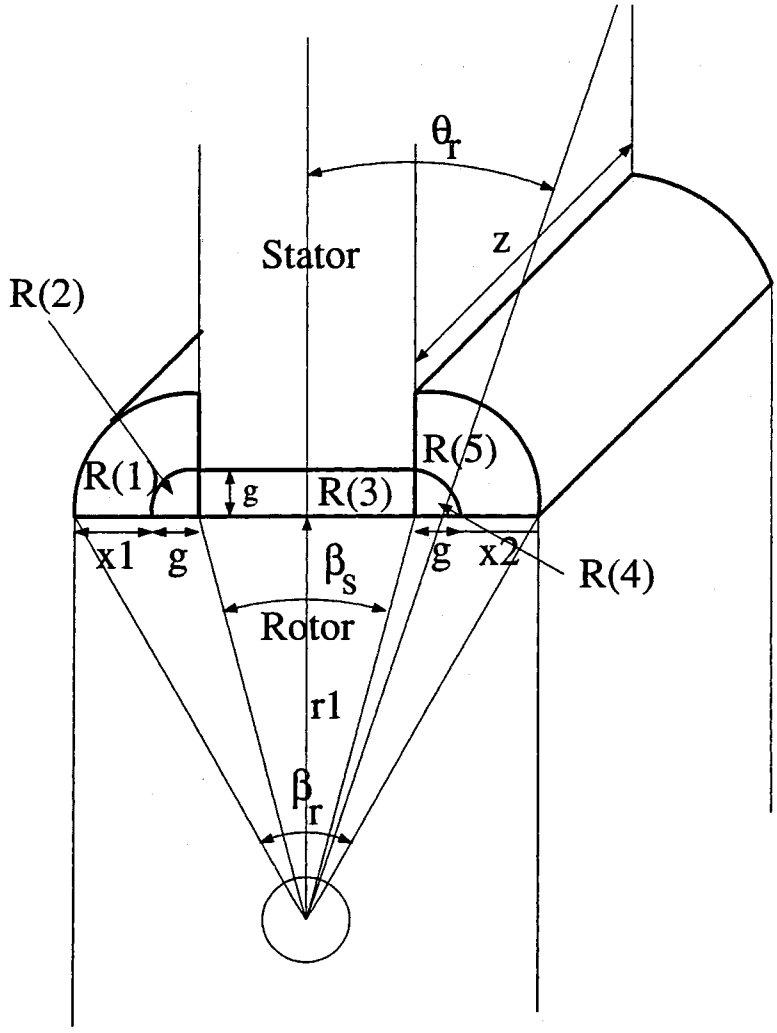

Figure D7 Outer Reluctance Paths When $\beta_s < \beta_r$

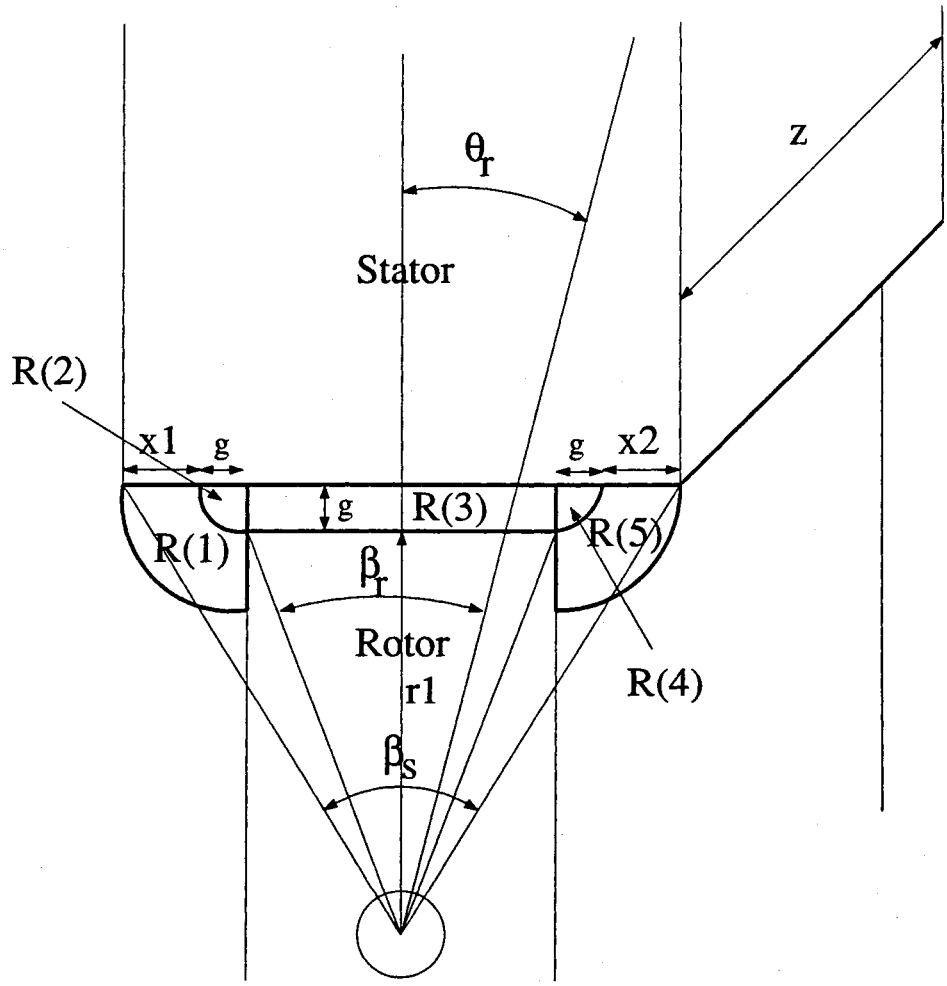

Figure D8 Outer Reluctance Paths When $\beta_s > \beta_r$

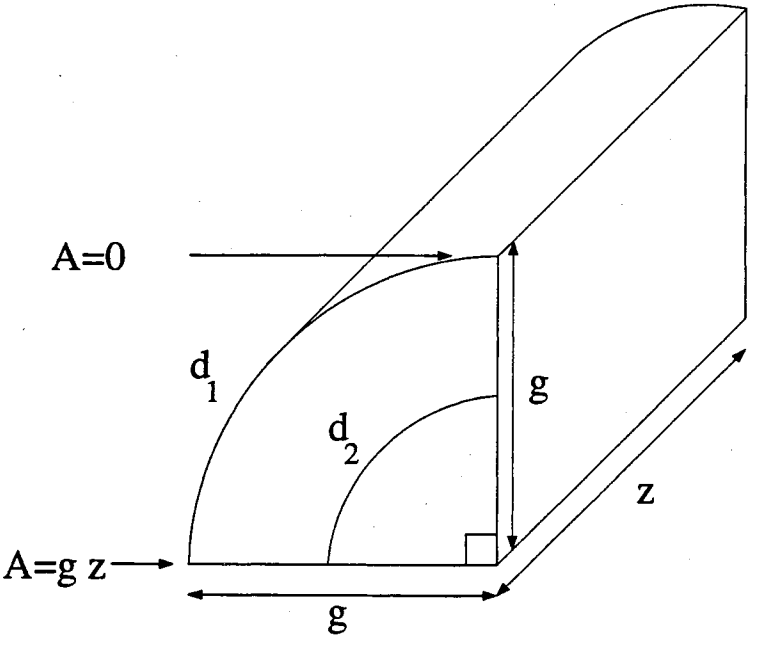

$$A=\frac{gw}{2}$$

$$\text{(average) } l=\frac{2.57g}{2}=1.29g$$

$$d=r\theta$$

$$d_1=g(\ 90^{o})$$

$$d_1=g(1.57)\text{ rads}$$

$$d_2=\frac{1.57g+g}{2}$$

Figure D9 l and A of Paths R(2) and R(4)

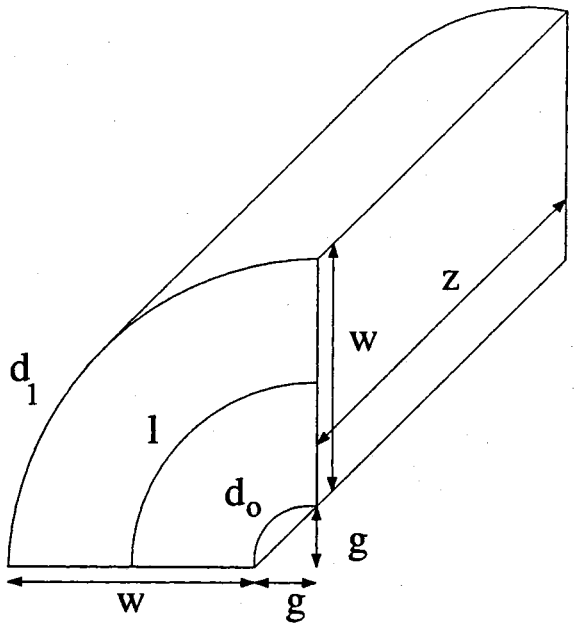

$$l=\frac{(w+g)(90+\theta_r)+g(1.57)}{2}$$

$$d=r\theta$$

$$d_1=(w+g)(1.57+\theta_r)$$

$$d_o=g(1.57)$$

$$A=zw$$

$$w=\beta_r r_1 - \alpha r_1 - g$$

Figure D10 l and A of Paths R(1) and R(5)

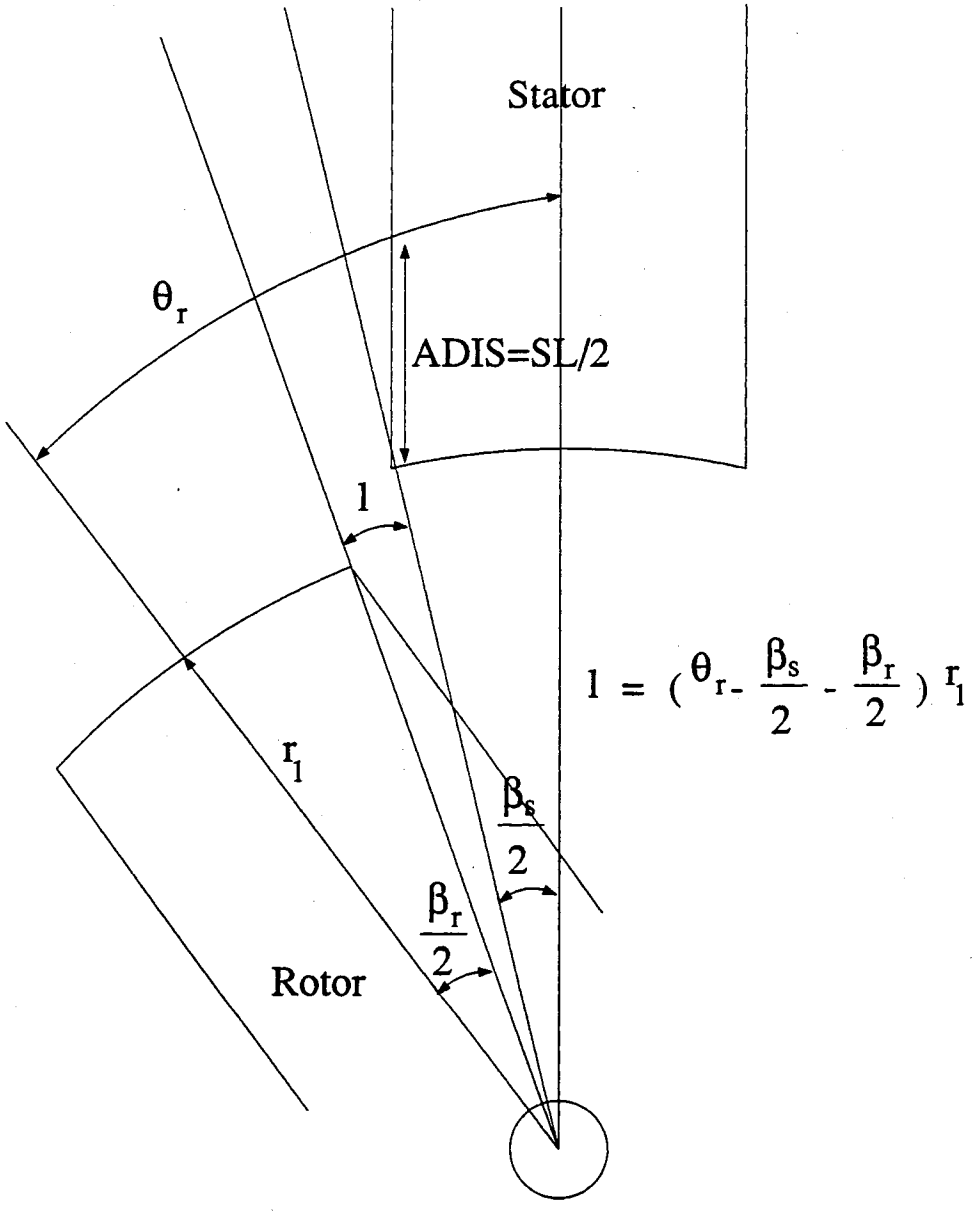

Figure D11 l During Non-Alignment

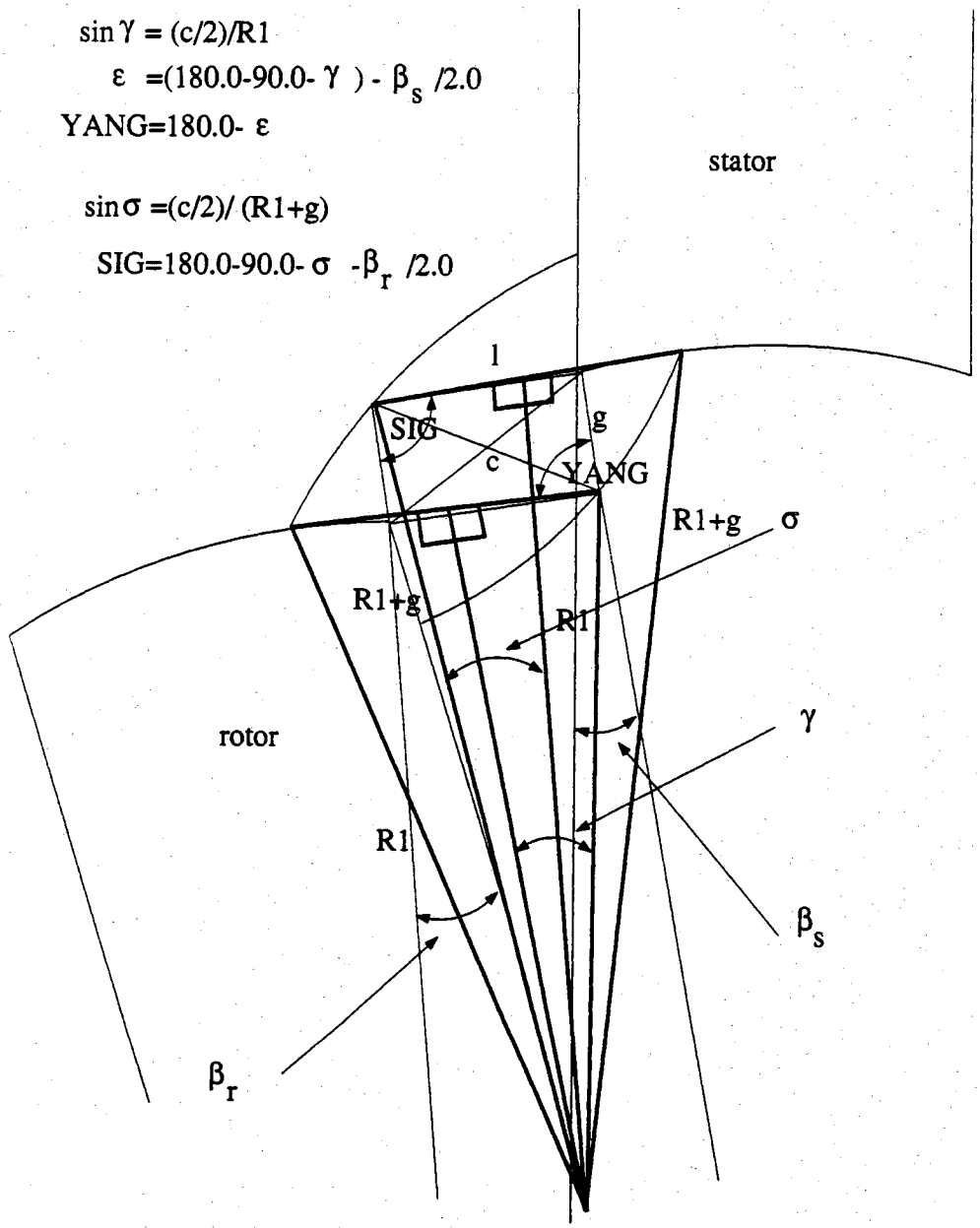

Figure D12 Non-Alignment Angular Relationships

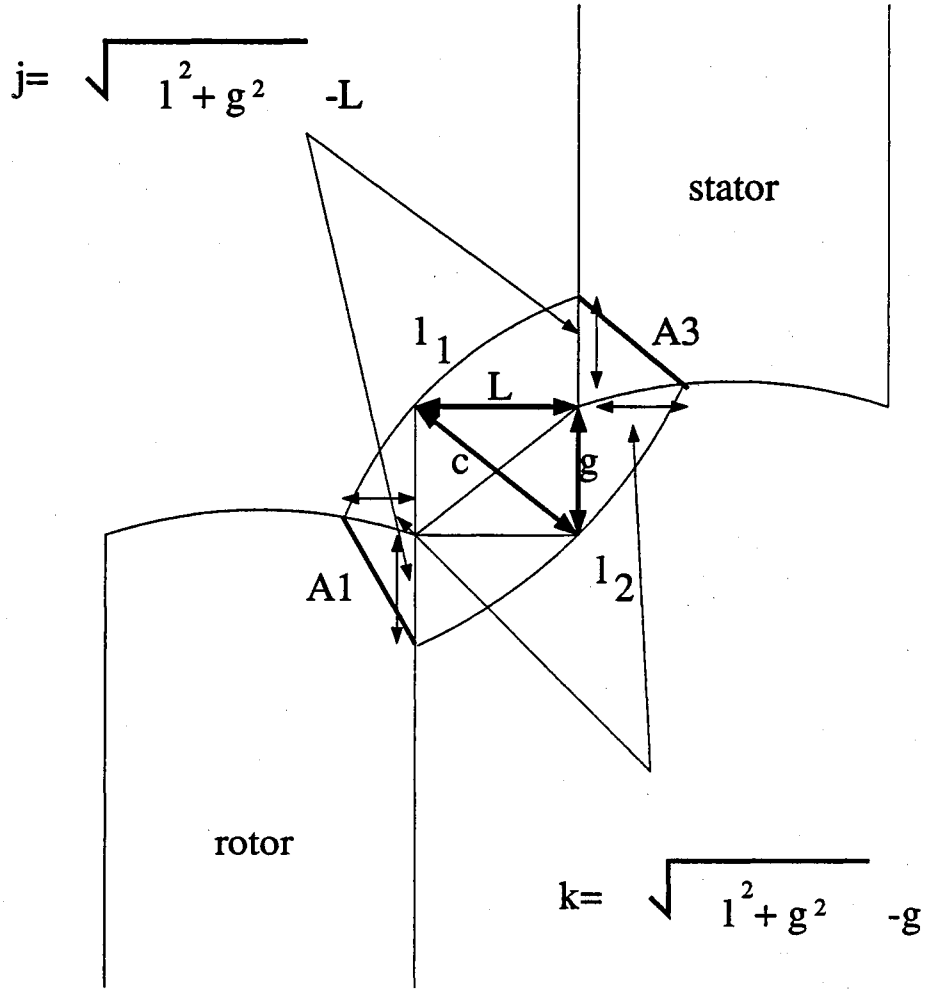

Figure D13 Non-Alignment Flux Paths

Appendix E
Experimental SRM Specifications

The test machine is a 60kW, 6000rpm, 4/6 SRM.

Table E1 Nameplate Data of Experimental Machine

Nameplate data of SRM test machine	
The nameplate data for this SRM are not needed.	
The flux Linkages and dimensions were known.	

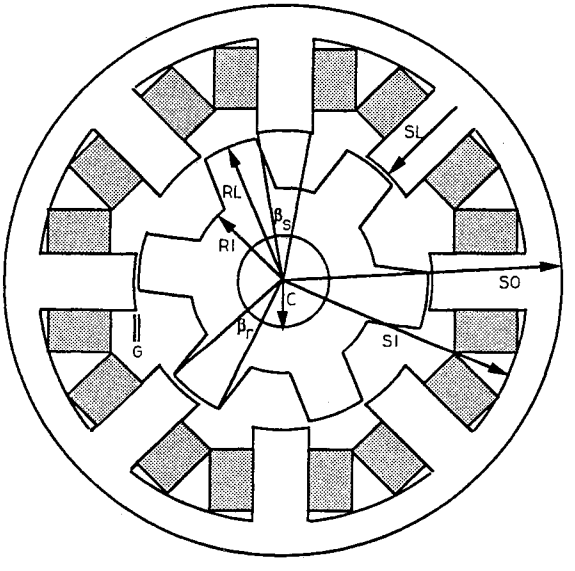

Figure E1 Description of Experimental Machine Dimensions

Table E2 Dimensions of Experimental Machine

Geometric Information of SRM	
all dimensions given in mm	
Z (axial length)	140.0
SI	102.0
SO	135.0
SL	25.0
SW	found from angle
β_s (degrees)	28.0°
RL	70.0
RI	40.0
RW	found from angle
β_r (degrees)	28.0°
G	1.0
RT	4 teeth
ST	6 teeth
N (turns/pole)	24 turns
C	18.0
Experimental machine was not simulated; the voltage and the internal winding resistance are not needed.	

Appendix F
Method of Calculating $\frac{\partial \mathfrak{R}}{\partial \phi}$

The method of calculating $\frac{\partial \mathfrak{R}}{\partial \phi}$ is greatly simplified using the basic magnetic principles described in equations (2.1), (2.2.) and (2.3). In order to describe H in terms of the flux density (B), H can be described as:

$$H=\nu \cdot B \tag{F.1}$$

where:

$\nu=\frac{1}{\mu}$

B -flux density

H -flux intensity

Substituting equation (2.1) into equation (F.1), the result is shown as:

$$\nu \cdot B \cdot l=\phi \cdot \mathfrak{R} \tag{F.2}$$

where:

$\nu=\frac{1}{\mu}$

B -flux density

l -length of magnetic material used

ϕ -flux traveling through material

$\mathfrak{R}$ -reluctance of material

Using equation (2.3), the relationship described in equation (F.2) can be expressed as:

$$\mathfrak{R}=\frac{\nu \cdot l}{A} \qquad \text{(F.3)}$$

where:

$\nu=\frac{1}{\mu}$

l -length of magnetic material used

$\mathfrak{R}$ -reluctance of material

A -cross-sectional area of material

$\frac{\partial \mathfrak{R}}{\partial \phi}$ can be expanded by utilizing the chain rule and is expressed as [14]:

$$\frac{\partial \mathfrak{R}}{\partial \phi}=\frac{\partial \mathfrak{R}}{\partial B}\cdot\frac{\partial B}{\partial \phi} \qquad \text{(F.4)}$$

where:

$\mathfrak{R}$ -reluctance of material

ϕ -flux traveling through material

B -flux density of material

Using equation (2.3), the relationship shown in equation (F.4) can be denoted as:

$$\frac{\partial \mathfrak{R}}{\partial \phi} = \frac{\partial \mathfrak{R}}{\partial B} \cdot \frac{1}{A} \qquad \text{(F.5)}$$

where:

$\mathfrak{R}$ -reluctance of material

ϕ -flux traveling through material

B -flux density of material

A -cross-sectional area of material

Understanding that the denominator of equation (F.5) is equal to the flux and substituting equation (F.3) into equation (F.5), the result is:

$$\frac{\partial \mathfrak{R}}{\partial \phi} = \frac{\partial \nu}{\partial B} \cdot \frac{l}{A} \qquad \text{(F.6)}$$

where:

$\mathfrak{R}$ -reluctance of material

ϕ -flux traveling through material

B -flux density of material

A -cross-sectional area of material

l -mean length of material

$\nu = \frac{1}{\mu}$

Therefore, $\frac{\partial \nu}{\partial B}$ must be found to satisfy equation (F.6).

Knowing the association shown in (F.1), $\frac{\partial \nu}{\partial B}$ can be found

using the cubic spline formulation for the B-H curve. H can be described by a cubic equation which is expressed as:

$$H=a_1B^3+a_2B^2+a_3B+a_4 \qquad (F.7)$$

where:

H -flux intensity

B -flux density

a -constants

Since $\nu=\frac{H}{B}$, equation (F.7) can be modified and expressed as:

$$\nu=a_1B^2+a_2B+a_3+\frac{a_4}{B} \qquad (F.8)$$

where:

B -flux density

a -constants

$\nu=\frac{1}{\mu}$

Taking the partial of equation (F.8) with respect to B can be expressed as:

$$\frac{\partial\nu}{\partial B}=a_1B+a_2-\frac{a_4}{B^2} \qquad (F.9)$$

where:

B -flux density

a -constants

$$\nu = \frac{1}{\mu}$$

Thus, equation (F.9) can be substituted into equation (F.6) to find $\frac{\partial \Re}{\partial \phi}$. However, the constants (a) need to be found first. Equation (C.1) of Appendix C can be used to find the constants by manipulation. By multiplying out and expanding equation (C.1), the equation can be grouped according to the powers of B. Thus, for B^3 (or x^3), a_1 can be expressed as:

$$a_1 = \frac{f''(x_i)}{6(x_i - x_{i-1})} - \frac{f''(x_{i-1})}{6(x_i - x_{i-1})} \qquad \text{(F.10)}$$

where:

f(x) -function to be interpolated (flux intensity (H))

x_i, x_{i-1} -the flux density knots above and below the known value of B

$f''(x)$ -second derivatives of the function to solve

The constants a_2, a_3, and a_4 are expressed for B^2, B, and B^0, respectively, using the same method used in equation (F.10).

Appendix G
$\lambda(\theta, i)$ Interpolation Derivation

As discussed in chapter four, a method of interpolating the flux linkages is needed for the machine simulation. The patch in Figure 25 shows a sample of the flux linkage profile portrayed in Figure 20. The objective of the interpolation method is to deduce or interpolate the value of the flux linkage (λ) in the middle of the patch of Figure 25.

Equation (4.8) is expanded to describe each λ node of the patch. Thus, the interpolation equations for the patch can be expressed as:

$$\begin{aligned}
\lambda_{aa} &= a_1 + a_2\theta_a + a_3 i_a + a_4\theta_a i_a \\
\lambda_{ab} &= a_1 + a_2\theta_a + a_3 i_b + a_4\theta_a i_b \\
\lambda_{ba} &= a_1 + a_2\theta_b + a_3 i_a + a_4\theta_b i_a \\
\lambda_{bb} &= a_1 + a_2\theta_b + a_3 i_b + a_4\theta_b i_b
\end{aligned} \qquad \text{(G.1)}$$

where:

λ -flux linkages for each corner of the patch

θ -angle index for each point

i -current index for each point

a -constants

Before the interpolation can begin, the constants (a) have to be found. Since equation (G.1) consists of four equations and four unknowns, the constants can be found by back-solving. Substituting λ_{ab} into λ_{aa} and λ_{bb} into λ_{ba}, the

modified equations are expressed as:

$$\lambda_{aa}-\lambda_{ab}=a_3(i_a-i_b)+a_4\theta_a(i_a-i_b)$$
$$\lambda_{ba}-\lambda_{bb}=a_3(i_a-i_b)+a_4\theta_b(i_a-i_b) \qquad \text{(G.2)}$$

where:

λ -flux linkages for each corner of the patch

θ -angle index for each point

i -current index for each point

a -constants

Further manipulation of equation (G.2) results in solving for the constants which are expressed as:

$$a_4=\frac{\lambda_{aa}-\lambda_{ab}-\lambda_{ba}+\lambda_{bb}}{(i_a-i_b)\cdot(\theta_a-\theta_b)}$$
$$a_3=\frac{\lambda_{ba}-\lambda_{bb}-a_4\theta_b(i_a-i_b)}{(i_a-i_b)} \qquad \text{(G.3)}$$

where:

λ -flux linkages for each corner of the patch

θ -angle index for each point

i -current index for each point

a -constants

Utilizing λ_{aa} and λ_{bb}, the remaining constants can be derived and are expressed as:

$$a_2=\frac{\lambda_{aa}-\lambda_{bb}-a_3(i_a-i_b)-a_4(\theta_a i_a-\theta_b i_b)}{(\theta_a-\theta_b)} \qquad (G.4)$$

$$a_1=\lambda_{aa}-a_2\theta_a-a_3 i_a-a_4\theta_a i_a$$

where:

λ -flux linkages for each corner of the patch

θ -angle index for each point

i -current index for each point

a -constants

Therefore, the patch of Figure 25 can be interpolated using equation (4.8) which is expressed as:

$$\lambda(\theta, i)=a_1+a_2\theta+a_3 i+a_4\theta i \qquad (G.5)$$

where:

λ -flux linkages for each corner of the patch

θ -angle index for each point

i -current index for each point

a -constants

Equation (G.5) can be used to interpolate flux given a specific value of current and rotor position. Equation (G.5) coupled with equation (4.5) can be modified to find the incremental inductance and can be expressed as:

$$L_{inc}=a_3+a_4\theta \qquad (G.6)$$

where:

L_{inc} -incremental inductance of the windings

a -constants found earlier

θ -rotor position

In addition to the incremental inductance, $\frac{\partial \lambda}{\partial \theta}$ can be found by taking the partial of equation (G.5) with respect to theta. The result is shown as:

$$\frac{\partial \lambda}{\partial \theta} = a_2 + a_4 i \qquad \text{(G.7)}$$

where:

a -constants found earlier

i -current in windings

The co-energy is found using the flux linkage interpolation method as well. The co-energy is vital to the simulation such that it provides an easy technique of finding torque. Since the co-energy is a definite integral, as described in [14], the equation requires the previous co-energy value to be known in order to find the next point. Thus, equation (G.5) can be modified to express the co-energy as:

$$W_c=\int_1^2 \lambda\, di=a_1 i+a_2\theta i+\frac{1}{2}a_3 i^2+\frac{1}{2}a_4\theta i^2$$

$$=a_1 i_2+a_2\theta i_2+\frac{1}{2}a_3 i_2^2+\frac{1}{2}a_4\theta i_2^2 \qquad (G.8)$$

$$-a_1 i_1+a_2\theta i_1+\frac{1}{2}a_3 i_1^2+\frac{1}{2}a_4\theta i_1^2+W_c(\theta,\ i_1)$$

where:

W_c -co-energy

a -constants solved earlier

i -current in windings

θ -rotor position

The co-energy is found for each current and theta used to find the flux linkages. Thus, the co-energy plot shown in Figure 32 is somewhat similar to the flux linkage profile of Figure 20. By finding the co-energy of the entire operating range, the torque is easily found by interpolating the co-energy profile.

Since torque is related to the co-energy by equation (4.12), the torque can be interpolated from the co-energy profile. The expression for torque is:

$$\frac{\partial W_c}{\partial\theta}=T_e=a_2+a_4 i \qquad (G.9)$$

where:

T_e -torque of machine

i -current in windings

a -constants

θ -position of rotor

The method of finding torque was simplified by generating profiles of the co-energy and torque. By using a torque profile, the torque for the machine operation was easily found by utilizing the current and the rotor position during simulation.